STAR FORMATION:
The Generation and Propagation of Jets from Young Stars

A dissertation submitted to the University of Dublin
for the degree of Doctor of Philosophy

Deirdre Coffey
December 2005

Department of Physics
University of Dublin
Trinity College

School of Cosmic Physics
The Dublin Institute for
Advanced Studies

For Mam and Dad

Declaration

I hereby declare that this thesis has not been submitted as an exercise for a degree at this or any other University and that, except where otherwise stated, it is entirely my own work.

I agree that the Library may lend or copy this thesis upon request.

Signed,

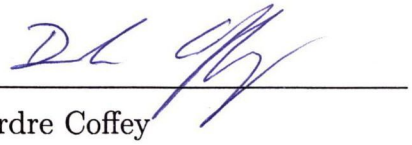

Deirdre Coffey

December 1, 2005.

Publications

Coffey, D., Bacciotti, F., Ray, T. P., Eislöffel, J., & Woitas, J., 2006, ApJ, *submitted*, 'Further indications of jet rotation in new ultraviolet and optical HST/STIS spectra'

Woitas, J., Bacciotti, F., Ray, T. P., Marconi, A., **Coffey, D.**, & Eislöffel, J., 2005, A&A, 432, 149, 'Jet rotation: Launching region, angular momentum balance and magnetic properties in the bipolar outflow from RW Aur'

Coffey, D., Bacciotti, F., Woitas, J., Ray, T. P., & Eislöffel, J., 2004, ApJ, 604, 758C, 'Rotation Of Jets From Young Stars: New Clues From The Hubble Space Telescope Imaging Spectrograph'

Coffey, D., Downes, T. P., & Ray, T. P., 2004, A&A, 419, 593, 'The evolution and simulation of the outburst from XZ Tauri - A possible EXor?'

Acknowledgments

I would like to acknowledge the support of Enterprise Ireland for this research. I would also like to acknowledge the work contributed by Dr Turlough P. Downes (DCU). His numerical simulations formed part of the CosmoGrid project, funded under the Programme for Research in Third Level Institutions (PRTLI) administered by the Irish Higher Education Authority under the National Development Plan and with partial support from the European Regional Development Fund.

It is with great pleasure that I take this opportunity to thank the following people for their help and support: Prof Tom Ray for being a great supervisor, for his guidance and advice, and for always having his door open; Dr Francesca Bacciotti for being a great collaborator and mentor, for her patience and encouragement, and for being a warm hostess on my trips to Florence; Dr Turlough Downes for being a great collaborator, for his patient explanations and for good chats in the pub; Drs Jochen Eislöffel and Jen Woitas for their helpful comments in all collaborations; Cian Crowley for sharing his knowledge of atomic line diagnostics and IDL, for interesting discussions about astrophysics, whether there was a point to it all, why there was a point afterall, and for pumping up my bike so I could get to work; Dr Brian Espey for sharing his indepth knowledge of STIS instrumentation, and for good naturedly tormenting me about the credibility of my results and the hilarity of my 'timeline'; Dr Thibaut Lery for allowing me to bombard him with questions about MHD; Drs Eric van der Swaluw, Dirk Froebrich and Matt Redmann, in order of appearance, for guiding me in their infinite wisdom as post-docs and in their fondness of the occasional pint; John Walsh and Stephane Dudzinski for being extremely helpful in their provision of computing support, and for trying hard not to talk about computers during lunch; Daniela Pandolfi for translating Italian notes for me; my fabulous flatmates Catriona, Ethna and Cian for a comical team proof-reading blitz the night before I submitted; everyone in DIAS for many happy times in the tea room, on the patio in the sun, and in the Gingerman. You know who you are!

And last but certainly not least, I want thank the people behind the scenes: Mam, Dad, Michael, Brendan and Niamh for their enormous support, and for making home a great place to have a laugh when I needed a break from rotating jets; Ivan for many welcome distractions; and Aoife, Celine, Larry, Damien, Sarah, Cian, Catriona and Ethna for their amazing friendship which kept me going.

Its been a great three years! Thank you!

Summary

While much progress has been made in recent decades, there are many outstanding questions about the star formation process, including how jets/outflows from young stars are launched and travel away from their source. This thesis constitutes an observational contribution to understanding the generation and propagation of jets and outflows from pre-main sequence stars. Long standing observational difficulties lie in the fact that young stars are often heavily embedded. Furthermore, due to the relatively small spatial and temporal scales, physical properties of jet/outflows can only be deduced from high angular resolution data. Consequently, to overcome these obstacles, this work focusses on more evolved, and hence less embedded, T Tauri stars and harnesses the high spatial resolution of the *Hubble Space Telescope* at optical and near ultraviolet wavelengths.

Imaging observations were extracted from the *Hubble Space Telescope* Archive of the pre-main sequence binary system XZ Tauri and its associated outflow. XZ Tauri is unusual in that *both* the source and outflow remnants are optically visible, making it an important case study at optical wavelengths. The accumulated archival data yielded high resolution images of the system spanning a total period of 6 years. The series of observations demonstrated that both the binary and outflow exhibit surprisingly dramatic changes on this short timescale. Specifically, the northern component of the binary was observed to increase by 3 orders of R-band magnitude in only 3 years. When considered in the light of previously published spectroscopic data, this strongly suggests that the northern component is undergoing a rapid increase in its accretion rate, leading to a flaring of the star and a violent outburst of jet material. In other words, the northern component is not only the most likely source of the outflow, but appears to be exhibiting EXor-type behaviour. This is of added interest considering that the number of known EXors is relatively few. A proper motions study of the outflow itself showed a marked deceleration of the shock front. Combining this with measurements of outflow morphology over the 6 year period, and making comparisons with observed outflow [SII] luminosity, provided parameters to guide simulations, since studies of cloud-shock interactions require numerical simulations to understand the detailed physics. These simulations highlighted the necessity of invoking a wide angle wind to reproduce the low aspect ratio of the bowshock, and a steep increase in ambient density to reproduce the shock deceleration.

Spectroscopic observations were then conducted with the *Hubble Space Telescope* (as part of the 'Guest Observer' programme) of 8 optically visible T Tauri jets close to their stellar source, in order to understand jet kinematics immediately after launch. It has

been proposed that jets from newly forming stars extract angular momentum from their source, which would otherwise reach unreasonably high rotational velocities. The strong correlation between outflow signatures and accretion diagnostics appears to support this supposition, but the origin of the jet and its driving mechanism still remain topics of intense debate. To date, observational backing for theoretical models has proved elusive due to observational constraints. Only recently has the high resolution of the *Hubble Space Telescope* provided tentative evidence of rotation for one T Tauri jet close to its source, thereby providing the motivation for this study. My work embodies the first *survey* evidence of systematic radial velocity differences across T Tauri jets before they have travelled beyond 100 AU from the star. These transverse radial velocity differences, of up to $30\,\mathrm{km\,s^{-1}}$, are interpreted as rotation signatures in the initial jet channel.

The optical spectroscopic survey was then extended to near ultraviolet wavelengths, so as to examine the targets with higher spatial and spectral resolution. Although the survey came to an abrupt end upon *Hubble Space Telescope* instrument failure, the first phase of observations had already been conducted, providing the first and now the only near ultraviolet dataset for the initial jet channel. Radial velocity differences were observed for all 3 targets, showing general agreement in magnitude and direction with the optical datasets. A Mg II absorption feature, Doppler shifted to $\sim$-$20\,\mathrm{km\,s^{-1}}$, appeared in all 3 targets and, unfortunately, significantly interrupted the emission profile leading to difficulties in data reduction. Therefore, the higher spectral resolution did not lead to improved results, as was originally hoped. Also, the higher spatial resolution was intended to probe the collimated higher velocity jet core, but the results revealed no detectable rotation signatures as the jet axis was approached. This phenomenon was also apparent in some of the optical targets, and is attributed to projection and beam smearing effects along the line of sight. Nevertheless, the near ultraviolet results support those of the optical survey, thus providing strong additional indications of rotation signatures in the initial jet channel of T Tauri jets.

Finally, the implications of jet rotation for theoretical models were examined. My kinematic analysis allowed calculation, in the context of the 'Disk wind' model, of the jet footpoint, i.e. the location from the star on the disk plane from which the jet is launched. The footpoint radius was found to extend from $\sim$0.1 AU to 2.5 AU from the star. Using footpoint values, calculation of mass and momentum fluxes then indicated that the jet could in fact extract a very significant fraction, and perhaps all, of the angular momentum from the system. This demonstrates *observationally* that it is very reasonable to assume jets can indeed play a significant role in angular momentum transport, allowing the star to rotate below break-up velocity and further accrete the material of its disk.

Contents

List of Figures

List of Tables

List of Acronyms

AMBER	**A**stronomical **M**ultiple **BE**am **R**ecombiner
AU	**A**stronomical **U**nit
CCD	**C**harge **C**oupled **D**evice
FEL	**F**orbidden **E**mission **L**ine
FOS	**F**aint **O**bject **S**pectrograph
FWHM	**F**ull **W**idth **H**alf **M**aximum
GMC	**G**iant **M**olecular **C**loud
GO	**G**uest **O**bserver
HH	**H**erbig **H**aro
HST	**H**ubble **S**pace **T**elescope
IRAF	**I**mage **R**eduction and **A**nalysis **F**acility
ISM	**I**nterstellar **M**edium
MAMA	**M**ulti-**A**node **M**icrochannel **A**rray
MHD	**M**agneto**h**ydro**d**ynamic
NUV	**N**ear **U**ltra**v**iolet
OVRO	**O**wens **V**alley **R**adio **O**bservatory
PA	**P**osition **A**ngle
STIS	**S**pace **T**elescope **I**maging **S**pectrograph
VLTI	**V**ery **L**arge **T**elescope **I**nterferometer
WPFC	**W**ide **F**ield **P**lanetary **C**amera
YSO	**Y**oung **S**tellar **O**bject

1

Introduction to Star Formation

The mystery of Star Formation is a long-standing one, observationally hindered by technological contraints, but is now reaching a crucial stage of advancement with the development of high resolution instruments and sophisticated numerical simulations. This chapter sets out a brief historical context for research in the field, gives a general overview of current understanding, and lastly describes the aim and structure of this thesis.

1.1 Historical Context

Star Formation research fully developed as an independent field of Astrophysics only in the latter half of the last century. Its beginnings, however, date back to Laplace (1796) who proposed the Nebular Hypothesis, one of the oldest surviving scientific hypotheses. It involved a rotating cloud of matter cooling and contracting under its own gravity to form a central star, while the remaining material flattens into a revolving disk from which planets are formed. Neverthless, at the turn of the twentieth century it was still generally assumed that stars lived forever, and so stellar origins were largely considered a question for cosmologists. In the early 1900s, the discovery of the nature of stars as thermonuclear reactors explained stellar evolution and death, but did not address the question of birth. Little was known beyond a broad understanding of the ongoing physical processes involved

when a giant molecular cloud collapses under its own gravity giving rise to clumps of gas and dust, each clump then individually contracting from this protostellar stage to the fusion-powered stellar core that is a pre-main sequence star.

The first step in the realisation of the true complexity of the star formation process came in the early 1950s when Herbig (1950; 1951) and Haro (1952; 1953) catalogued a series of small ionised nebulae which were consistently found to be located near star forming regions (see review of Reipurth & Bally, 2001). However the nature of the link between these so called Herbig-Haro objects (HH objects) and star forming sites remained unknown until the mid 1970s when it was recognised that these objects were shock fronts moving away from young stars (Schwartz, 1975). A key advancement in understanding was the realisation, in the 1980s, that HH objects are causally connected to highly collimated jets from pre-main sequence stars (Mundt & Fried 1983; Graham & Elias 1983; Mundt et al. 1984; Reipurth et al. 1986; Mundt et al. 1987). As the jets propagate into the surrounding cloud at velocities on the order of hundreds of kilometers per second, the ambient medium and the jet itself are rapidly shocked and ionised.

Only in the last thirty years has a coherent theory of star formation emerged. As a molecular cloud collapses, any initial rotation present is amplified resulting in a spinning of the core (Figure 1.1 left panel) and the formation from the remaining infalling dust and gas, of a rotating circumstellar disk (Figure 1.1 HH30 panel). Unexpectedly, this accretion process forces the launch of high velocity bipolar jets which transport considerable amounts of matter and energy away from the star. These jets are found to be highly collimated and comprise clumps, or knots, of material along their flow-axis which gradually fade with distance from the source (Figure 1.1 HH34 panel). Upon impact, these jets shock the surrounding cloud forming HH objects, the morphologies of which are diverse and may vary from a symmetrical bowshock at the head of the jet, to an elongated ionised gas which traces the jet as it propagates, (Figure 1.1 HH47 panel). It is proposed that jets exist as a mechanism for transporting excess angular momentum away from the disk allowing it to slow down and further accrete onto the star. Estimates (both observational and theoretical) suggest that about 10% of the material is ejected and the remainder is accreted. Ultimately, the disk may then accrete onto the star, be dispersed by winds, or condense into a system of planets.

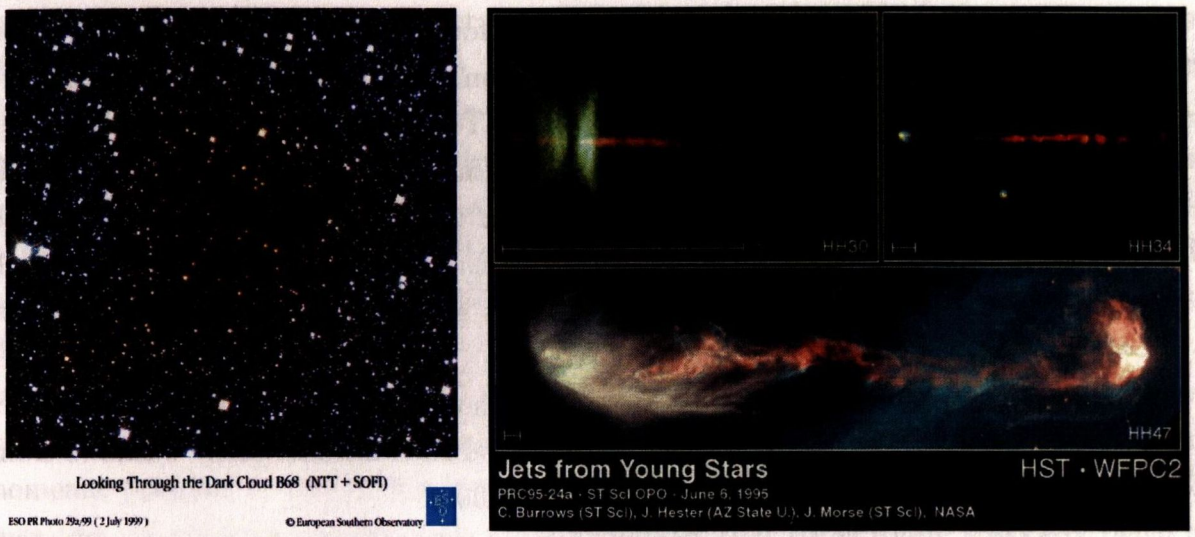

Figure 1.1: ***Left:*** *Barnard 68 globule (starless core) revealed through extincted background starlight.* ***Right:*** *Hubble Space Telescope images* ***HH30-*** *A circumstellar disk surrounding a newly forming star. Light from the star escapes from either side of the dark disk and reflects off the thinner envelope of cloud material which has yet to be dissipated.* ***HH34-*** *A jet comprising clumps of material along its axis, which gradually fade with distance from the source.* ***HH47-*** *An outflow visible at optical wavelengths. The emission originates in shocks resulting from the impact of high velocity jets on ambient cloud material. The infant star is located to the left of the image.*

1.2 Current Understanding

1.2.1 Prestellar Cores

The natural sites of star formation are molecular clouds, since star formation occurs from the gravitational collapse of interstellar material. Cloud complexes were initially discovered in the 1970s though CO millimetre line emission studies and, although their means of formation is not yet understood, they possibly form through more than one mechanism, including spiral density waves, instabilities and compression of the interstellar medium (ISM) by supernovae (e.g. Shu, Adams & Lizano 1987; McCray & Kafatos 1987). They have various sizes, from Giant Molecular Clouds (GMCs) (e.g. Orion), which are 50-100 pc in diameter, of $\sim 10^5$ to $10^6\,M_\odot$ and are found in the galactic arms, to Smaller Molecular Clouds (e.g. Taurus) which are 10-20 pc in diameter, of $\sim 10^3\,M_\odot$ and are found in the galactic disk. Structurally, molecular clouds are very complex. Observations at millimeter wavelengths show that they are clumpy, with high density cores ranging in mass from ~ 1 to $10^3 M_\odot$ appearing in sites of star formation (Blitz 1993). Volume-

averaged H_2 densities range from $\leq 50\,cm^{-3}$ for GMCs (e.g. Blitz 1993) to $\geq 10^5\,cm^{-3}$ for dense cores of sizes 0.03-0.1 pc (e.g. Wilson & Walmsley 1989; Myers 1995). Kinetic temperatures are relatively constant, typically T$\sim$ 10 K (e.g. Pratap et al. 1997) as a result of cooling by CO molecules, but rising by a few factors in star forming regions, particularily in sites where massive stars are formed. Their internal velocity dispersions are generally supersonic with Mach numbers, M, $\geq$10 (e.g. Goodman et al. 1998). When available (e.g. Crutcher et al. 1993), Zeeman measurements give typical values for the magnetic field intensity of a few to a few tens of microgauss (at densities of $n_H \sim 10^3\,cm^{-3}$). Finally, molecular clouds seem to be supported somehow, perhaps by magnetic field turbulence (e.g. Padoan et al. 2004) or through the turbulence introduced by outflows from young stellar objects (YSOs) (e.g. Arce & Sargent 2005).

The formation of dense cores within these molecular clouds can occur via two distinct modes (see Shu et al. 1993 and references therein), i.e. magnetic supercritical or subcritical collapse. Magnetic supercritical collapse of molecular cores occurs when a sufficient density of material accumulates in a given region so that the inward pull of gravity overwhelms the outward pressure of magnetic fields, and then core fragmentation produces ultra-dense sub-cores of stellar mass. Because of this core fragmentation, a mode of star formation thought to be the most efficient (i.e. 5 to 15%), stars are expected to form in clusters such as the Trapezium cluster in Orion. The alternative senario describes core formation via ambipolar diffusion, whereby the neutral gas element of subcritical clumps in a molecular cloud uncouple from the interstellar magnetic field, which would otherwise resist further gravitational collapse. In particular, the interstellar magnetic field acts directly on the ions, but not the neutrals. Therefore, if there is insufficient coupling of neutrals and ions through collisions, the neutrals can slip through the magnetic field, and so the field does not act as a significant brake on collapse. This process occurs slowly, lowering the mass where collapse sets in to about $1\,M_\odot$ (Shu et al. 1987) since only thermal pressure and not the additional outward pressure of the magnetic field has to be overcome by gravitational forces. Although these two alternatives for the formation of dense cores appear viable, many observations of star forming regions suggest that binary and multiple young stars are the rule rather than the exception (e.g. Fuller et al. 1996) and hence implicate fragmentation as the likely mechanism for their formation.

The prestellar stage of star formation may be defined as the phase in which a gravitationally bound core has formed in a molecular cloud and evolves toward higher degrees of central condensation, but no central hydrostatic protostellar object exists yet within the core. More than 100 dark cores have been identified through optical extinction and molecular line studies (e.g. Benson et al. 1998 and references therein). They can be

separated into starless cores and cores with stars, on the basis of the absense or presence of an embedded source detected in the infrared. Many have been found to have larger sizes than, but masses comparable to, the youngest protostars (Class 0 sources, see Subsection 1.2.2 below) (Ward-Thompson et al. 1999). This is consistent with starless cores being prestellar in nature and the precursors of protostars. Prior to the start of protostellar collapse, cores are supported against self-gravity by a combination of thermal and magnetic pressure. Observations of several dozen dense cores reveal mean axial ratios of about 0.6, thus favoring a prolate shape when deprojected from the plane of the sky. Interestingly, this shape is favoured theoretically as a progenitor for binary stars. Stellar mass fragments in gravitationally collapsing GMC cores typically develop specific angular momenta (angular momentum per unit mass), but analysis of Doppler shifted spectral lines (e.g. in tracer molecules such as NH_3) implies that cores rotate so slowly (with a period of $2\pi/\omega \approx 6\times10^6$ yr) that the associated centrifugal force is negligible compared to the self-gravity and pressure gradients. However, the true significance of this initial rotation lies in its effect on later collapse.

1.2.2 Young Stellar Objects (YSO)

The prestellar stage of star formation ends with the formation of an opaque, hydrostatic protostellar object in the centre. The formation of low-mass stars then enters a series of four conceptually different further stages (e.g. Larson 1969; Shu et al. 1987), Figure 1.2. The distinction between each stage is not exactly precise, but is aided by classing sources according to their near-infrared excess, Figure 1.2 right panel.

Following subcondensation of the clumps of cloud material into starless cores, Figure 1.2 (a), each core further contracts and any initial rotation of the cloud material is amplified. This leads to a spinning of the core (now a Class 0 source, Figure 1.2 (b)) and the formation of a circumstellar accretion disk. In contrast to prestellar cores, Class 0 protostars are always found to be strongly centrally condensed, although they are still a factor of $\geq$10 less massive than their surrounding circumstellar envelopes (e.g. Motte et al. 1998). The system now enters the main phase of accretion, during which the central object builds up its mass (initially $\sim10^{-2}\,M_\odot$) from the surrounding infalling envelope and accretion disk, while progressively warming up. The embedded star is not optically visible, since it is surrounded by an envelope of cloud material, and can only be studied at infrared, submillimeter or millimeter wavelengths. The initial burst of rapid accretion lasts less than 10^4 years, while the time taken for half of the envelope to be accreted is about 10^5 years, and nearly all of the envelope is accreted within $\sim10^6$ years. All the energy from the YSO is from contraction although, during the protostellar accretion phase, stars more massive

than a few 0.1 $M_\odot$ start burning deuterium (at core temperatures of $\sim 10^6$ K) whereas stars with masses in excess of $\sim 8\,M_\odot$ begin to burn hydrogen (which begins at 10^7 K) (see Palla & Stahler 1991). Unexpectedly, observations have shown that the main accretion phase is always accompanied by a powerful ejection of ~10% of the accreted material in the form of prominent bipolar jets or outflows. As the process advances, the circumstellar envelope depletes as it falls onto the disk or is blown away by the power of the outflow, allowing the bipolar jet to become optically visible (Class I sources), Figure 1.2 (c). In contrast to Class 0 sources, the star (not the accreting disk/envelope) possesses the majority of the mass in a Class I protostellar system. The decreased accretion activity leads to a decrease in ejection activity, and so while Class 0 sources drive powerful outflows (e.g. Bachiller 1996), the outflows from Class I sources tend to be much less powerful and less collimated. With the further depletion of disk material, the driving force of gravitational accretion lessens and the jets become weaker still. When the central object has accumulated most ($\geq$ 90%) of its final main sequence mass, it becomes a pre-main sequence star (Class II source), Figure 1.2 (d). The central star gradually becomes optically visible and, depending on mass, is classed as a low mass Classical T Tauri star ($< 2\,M_\odot$), an intermediate mass Herbig Ae/Be star (2 - 10 $M_\odot$), or a high mass star ($> 10\,M_\odot$). Finally, the infalling envelope disappears and accretion/ejection abates, leaving the remains of a circumstellar disk which may then condense into a system of planets (around this Class III source). It is possible that this stage represents the observed Weak-line T Tauri stars, which have narrower equivalent widths in Hα emission, a known tracer of accretion activity. Once most ($\geq$ 90%) of the star's energy output is derived from hydrogen fusion, it graduates to a zero-age main sequence star. The internal pressure then exactly balances gravity so that the star can begin a long-lived phase of overall equilibrium on the main sequence.

Classical T Tauri stars were the first pre-main sequence stars to be identified (Joy 1945, Ambartsumian 1957). Characteristically, they have an associated infrared emission attributed to the disk and dusty halo, as well as excess continuum emission in the ultraviolet. Their spectra display strong permitted lines, e.g. Balmer and Ca II lines, and strong forbidden emission lines (FELs), e.g. [O I]λ6300 and [S II]λ6716. Where absorption lines are present, they are often partially filled-in (or 'veiled') by accretion shock emission. In contrast, Weak-line T Tauri stars have emission line fluxes consistent with active stellar chromospheres, and appear to rotate faster (Edwards et al. 1993), a fact attributed to the lack of MHD disk braking. Meanwhile, Herbig Ae/Be stars are thought to be the intermediate mass counterparts of T Tauri stars (Corcoran & Ray 1997a), showing similar infrared excess emission and FELs. A further characteristic of young, pre-main sequence stars is both regular and erratic variability in their emission, including flaring at optical

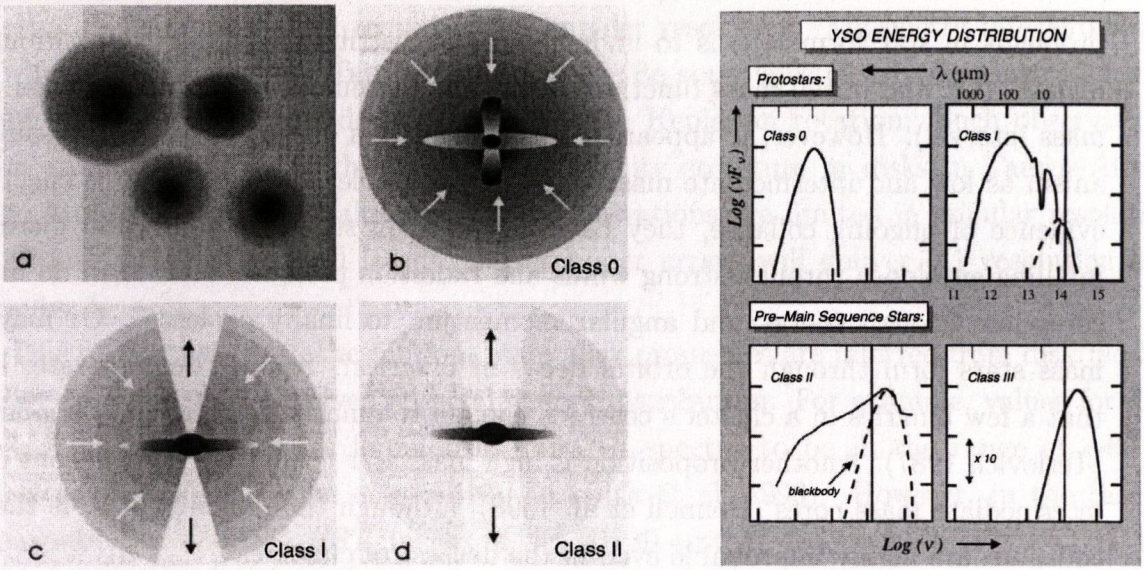

Figure 1.2: Panels (a) to (d): *Stages of Star Formation: (a) fragmentation of the cloud material into clumps and then cores, (b) the formation of a circumstellar disk and the initial launch of a bipolar jet, (c) depletion of the circumstellar envelope as the jet advances, (d) further depletion of the envelope and reduced accretion/ejection activity;* **Right panel:** *Classification scheme of YSO spectral energy distributions, (a vertical line appears at 2.2 μm as a reference between panels). Classes 0 and III have distributions whose widths are similar to single temperature blackbody functions, while Classes I and II display infrared excess (Lada, 1999).*

wavelengths e.g. the class known as EXors displays large outbursts on decade time scales (e.g. Coffey, Downes & Ray 2004), while FU Orionis stars exhibit the most dramatic changes with luminosity increases of two orders of magnitude in the course of a year or so. These outbursts, of unknown origin, occur repeatedly during pre-main sequence contraction.

Understanding the stages of high mass star formation has proved more difficult since, although they are more luminous, high mass stars are generally so far away that the surrounding cloud structures do not allow high resolution studies. Moreover, since observations are statistically unfavorable, in that these sources must disperse their parent clouds in a time short comparable with lower mass objects, it is difficult to witness the actual birth of a high mass stars. Furthermore, although variations in environmental factors such as the ambient magnetic field, or the molecular cloud temperature prior to core formation, could in principle yield a variety of mass distributions, massive stars are somehow intrinsically rarer than their low-mass counterparts. In fact, one of the unsolved

problems in star formation is to understand the distribution at birth of various stellar masses, (i.e. the initial mass function, defined as the number of stars produced per unit mass interval). However, it appears that massive stars do not form via the same mechanism as low and intermediate mass stars. For example, although there is spectroscopic evidence of ongoing collapse, they have no pre-main sequence phase and disrupt their infalling envelopes through strong winds and radiation pressure. How then do high mass cores lose enough energy and angular momentum to finally coalesce? Or maybe high mass stars form through the orbital decay of binaries? Studies demonstrate, however, that a few binaries in a cluster's centre is enough to quickly disperse the remaining stars (Terlevich 1987). Another proposition is high mass star formation via collisions of low or intermediate mass cores (Bonnell et al. 1998), although the difficulty here is that direct collisions are highly improbable even in the densest of clusters.

1.2.3 Circumstellar Disks

Circumstellar disks were first detected indirectly in a variety of ways, such as infrared excess emission in spectral energy distributions (e.g. Cohen et al. 1984), interferometric imaging at near infrared (e.g. Beckwith et al. 1984) and millimetre (e.g. Sargent & Beckwith 1987) wavelengths, polarisation mapping (e.g. Bastien et al. 1988; Piirola et al. 1992), and the absence of redshifted outflows close to the source interpreted as obscuration by the presence of a disk (Appenzeller et al. 1984; Edwards et al. 1987). The many diverse observations were reconciled with each other only by invoking a flattened disk of dust and gas around the young star (see Beckwith & Sargent 1996 for review). The first direct observations of the proto-planetary disks surrounding young stars were made only as recently as 1992. Conducted with the *Hubble Space Telescope (HST)*, these imaging observations were of circumstellar disks embedded in the Orion Nebula (O'Dell et al. 1993; O'Dell & Wen 1994), and were detected in silhouette against the background light their young star. Since then, *HST* observations have demonstrated that circumstellar disks are common among low mass young stars (McCaughrean & O'Dell 1996).

For typical temperatures of $\sim$10 to 50 K (at a radius of $\geq$100 AU from the star), disk material will radiate preferentially in the millimetre wavelength region. Therefore, millimetre and thermal-infrared observations directly image the gas and warm dust in a disk in emission, while optical and near-infrared observations rely on either dust scattering or absorption. The clear observational challenge is that disk diameters, which are typically $\sim$ 50 to 500 AU for the Orion Nebula, require subarcsecond angular resolution given that the distance to the Orion GMC is $\sim$500 pc. The situation is somewhat improved for nearby star-forming regions such as Taurus-Auriga ($\sim$ 140 pc), although resolution of the

internal disk structure still requires high angular resolution. Millimetre interferometric CO line observations of T Tauri and Herbig Ae/Be stars have clearly demonstrated that many of them are surrounded by large disks in Keplerian rotation. Such observations have given indications of the density and velocity structure in disks in Taurus-Auriga (e.g. Mundy et al. 1996), although these observations are limited in angular resolution to about 1″, while planned larger interferometer arrays will deliver 0.″1 resolution (see Chapter 6).

Due to limiting spatial resolution, many disk properties are inferred from disk models which reproduce the observed spectral energy distribution. For example, values for disk surface temperatures were found from infrared spectra to be in the range of ∼60 to 400 K with a typical value of ∼150 K (Beckwith et al. 1990). However, in the case of subarcsecond resolution *HST* images of the HH 30 system, for example (Figure 1.1), the disk surface temperature can be derived directly from the observed disk morphology (Burrows et al. 1996). This disk, like many others, is found to become thicker (or 'flare') with increasing radial distance. The observed half-thickness of the disk (i.e. a height of ∼15 AU at r=100 AU) suggests a disk surface temperature of 34 K. Depending on mass accretion rates, which are estimated to lie in the range of 5×10^{-8}-10^{-6} $M_\odot$, the disk surface temperature would rise to 80 K at distances of 1-5 AU respectively from the protostar (Boss 1998). In terms of disk mass, Boss (1998) inferred a relatively low value of 0.006 $M_\odot$. By comparison, millimeter survey data (Beckwith et al. 1990) revealed an average disk mass of 0.02 $M_\odot$, calculated from a range of values spanning 0.001 to 1 $M_\odot$.

Planets, or at least their cores, form through the aggregation of grains within a circumstellar disk. The discovery of extra-solar planets confirms that the formation of these objects is a common occurrence in solar-type stars. The first planet discovered using the Doppler technique (Mayor & Queloz 1995) has been interpreted as a gas giant (with mass of at least $\sim 0.5\,M_J$) orbiting at ∼0.05 AU from its solar-type star. Given that the midplane temperatures in the disk would have exceeded 1 500 K at this distance, it seems likely that the planet formed further from the star and migrated inwards to its present location through interactions with the disk or with other planets (Boss 1998). Several extrasolar gas giant planets have been detected with orbits much more similar to that of Jupiter, ranging from 2-7 AU from their stars (Butler & Marcy 1996; Cochran et al. 1996). The overall aim is to identify the conditions in proto-planetary environments, and perhaps detect indirect signatures of on-going planet formation. The ultimate goal would be to find extraterrestrial life.

1.2.4 Bipolar Jets and Outflows

The striking phenomena of jets and outflows was wholly unanticipated by theorists, who are still struggling to understand the basic mechanism. Since they are observed to transport significant amounts of energy and momentum away from the central source, it is likely that they play an important role in the evolution of the parent star. Furthermore, stellar birth is often hidden from view and since jets and outflows can be more easily observed, they offer a 'fossil record' of the star's history.

Bipolar ejecta from young stars can be considered in terms of two classes: optically visible highly collimated atomic jets which travel at velocities of a few hundreds of kilometres per second; and less collimated molecular outflows (primarily seen in trace molecules such as CO and SiO) which travel at velocities of a few tens of kilometres per second and are detectable at millimetre wavelengths. The relationship between the two has been extensively debated during the past two decades (e.g. Cabrit et al. 1997). Some suggest that the initial jet collects gas from its surroundings through either 'prompt entrainment' when the jet rams into the molecular cloud material head-on (Richer et al. 2000), 'steady entrainment' occuring within the shear layer along the jet (De Young 1986), or interactions of a non-steady jet with the cloud due to variations in jet velocity or orientation (e.g. Suttner et al. 1997). The opposing view is that the jet is simply the denser core of a wider angle wind. It sweeps up the ambient material, via a forward shock, which runs ahead of the wind bubble and this produces the molecular outflow (e.g. Shu et al. 2000).

Regardless of the exact distinction or relationship between jets and outflows, the resulting shocks are observed as ionised nebulae (i.e. HH objects/flows, as mentioned in Section 1.1). While some form clear bowshocks and others have a distinct jet morphology, many are more chaotic in shape. The first jets/outflows to be recognised as such were from HL Tau, HH 30 and DG Tau (Mundt & Fried 1983), while today a large number of HH flows are known (Reipurth & Bally 2001) and tend to occur in groups since star formation occurs in clusters (Bally et al. 1996).

Observationally, imaging and spectroscopic studies have provided a detailed understanding of morphology, kinematics and diagnostics, although many studies centre on low mass stars as they are closer and more abundant. Jets and outflows have a wide variety of scales, with lengths on the order of a few thousand AU although parsec-scale outflows have also been observed (Ray 1987; Bally & Devine 1994; McGroarty et al. 2004). Jet diameters range from $\sim$70 to 140 AU (i.e. $\sim$0.″5 to 1″) for the nearest flows (Ray et al. 1996), and have varying degrees of collimation from wide angle winds to narrow jets. Full opening angles are in the range of 10° to 30° close to the source ($\leq$50 AU), followed by re-collimation by a few degrees within 100 AU of the protostar (e.g. Ray et al. 1996;

Dougados et al. 2000). The flows exhibit axisymmetric expansion patterns and can persist for 10^5 years for low mass stars, although this is possibly a lower limit given that the true extent of many outflows is not necessarily known. Many jets have been observed to oscillate in the transverse direction as they propagate (e.g. López et al. 1995). Typical variations in angle are anything up to $\sim$10°, an effect interpreted as either jet precession associated with the presence of a companion star, or instabilities within the jet itself. Depending on the source luminosity, jet radial velocities typically range from ~ 200 to $1\,000\,\mathrm{km\,s^{-1}}$ which is larger than the sound speed, c_s, in the surrounding medium (i.e. $c_s \propto \sqrt{T} \propto \sqrt{10\,K} << 10\,\mathrm{km\,s^{-1}}$). Therefore, Mach numbers, M, (i.e. the ratio of jet velocity to ambient sound speed) are in the range of ~ 20 to 100, i.e. jets are hypersonic and so cause shock phenomena. They also incorporate clumps, or 'knots', which have lengths of a few hundred AU and exhibit large proper motions. These knots are most likely due to variations in ejection velocity of the jet material from the source, which can cause internal jet shocks that propagate along the jet (e.g. Suttner et al. 1997). Typical jet temperatures are in the range of 5×10^3 to 10^4 K (and so jet sound speeds are ~ 10 to $30\,\mathrm{km\,s^{-1}}$), while electron densities are found to be in the range of 10^2 to $10^4\,\mathrm{cm^{-3}}$. Only a small fraction of the jet is ionised, i.e. $\sim$10% (Bacciotti et al. 1995), but the ionising agent is as yet unknown. Ionisation can occur collisionally through the shocks but, given that bowshock velocities of $\sim 100\,\mathrm{km\,s^{-1}}$ can explain collisional ionisation of only $\sim$3%, interal jet shock velocities of typically ~ 30 to $40\,\mathrm{km\,s^{-1}}$ cannot explain the 10% level. Furthermore, low mass young stars are too cool to allow photoionisation although x-ray emission from the magnetospheric accretion shock offers a possible explanation.

Finally, strong observational links have been established between accretion and ejection processes. A strong correlation is found (e.g. Cabrit et al. 1990; Cabrit & André 1991; Hartigan et al. 1995) between the presence of outflow signatures (such as P Cygni line profiles, FELs, or well-developed molecular lobes) and accretion diagnostics (such as ultraviolet, infrared and millimetre wavelength emission excess, or inverse P Cygni line profiles). For example, jet mass fluxes are $\sim 10^{-9}$ to $10^{-7}\,\mathrm{M_\odot yr^{-1}}$ depending on source luminosity (Edwards et al. 1993), while typical estimates of accretion rates ($\sim 10^{-8}$ to $10^{-6}\mathrm{M_\odot/yr}$) are around 10 times larger (Hartigan, Edwards & Ghandour 1995). Further support is provided by the apparent decline in outflow activity with stellar age, which follows a similiar trend in disk frequency (Mundy et al. 2000) and mass accretion rate (Calvet et al. 2000). At least some low mass YSOs undergo occasional FU Ori outbursts, with rapid disk accretion (up to $10^{-3}\,\mathrm{M_\odot yr^{-1}}$) accompanied by a strong disk wind with high mass loss rates ($\sim 10^{-5}\,\mathrm{M_\odot yr^{-1}}$), which more than likely affects the energetics and morphology of the large-scale flow (see Hartmann & Kenyon 1996 for review).

1.3 Aim of this Thesis

1.3.1 Context and Structure

The importance of understanding accretion/ejection structures is highlighted by the ubiquity of jets in other astrophysical phenomena (e.g. jets from x-ray binaries, pulsars, symbiotic stars and planetary nebulae; and active galactic nuclei jets associated with quasars, blazers and gamma ray bursts). By providing protostellar jet models with observational constraints, other types of astrophysical jets may be confronted with scaled versions of these models.

While much progress has been made in recent decades there are many outstanding questions to be answered, including how jets/outflows from young stars are launched and travel away from their source. Long-standing observational difficulties lie in the fact that young stars are often heavily embedded. Furthermore, due to the relatively small spatial and temporal scales, physical properties of jet/outflows can only be deduced from high angular resolution data. Consequently, to overcome these obstacles, this work focusses on more evolved, and hence less embedded, T Tauri stars and harnesses the high spatial resolution of *HST* at optical and near ultraviolet (NUV) wavelengths. In this way, this thesis constitutes an observational contribution to understanding jet generation and propagation.

First, I examine the case of the pre-main sequence star XZ Tauri and its outflow. I describe imaging observations of the binary system and its outflow, and how each has evolved over a six year period. Using my proper motion results in combination with typical outflow parameters, I was able to guide simulations so that other parameters could be inferred.

I also conduct a spectroscopic survey, at optical and NUV wavelengths, of several T Tauri star jets. I examine the base of these jets close to their sources, in order to determine the radial velocity profile across the jet immediately after it has been launched from the star/disk system. In this way, I provide further constraints for theoretical models, and attempt to differentiate between currently proposed models of jet generation.

Therefore, this thesis can be considered in terms of two main divisions, namely, pre-main sequence outflow propagation (Chapter 3), and pre-main sequence jet launch (Chapters 4 and 5). Chapter 2 is therefore divided into two separate sections which discuss the theory of each. And, finally, Chapter 6 draws together the conclusions and outlines the next steps for future research.

1.3.2 Angular Resolution Demands

The diffraction limit, the physical limit for spatial resolution given by the Rayleigh Criterion, may be extended by using a larger telescope mirror diameter and/or observing at shorter wavelengths. Currently, the largest ground-based optical/infrared telescopes have mirrors of 8 to 10 m in diameter but, practically, atmospheric turbulence dominates over diffraction in degrading the image. As a result, current non-adaptive optics ground-based observing is limited to achieving spatial resolutions of about 1″ at optical wavelengths. However, improvements are in sight for the near future through the development of adaptive optics and interferometric techniques for infrared and eventually optical telescopes.

Meanwhile, the current resolution of standard ground-based proper motion studies of outflows from YSOs demands relatively long time intervals between observations. Outflow velocities are on the order of 100 to 200 $\mathrm{km\,s^{-1}}$ and so, for an angular resolution of 1″, typically a five year time interval is necessary for even the nearest outflows (140 pc) while more distant objects required intervals of several decades. Meanwhile, as will be seen in Chapter 3, outflows observed at one year intervals with the diffraction-limited spatial resolution of *HST* (i.e. 0.″1 when imaging at optical wavelengths) have exhibited dramatic changes on such timescales.

Furthermore, given that jet widths are typically about 1″, only high resolution observations can examine the jets' internal structure, and thus attempt to differentiate between models currently proposed for jet formation. The combination of *HST*'s subarcsecond spatial resolution with its good spectral resolution (R = 30 000 in the near ultraviolet and 5 000 to 10 000 in the optical region) allows a detailed analysis of the internal jet structure, as will be seen in Chapters 4 and 5.

Consequently, it is clear that many studies of the circumstellar environment in star forming regions require the high spatial resolution of *HST*.

1.3.3 Instrumentation

All observations were conducted with instruments aboard *HST*, launched in 1990 into a low Earth orbit and now possibly in the final years of its useful life. The payload comprises four science instruments (some of which have been replaced or upgraded during periodic servicing missions) providing data from the infrared to the ultraviolet region of the spectrum. The current instruments are the Advanced Camera for Surveys (ACS), the Near Infrared Camera and Multi Object Spectrometer (NICMOS), the Wide Field Planetary Camera 2 (WFPC2) and the Space Telescope Imaging Spectrograph (STIS), Figure 1.3. The latter two instruments were used to obtain imaging and spectroscopic

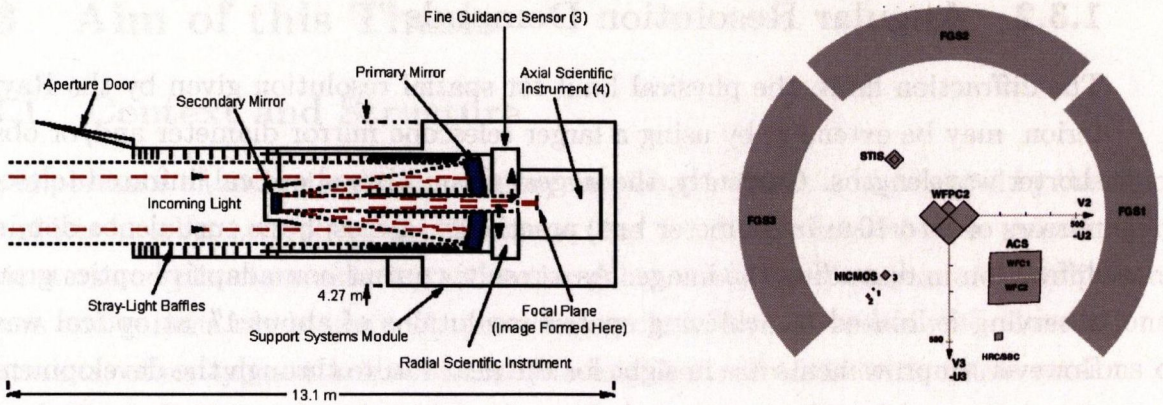

Figure 1.3: ***Left:*** *Schematic of the HST optical design.* ***Right:*** *Schematic of the HST focal plane layout, showing each of the four instruments surrounded by the the Fine Guidance Sensors. (http://www.stsci.edu/hst/)*

data, respectively, for this research.

WFPC2, which replaced the original WFPC in the 1993 servicing mission, comprises four (800×800 pixel) cameras and provides images over a broad wavelength range (1 150 to 11 000 Å). The WFPC2 detector comprises four front-side illuminated CCDs. It simultaneously images a $150'' \times 150''$ region using three cameras forming an L-shape with a spatial sampling of $0.''1\,\text{pixel}^{-1}$ (referred to as Wide Field Cameras 2, 3 and 4), and a smaller $34'' \times 34''$ square field with one smaller camera of spatial sampling $0.''046\,\text{pixel}^{-1}$ (refered to as Planetary Camera 1). Each observation results in a mosaic of images from the four cameras. The instrument contains a total of 48 filters, which include a set of broad band filters approximating Johnson-Cousins UBVRI, as well as a set of wide U, B, V, and R filters, and a set of medium bandwidth Strömgren u, v, b, and y filters.

STIS, installed in 1997 and operating until its power supply failure in 2004, provided images and spectra at optical and ultraviolet wavelengths. It has three (1024×1024 pixel) detectors: a back-illuminated CCD for observations from 2 000 to 10 300 Å with spatial sampling of $0.''05\,\text{pixel}^{-1}$ over a $52'' \times 52''$ field of view; and two Multi-Anode Microchannel Array (MAMA) detectors operating in the NUV region from 1 600 to 3 100 Å and the far ultraviolet from 1 150 to 1 700 Å, with spatial sampling of $0.''029\,\text{pixel}^{-1}$ over a $25'' \times 25''$ field of view. For each detector, there is a choice of first-order and echelle gratings, several filters , and various apertures. Finally, both WFPC2 and STIS contain internal corrective optics to account for the well known spherical aberration of the *HST* primary mirror.

While this section provides an overview of the relevant *HST* instrumentation, the specific instrument configurations used for the observations are detailed in the appropriate chapters.

2

Overview of Theory

This chapter outlines the basic physics governing jets/outflows from young stars, in order to give a context for my observational research and an understanding of its significance.

2.1 Theory of Shock Formation

2.1.1 Mechanism of Shock Formation

Shocks form when a jet encounters the surrounding interstellar medium (ISM) at supersonic velocities, i.e. $M > 1$ but typically 10 to 30. As the jet material runs into the ambient cloud, it produces a two shock system. The reverse shock (or 'Mach disk') forms where the jet material is decelerated, while the forward shock (or 'bowshock') forms where the ambient material is accelerated. The gas immediately behind each shock is compressed, heated and ionised. The post-shock gas resides between the shocks in two layers separated by a boundary called the 'contact surface' or 'contact discontinuity'. There is no pressure gradient across the boundary, and so there is no flow of material across it. The shock velocities (in the shock reference frame) are noted in Figure 2.1, left panel.

The hot inter-shock layer then immediately undergoes rapid radiative cooling. The distance behind the shock over which this takes place, the cooling length, is small (i.e. $\sim\frac{1}{10}$ of the shock size). Lines from various species are emitted at varying distances from the

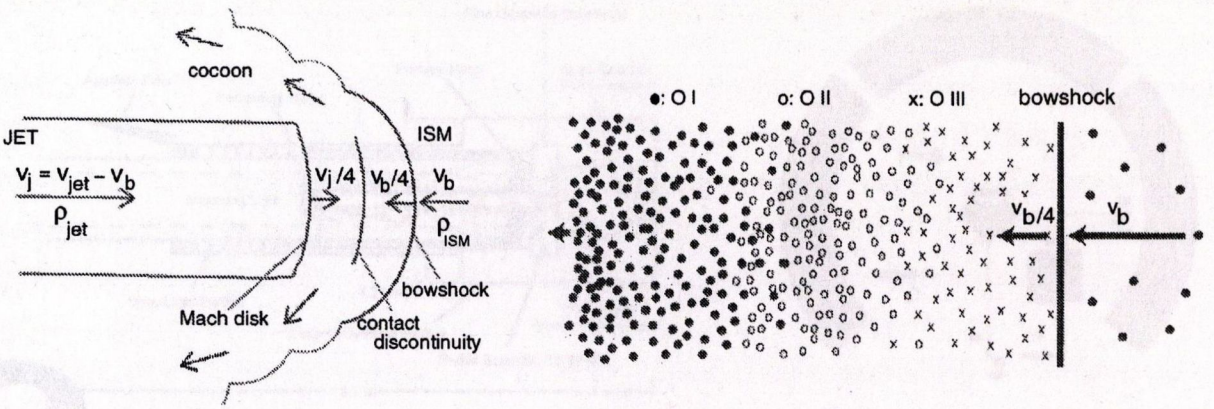

Figure 2.1: ***Left Panel:*** *Schematic of a jet interacting with the surrounding ISM, drawn in the bowshock reference frame. The result is a cocoon region containing shocked jet and ISM material with a contact surface between the two. Material enters the shock front from the right with a velocity, v_b, and is slowed by a factor of 4 after crossing the shock. The density jumps by a factor of 4 at the shock and increases as the gas cools, recombines and slows.* ***Right Panel:*** *The structure of a radiative shock, drawn in the bowshock reference frame. As an example, cooling zones of various oxygen species are depicted by the crosses, circles and dots (Hartigan et al. 2000).*

front, according to excitation conditions. In particular, strong Hα emission denotes the position of shock fronts in outflows, while emission such as O III is followed by O II and O I (Figure 2.1 right panel). Forbidden lines such as [O I]λ6300, [N II]λ6583 and [S II]λ6731 are also emitted in the post-shock gas. With no pressure gradient, the rapid decrease in temperature causes a corresponding increase in density. The result is a dense build-up of material just beyond the cooling distance. Both the forward and reverse shock contribute to this density build-up, and so there is a very large compression of matter such that most of the material in the region resides close to the contact surface. Momentum conservation implies that the increase in density causes a decrease in velocity, and so the cooled dense layer now decelerates (in the bowshock frame) to the same speed as the forward shock, i.e. from $-\frac{1}{4}v_{bow}$ to zero. Thus, in the ambient frame, it accelerates from $\frac{3}{4}v_{bow}$ to v_{bow}.

So far I have described high velocity 'jump-shocks' (J-shocks), in which temperature, density and velocity experience a discontinuous jump at the shock surface. This causes dissociation of any molecules, assuming shock velocities greater than 10 to 20 km s^{-1}, leading to a spectrum dominated by atomic emission lines. However, depending on the gas velocity, magnetic field strength and ion density, another type of shock may form. 'Continuous shocks' (C-shocks) occur when the Alfvén velocity is greater than the neutral shock velocity, so the magnetic field transmits energy at a speed greater than that of

the neutral shock. In this case the temperature, density and velocity experience a less abrupt, more continuous change and molecules can play an important role in the cooling process. The formation of C-shocks occurs as follows. Low ionization from cosmic rays is expected in the interior of molecular clouds, which is shielded against ionizing radiation from OB stars. If the ionization fraction is low enough, the ions are not well coupled (through collisions) to the neutrals any more and the gas then has to be treated as a two-component fluid. The speed of signal propagation in the ion fluid, which is of the order of the ion Alfvén velocity, can be much larger than the sound speed of the neutrals. The ion fluid is then continuously accelerated and compressed, and friction between the ion and neutral fluids leads to acceleration and heating of the neutral fluid before the neutral jump-shock arrives. Depending on the field strength and cooling efficiency, the magnetic precursor may eventually lead to a continuous static compression of the neutral gas to its post-shock properties without the presence of a jump. This is a C-shock. Therefore, for C-shocks the kinetic energy dissipation is a much more gradual process than for J-shocks, and is spread over a much larger volume. This leads to a much lower temperature in the shocked gas for a given shock velocity. H_2 and other molecules can thus survive much faster C-shocks than J-shocks.

Both J and C shocks may be present *within* the jet, appearing as bright clumps of material along the flow axis, and most likely occuring due to variations in the ejection velocity of jet material at the source, Figure 2.2. For example, Reipurth & Heathcote (1991) observed bright clumps embedded in the flow of the HH 46/47 jet, and interpreted them as internal jet shocks (i.e. 'internal working surfaces') which they explain in terms of multiple ejections from the embedded energy source. These results were successfully reproduced by Raga et al. (1990) using analytic and numerical models for jets with variable velocity ejection. They find that variations in the source velocity induce the formation of discontinuities in the jet which can be described as internal working surfaces.

Figure 2.2 (Raga et al. 1990) shows a schematic diagram of the structure of internal working surfaces in jets. The working surface moves with a velocity, v, that satisfies $u_1 > v > u_2$ (where u_1 and u_2 are the upstream and downstream flow velocities, respectively). The high pressure between the two shocks of the working surface drives out material sideways, and the interaction of the ejected gas with the surrounding environment forms a bowshock.

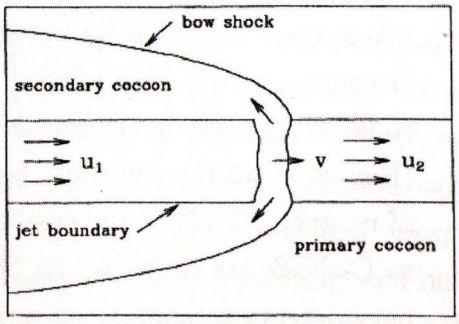

Figure 2.2: *Schematic diagram of an internal working surface.*

2.1.2 Numerically Simulating Outflow Shocks

Studies of cloud-shock interactions require numerical simulations to understand the detailed physics, a task which is computationally demanding and so advances parallel the development of computing power and sophisticated algorithims.

Extensive numerical simulations of supersonic jets had been carried out for adiabatic flows (e.g. Norman et al. 1982), in order to model observations of highly collimated jets in extended radio galaxies (e.g. Jennison & Das Gupta 1953). However, they were not directly relevant to YSO jets, because the strong departure from adiabaticity in a radiatively cooling jet can significantly modify the structure of the flow (Blondin et al. 1990). For example, in addition to the basic two-shock morphology of adiabatic jet heads, the first numerical models for radiatively cooled jets found that they develop a dense shell between the jet shock and the leading bow shock (Blondin et al. 1989), as described in Section 2.1.1.

Outflow modeling is constrained by the narrow range of acceptable outflow parameters (e.g. density, velocity, excitation etc.), which are in turn derived from diagnostic (forbidden and permitted) lines observed at various distances from the outflow source. In the ideal case, the ambient medium is assumed to have an undisturbed, simple structure with no clumps, magnetic fields or ionisation stages, and the jet is assumed to be axisymmetric. For example, simulations were conducted in Chapter 3 by choosing a box size in which ambient medium parameters were defined, i.e. we choose the velocity of the ambient medium to be zero, a typical ambient density, and an unchanging gas pressure which yields a realistic value for the ambient temperature. The jet is allowed to enter the box from one side and is given initial jet parameters of velocity, density and opening angle. The hydrodynamic code then derives the behaviour of the jet from the four Euler equations (i.e. the conservation of mass, momentum, energy and the equation of state).

While hydrodynamic jets with and without radiative losses have been well-studied (e.g. Raga 1988; Blondin et al. 1990; Stone et al. 1993; Raga et al. 1995), magnetised jets subject to collisionally excited radiative losses are only now being investigated (e.g. Cerqueira et al. 1997; O'Sullivan & Ray 2000; Cerqueira et al. 2004). Nevertheless, considering that direct measurements of magnetic fields have proved difficult to obtain (Ray et al. 1997), the code described in Chapter 3 is purely hydrodynamic. The addition of magnetic fields to the system has the capability to change the shock type from J-shock to C-shock (as described in Section 2.1.1), but the resulting morphology and diagnostic parameters can equally be reproduced by changing input parameters in a hydrodynamic code, and so are not necessarily an immediate indicator of the influence of a magnetic field.

The results of the simulations in Chapter 3 indicate the presence of several instabilities. The Rayleigh-Taylor Instability (e.g. Blondin et al. 1992) occurs when a dense, heavy fluid is accelerated by a light fluid, as is the case in the vicinity of the contact surface when $\rho_{jet}/\rho_{ISM} < 1$. Such instabilities are quelled by any sort of restoring force. In astrophysical situations, a magnetic field applies a certain amount of tension and can inhibit instability growth. On this point, it should be reiterated that the simulations in Chapter 3 are purely hydrodynamic. The Kelvin-Helmholtz Instability (e.g. Downes & Ray 1998) results from velocity shears between two media, which are not necessarily of different densities. When this comes into play it occurs either along the sides of the jet (incompressible modes) or in the body of the jet (compressible modes). However, this is not apparent in the simulations of Chapter 3, due to the high Mach number (i.e. $M \sim 25$) and short dynamical timescale. As with the Rayleigh-Taylor Instability, any type of surface tension will hinder the Kelvin-Helmholtz Instability for incompressible flows. The result is that instability is only present if the velocity shear is greater than the Alfvén velocity (Chandrasekhar 1961). Finally, a medium that is shocked and compressed from two sides will produce a wavy structure known as the Vishniac Instability (Vishniac 1994; Dgani et al. 1996). Compression from one side is due to thermal pressure, which acts normally, and from the other is due to ram pressure, which acts obliquely giving a transverse resultant force that drives material into peaks and valleys in the compressed region. The denser valleys will be decelerated less than the rarefied peaks, leading to oscillations.

2.2 Theory of Jet Launch

2.2.1 The Angular Momentum Problem

According to the law of conservation of angular momentum, the inward falling matter of an accretion disk must have increasing angular velocity with decreasing radius. As has long been recognised, the amount of angular momentum in a typical star forming cloud core is several orders of magnitude too large to be contained in a single star, even when rotating at break-up speed. This is the classical 'angular momentum problem' of star formation (Mestel & Spitzer 1956, Bodenheimer 1978, 1995). If angular momentum is not somehow transported away from the protostellar system, the star's rotation would reach unreasonably high speeds. We can then infer that angular momentum *must* be transported away from the accreting system, thereby keeping the star rotating well below break-up velocity, as observed. Consequently, with the first observations of protostellar jets in the 1980s, it was proposed that jets and outflows from newly forming stars somehow

extract angular momentum from their source (e.g. Pudritz & Norman 1983). The strong correlation between outflow signatures and accretion diagnostics appears to support this supposition. But, while the disk/jet connection is well established (e.g. Cabrit et al. 1990), the origin of the jet and its driving mechanism remain topics of intense debate (see review by Cabrit 2002).

The theoretical foundations for how outflows can lead to angular momentum loss had already been laid by the 1960s. The prediction of a steady, radial, structureless wind driven by the thermal gas pressure gradients in a star's corona (Parker 1958), was soon followed an adapted model which incorporated open magnetic field lines (Parker 1965) in order to explain subsequent observations of clearly very *structured* winds. Following this, Weber & Davis (1967) developed the basic equations for magnetic rotator theory in which the combined effects of rotation and magnetic fields were investigated. One of the most important effects of such a wind is the enhanced loss of stellar angular momentum.

Building on these foundations, many models have been proposed for the extraction of angular momentum through the launch of protostellar jets. These rely on driving forces such as thermal pressure, radiation pressure and magneto-centrifugal forces. Both mass and momentum fluxes of the observed outflows are much higher than could be derived from the protostar's luminosity, hence forbidding both thermal and radiation pressure driven outflows (DeCampli 1981, Königl 1986). The third option proposes the combined launching effect of magnetic fields and centrifugal forces, and appears to provide a natural explanation for the long standing problem of angular momentum dissipation in protostars.

Aside from the role of the bipolar jet, the contribution of viscous forces in the disk to angular momentum transport is as yet unknown. Astrophysical disks are too large for ordinary particle viscosity to play a significant role in angular momentum extraction from the disk. This is due to the fact that the timescales on which disturbances are propagated by viscous diffusion are orders of magnitude too long for the time variability seen in accretion disks. A long-standing challenge of the theory of accretion disks, therefore, has been to find a mechanism capable of generating a turbulent viscosity within the disk, which in turn could be responsible for angular momentum transport. There are ongoing attempts to isolate instabilities that may lead to the generation of disk turbulence (see reviews by Papaloizou & Lin 1995, Lin & Papaloizou 1996, Balbus 2003).

For example, assuming a large Reynolds number allows differential rotation to turn into shear-driven turbulence (Crawford & Kraft 1956, Shakura & Sunyaev 1973). In other words, assuming the presence of a sufficiently strong viscous stress then, since an accreting disk is a differentially rotating object and angular velocity decreases with increasing radius, the inner parts of the disk will shear past the outer parts. This frictional force

has the effect of transporting angular momentum outwards, thus allowing accretion onto the central object. Shear turbulence increases a disk's angular momentum flux to orders of magnitude above that which is possible with ordinary collisional viscosity. However, studies show that only for low-vorticity rotational profiles does laminar flow breakdown into turbulent flow (Lighthill 1978, Hawley et al 1999). More recently, an alternative mechanism for generating disk turbulence has come under scrutiny, based on the fact that astrophysical disks are generally magnetised. Even weak magnetic fields completely alter the stability behaviour of astrophysical gases, both rotationally and thermally (Balbus 2001). Weak fields depend on the hydrodynamic properties of the unperturbed disk. Given that the angular velocity decreases outward in a weakly magnetised accretion disk, the rotation profile is linearly unstable (Balbus & Hawley 1991). This instability is known as the magnetorotational instability. It is the only instability shown to be capable of producing and sustaining the enhanced stress needed for accretion to proceed on viable timescales. Furthermore, the level of the resulting turbulence can change rapidly, erupting or even turning off completely. All this occurs while the underlying Keplerian profile remains essentially fixed. Hence, the magnetorotational instability is now at the centre of numerical accretion disk studies. Unfortunately, the study of this 'MHD turbulence' in protostellar disks is complicated by the low ionisation fraction of the gas. This affects the coupling between the matter and the field and so making it imperative to account for a departure from ideal MHD conditions.

Angular momentum extraction via bipolar outflows has, in the past, generally been considered seperately to disk turbulence in analytic and numerical investigations. A combination of the two mechanisms as a means of angular momentum extraction is now also under consideration. Very recent studies (Salmerson & Königl 2005) have begun to investigate whether radial (magnetorotational instability induced) angular momentum transport can coexist with vertical transport (via outflows). If so, the relative importance of these two mechanisms at different locations and evolutionary stages in protoplanetary disks requires examination.

In order to gain an understanding of the possible extent of the bipolar jet's role in angular momentum extraction, the underlying MHD theory of the magneto-centrifugal mechanism for launching collimated outflows is now presented.

2.2.2 Magnetocentrifugal Mechanism of Jet Launching

Magneto-centrifugal models propose that magnetic fields in the collapsing, rotating cloud core are advected with the accretion flow and so form an hour glass shaped magnetic field as a result of this inward motion of the disk material. The accreting central protostar,

which becomes fully convective soon after its formation, supports a rigid, co-rotating (with the star), roughly bipolar stellar field which may extend to 5 to 10 stellar radii. The point where the outermost stellar field line intersects the accretion disk determines the rotation rate of the young star. This point will rotate with the Keplerian rotation speed of the disk at that radius, called the co-rotation radius. Inside this radius, the stellar magnetic field dominates all pressures and rotates as a rigid body anchored to the star. Matter is lifted from the disk, forced to move along magnetically dominated accretion columns to high stellar latitudes, where it is accreted onto the star. Most have adopted this magnetic geometry, first worked out by Ghosh & Lamb (1977; 1978). In the case of YSOs, there is direct observational evidence of this process, e.g. characteristic broad line profiles consistent with formation in the extended magnetospheric flow (Muzerolle et al. 1998a; 1998b; 2001) and the spectral energy distribution of the optical and ultraviolet excess consistent with accretion shock emission (Calvet & Gullbring 1998; Gullbring et al. 2000; Ardila et al. 2002).

However, models using this approach differ in their *source* of magnetic forces which drive the jet. Current research proposes two main alternatives: the interaction region between the protostar and disk, called the 'X wind' model (e.g. Wardle & Königl 1993; Lovelace et al. 1995; Ostriker & Shu 1995; Shu et al. 2000); and the disk alone, called the 'Disk wind' model (e.g. Blandford & Payne 1982; Pudritz & Norman 1983; Uchida & Shibata 1985; Königl & Pudritz 2000). Both models have been shown to plausibly produce the correct ejection-accretion ratios. In the 'X wind' scenario, the magnetic 'X-point' (where the stellar magnetosphere intersects the disk, which is truncated at the co-rotation radius) is the point of origin of a magneto-centrifugally driven wind fueled by matter injected onto open field lines and flung to infinity. In this picture, magnetic forces on the open field lines $\sim$0.03 AU from the central star are responsible for collimating the wind into a stellar jet. Conversely, the 'Disk wind' model proposes centrifugally driven winds launched from a magnetised disk surface, and so launching occurs not only close to the star but also up to a few AU along the disk from the source. Therefore, the basic assumption of this mechanism is the existence of a magnetic field threading the accretion disk of the protostar. (No direct observations have yet determined a typical magnetic field strength for accretion disks around low mass stars.) For disks *without* a hot corona ('cold' disks), as in the case of a protostar, it is possible for such jets to be launched without the contribution of thermal effects but through magnetic effects alone. This is possible *provided* the hour-glass shaped field lines are inclined at an angle of at least 30° with respect to the vertical axis (see Königl & Pudritz 2000).

A narrative description of the basic physics follows, before outlining the relevant equations (Section 2.2.3) in a form applicable to my results. Emphasis is on the 'Disk wind' model because my observational findings (Chapters 4 and 5) appear to be more readily explained using this scenario.

Consider a plasma, in a large scale magnetic field, of sufficient ionisation that the ions and neutrals are well coupled (through collisions) such that the plasma can be considered as a one-component fluid. In the infinite conductivity limit, assumed in many astrophysical applications, the electric field effectively disappears. With the electric field fixed at zero, then by the laws of induction the relative change between the magnetic field and fluid motion is limited, and so the field is said to be 'frozen in'.

In the case of cloud collapse, gravitational forces dominate over magnetic forces. The large scale magnetic field is 'dragged' inwards with the motion of the gas, and so takes on an hour-glass shape. As some of the gas particles in the disk experience increased heating and become ionised, they manage to escape from the disk's surface. A role reversal now occurs for these particles, whereby it is now the magnetic field which dominates over the inertial and pressure forces of the gas. The gas is accelerated upwards off the disk by centrifugal forces, and guided by the field lines. The angular velocity of the particles remains unchanged, so long as the ions are forced to move with the field. This means that, as the gas increases its distance from the disk surface, the angular momentum of the gas increases per unit mass. Conservation of angular momentum then implies that the disk must decrease its angular momentum correspondingly.

Soon, the accelerating outflow reaches the Alfvén velocity. At this distance from the star, the Alfvén radius (which defines the so called Alfvén surface), the kinetic energy density matches the magnetic energy density. Yet again a role reversal occurs whereby the magnetic field can no longer guide the plasma and so is forced to move with the gas once more. The gas now has enough energy to dominate over the field strength, since the magnetic pressure is negligible compared to the inertia and gas pressure, and so the 'frozen in' field is forced to curve in the direction of the gas rotation. The outflow now takes on a rotational velocity determined by the angular momentum of the disk where the ions originated and magnified on the journey to the Alfvén surface.

The magnetic field can be decomposed into poloidal and toroidal components. The curvature of the magnetic field means the toroidal component has now been substantially increased. The interaction of the toroidal field and the vertical component of the plasma motion then sets up a Lorentz force which is directed towards the rotation axis (i.e. the so called 'z-pinch' or 'hoop stress'), thus collimating the gas. The resulting hoop stress dominates over the defocussing forces (i.e. outward pressure gradients and centrifugal

forces), leading to a high degree of outflow collimation.

The net effect is that the outflow has set up a braking torque on the disk, whereby the initial path of the outflow particles acts as a 'magnetic lever arm'. In this way, angular momentum is extracted from the disk causing it to slow down. Matter can then move inwards on the disk towards the protostar to a point where the rotational velocity of the disk equals that of the protostar (i.e. at the co-rotation radius), and can then accrete onto the star.

2.2.3 Applied Theory

I present here the relevant theoretical equations, as described by Woitas et al. (2005), in a form applicable to my observational results of later chapters. Specifically, I use these equations to check whether my results are consistent with the 'Disk wind' model described by Königl & Pudritz (2000). As in many models, a steady-state, axisymmetric bipolar jet satisfying ideal MHD conditions is assumed, and described by cylindrical coordinates (r, z, ϕ) in which the star is at the origin. The velocity and magnetic field vectors comprise poloidal (r, z) and toroidal (ϕ) components.

Consider now the balance of angular momentum influx and efflux in a jet-disk system. The angular momentum flux available for extraction from the disk to allow accretion is given by $\dot{L}_{disk}$. The angular momentum flux that may be carried away by the bipolar jet is given by $\dot{L}_{jet,red}$ and $\dot{L}_{jet,blue}$, denoting receding and approaching jets respectively. The angular momentum that may be carried away by viscous forces within the disk is given by $\dot{L}_T$ (where $_T$ represents the turbulent stress tensor which is related to the turbulent viscosity). Equating these terms as dictated by the conservation of angular momentum flux in the system yields,

$$\dot{L}_{disk} = \dot{L}_T + \dot{L}_{jet,red} + \dot{L}_{jet,blue}. \tag{2.1}$$

In order to obtain an observational estimate of each quantity, consider the schematic of a jet-disk system shown in Figure 2.3. The schematic shows a series of nested magnetic surfaces (i.e. areas of constant magnetic flux) rooted in the disk along, which the gas particles are forced to flow. The point at which a magnetic surface intersects the Alfvén surface is denoted by the Alfvén radius, r_A. As will be seen, jet observations allow us to determine the point on the disk (i.e. $z = 0$) where the observed material originated. This launch point is denoted by a jet footpoint radius, $r_{0,obs}$. When calculating $r_{0,obs}$, it can be assumed that the jet observations are made at a distance above/below the disk plane of effectively $z = \pm\infty$. So the radius of the observations is denoted by $r_{\infty,obs}$. Lastly,

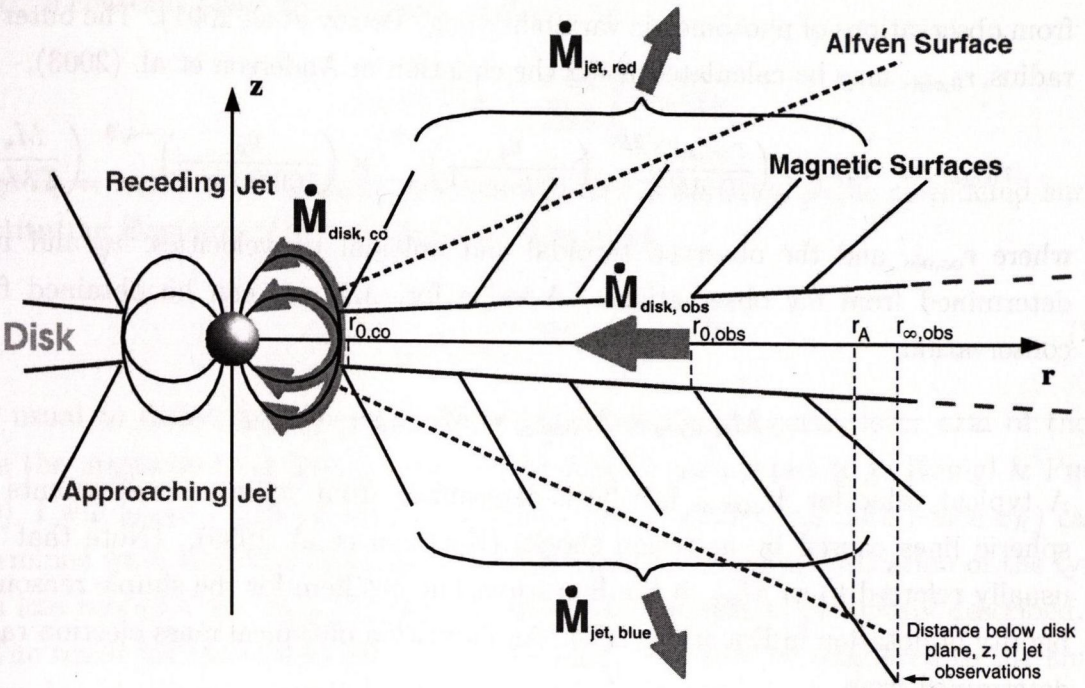

Figure 2.3: *Pictorial sketch (adapted from Woitas et al. 2005, and not to scale) of magnetic surfaces rooted in the accretion disk, according to the 'Disk wind' scenario .*

the disk is truncated at an inner radius where it co-rotates with the star, $r_{0,co}$, and where magnetospheric accretion occurs.

Consider a volume of this jet-disk system, bounded by inner and outer magnetic surfaces which are rooted in the disk at $r_{0,co}$ and $r_{0,obs}$, and by surfaces above and below the disk at the distance of the observations. (The assumption of $z = \pm\infty$ for the observation distance is made only when calculating $r_{0,obs}$.) Then, the angular momentum available in this volume for extraction from the disk to allow accretion is given by,

$$-\dot{L}_{disk} = \dot{M}_{disk,co}\, r_{0,co}\, v_{K,co} - \dot{M}_{disk,obs}\, r_{0,obs}\, v_{K,obs} \tag{2.2}$$

where $\dot{M}_{disk,co}$ and $\dot{M}_{disk,obs}$ are the mass accretion rates, while $v_{K,co}$ and $v_{K,obs}$ are the Keplerian rotational velocities of the disk, at $r_{0,co}$ and $r_{0,obs}$ respectively. Once the footpoint radii are known, the Keplerian rotational velocities can be calculated from

$$v_K = \sqrt{GM_\star / r_0} \tag{2.3}$$

where G is the universal gravitational constant and $M_\star$ is the stellar mass which can be found in the literature. The co-rotation radius, $r_{0,co}$, can be calculated from the stellar period, $2\pi/\omega$, since accretion occurs when the disk's angular velocity falls below the Keplerian velocity, i.e. $\omega r_{0,co} < \sqrt{GM_\star / r_{0,co}}$. The stellar period, in turn, can be determined

from observations of photometric variability (e.g. Petrov et al. 2001). The outer footpoint radius, $r_{0,obs}$, may be calculated using the equation in Anderson et al. (2003),

$$r_{0,obs} \approx 0.7\,AU \left(\frac{r_{\infty,obs}}{10\,AU}\right)^{2/3} \left(\frac{v_\phi}{10\,kms^{-1}}\right)^{2/3} \times \left(\frac{v_p}{100\,kms^{-1}}\right)^{-4/3} \left(\frac{M_\star}{1\,M_\odot}\right)^{1/3} \quad (2.4)$$

where $r_{\infty,obs}$ and the observed toroidal and poloidal jet velocities, v_ϕ and v_p, can be determined from my observations. A value for, $\dot{M}_{disk,obs}$ can be obtained from mass conservation,

$$\dot{M}_{disk,obs} - \dot{M}_{disk,co} = \dot{M}_{jet,red} + \dot{M}_{jet,blue} \quad (2.5)$$

A typical value for $\dot{M}_{disk,co}$ has been determined from veiling measurements of photospheric lines caused by accretion shocks (Hartigan et al. 1995). (Note that $\dot{M}_{disk,co}$ is usually referred to as $\dot{M}_{acc}$ in the literature, but not here for the simple reason of unambiguity of notation in Equation (2.2)). An indication of typical mass ejection rates can be determined from

$$\dot{M}_{jet} = \int \rho \mathbf{v_p} dA \quad (2.6)$$

where the area, A, is obtained assuming the jet diameter is equivalent to the spatial full width half maximum (FWMH) of a given emission line, and the hydrogen density, ρ, is obtained from the electron density, n_e, and ionisation fraction, x_e, since the number density of hydrogen is given by $n_H = n_e/x_e$. A value for n_e and x_e can be found from my results (see Chapter 4, Section 4.4.8). Finally, substituting all of the above into Equation (2.2), allows a value for $\dot{L}_{disk}$ to be found.

Next, we want to find the contribution of the bipolar jet to the extraction of angular momentum from the system, $(\dot{L}_{jet,red}+\dot{L}_{jet,blue})$. Consider the angular momentum balance written in conservative form (Casse & Ferreira 2000),

$$\nabla \left(\rho r v_\phi \mathbf{v_p} - \frac{r B_\phi}{4\pi} \mathbf{B_p} - r \mathbf{T_v}\right) = 0 \quad (2.7)$$

Due to axisymmetry, the induction equation $\nabla \times (\mathbf{v} \times \mathbf{B}) = 0$ forces $\mathbf{v_p} \parallel \mathbf{B_p}$, implying there is a function k, the mass load of the jet, such that $\rho \mathbf{v}_\mathrm{p} = k \mathbf{B}_\mathrm{p}$ (see Königl & Pudritz 2000). Then for each jet lobe the angular momentum extracted is given by

$$\dot{L}_{jet} = \int_S \left(r v_\phi - \frac{r B_\phi}{4\pi k}\right) \rho \mathbf{v_p} \cdot \mathbf{n} dS \quad (2.8)$$

MHD wind theory prescribes that the quantity in parentheses, which represents the total (kinetic plus magnetic) specific angular momentum (i.e. angular momentum per unit

mass), is constant along the magnetic surfaces, i.e.

$$l_{\rm jet} = \left(r v_\phi - \frac{r B_\phi}{4\pi k} \right) = r_A^2 \Omega_0 \tag{2.9}$$

where $\Omega_0 = v_K / r_0$ is the angular speed of the disk at the base of the considered surface. Substituting Equation (2.9) into Equation (2.8) gives

$$\dot{L}_{jet} = \int_S \left(\frac{r_A}{r_0} \right)^2 r_0 v_K \rho \mathbf{v_p} \cdot \mathbf{n} dS \tag{2.10}$$

It is usual to define $\lambda = (r_A/r_0)^2$ where (r_A/r_0) is the magnetic lever arm of the jet. Since the magnetic lever arm $(r_A/r_0) \sim 3$ for typical parameters (e.g. Königl & Pudritz 2000), I will adopt λ=10 for my calculations. The footpoint, r_0, (and hence v_K) can be determined from Equation (2.4), as previously described, and an indication of the typical mass loss rate of a jet, $\dot{M}_{jet} = \int \rho \mathbf{v_p} \, dA$, can be determined as previously described.

The result for the bipolar jet, $\dot{L}_{jet,red} + \dot{L}_{jet,blue}$, can now be compared to the amount of angular momentum that must be taken from the disk to allow accretion, $\dot{L}_{disk}$, and hence the contribution of the outflow to angular momentum extraction can be observationally determined. Lastly, the possible contribution of $\dot{L}_T$ can be estimated. See Woitas et al. (2005) for further elaboration.

3

Time Evolution of a YSO Outflow

This chapter examines YSO jet propagation through a case study of the XZ Tauri pre-main sequence system, using *HST* imaging observations at optical wavelengths.

3.1 Introduction

XZ Tau is a classical T Tauri binary system with a separation of 0.″3 (Haas et al. 1990) and is located in the well known Lynds 1551 star-forming region some 140 pc away (Elias et al. 1978). The system was first found to have an associated HH outflow through ground-based CCD imaging and spectroscopy (Mundt et al. 1988, Mundt et al. 1990). XZ Tauri is unusual in that *both* the source and outflow remnants are optically visible, whereas most visible outflows are from embedded stars, making it important for optical studies. These early observations revealed a bipolar optical flow that could be traced to at least 10″ on either side of the binary at a position angle of 15 °, Figure 3.1. The first *HST*/WFPC2 images of XZ Tauri taken in 1995 show a bubble of emission nebulosity extending 4″ to the north of the system (Krist et al. 1997, hereafter K97). Further images, taken 3 years later, show dramatic structural changes as the bubble expanded and altered from being centre-brightened to limb-brightened, suggesting the formation of a HH bowshock (Krist et al. 1999, hereafter K99).

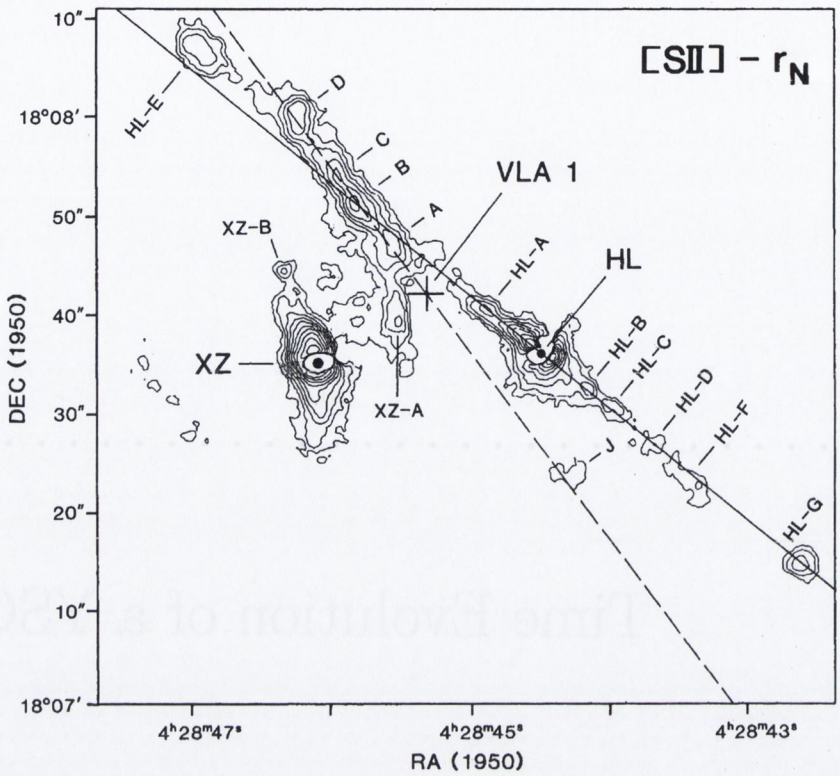

Figure 3.1: *Contour plot of the HL/XZ Tau region (Mundt et al. 1990) showing the full extension of the XZ Tauri outflow. Close-up images of XZ Tau, Figure 3.2, reveal a 'bubble' which extends towards XZ Tau B of this figure.*

Ground-based photometry of XZ Tau from 1962 to 1981 (Herbst et al. 1994) has shown variations, of almost two magnitudes in the V-band, for the binary as a whole. Such variations are common among YSOs. Of the two components, the southern one has been, at least until recently, optically brighter and thought to be the more evolved star. Its companion, however, dominates at infra-red wavelengths and is probably of higher overall luminosity (Haas et al. 1990). Recent Faint Object Spectrograph (FOS) observations unexpectedly found the northern component to be optically brighter (White et al. 2001, hereafter WG01), a result that I will discuss further in the light of my findings. For this system therefore it seems more appropriate not to use the terms primary and secondary but instead to adopt the nomenclature, used in K97, of XZ Tau North and South.

In this chapter, I present an analysis of further (unpublished) *HST* archival WFPC2 images of the XZ Tau system and outflow from 1999, 2000 and 2001. These data show not only ongoing changes in the outflow but a dramatic brightening of XZ Tau North in the optical suggesting that it may be an EXor. In collarboration with Dr T. Downes (Dublin

City University), I also present a simulation of the outflow in an attempt to reproduce its dynamical and morphological evolution.

3.2 Data

High resolution archival WFPC2 images of XZ Tauri were obtained for 3 consecutive epochs: 1999 February 3; 2000 February 6; and 2001 February 10. The binary was at the same approximate location on the Planetary Camera (spatial sampling = $0\farcs04555\,\mathrm{pixel}^{-1}$) for all frames. Four filters were used: Hα (F656N); [S II] (F673N); R-band (F675W) and I-band (F814W). The frequency and duration of the short exposures for each filter were: 1×120 s; 1×180 s; 2×6 s; and 2×6 s respectively. Two long exposures for each filter of 1000 s were also extracted from the *HST* Archive, all of which were saturated at the location of XZ Tauri. No short exposures were made for the I-band filter in the final year.

Previously published WFPC2 archival data for XZ Tauri (K99) facilitated proper motion measurements. These data comprised images from 1995 January 5 and 1998 March 25. The 1995 images used were 2×600 s exposures in the R-band and 1×3 s exposure in the I-band. The latter allowed me to determine the stellar positions, as no R-band short exposures were taken and the long exposures were saturated in the vicinity of the star. The 1998 images were taken in the R-band only: 2×6 s and 2×1100 s exposures. All frames were processed through the standard *HST* pipeline and each set of double exposures was combined to eliminate cosmic rays.

The accumulated data yielded high resolution images of XZ Tau spanning a total of 6 years. I analyse these data in Section 3.3, under the two headings: outflow structure, proper motions and [S II] luminosity; and stellar astrometry and photometry.

3.3 Results

3.3.1 Outflow Structure, Proper Motions & [S II] Luminosity

The Planetary Camera images for each year were aligned and their orientation corrected where necessary. A montage of R-band images, covering the full timespan, is shown in Figure 3.2. As previously observed (K99), there appears to be two edge-brightened 'bubbles', i.e. inner and outer shocks, similar to those seen with *HST* close to DG Tau (Bacciotti et al. 2000). By 2001, the rapidly fading outer shock reached a distance of approximately 800 AU from the binary, while the inner shock has travelled approximately half as far.

Observation date/interval	Distance from source (AU)	Bubble width (AU)	Longitudinal speed ($km\,s^{-1}$)	Transverse speed ($km\,s^{-1}$)
1995 Jan 5	598 ±16	336 ±25	-	-
1995 Jan 5 to 1998 Mar 25	697 ±10	405 ±14	146 ±28	101 ±42
1998 Mar 25 to 1999 Feb 3	721 ±9	423 ±5	130 ±73	105 ±83
1999 Feb 3 to 2000 Feb 6	746 ±11	-	119 ±65	-
2000 Feb 6 to 2001 Feb 10	771 ±10	-	117 ±69	-
1998 Mar 25 to 2001 Feb 10	-	-	130 ±84 (jet)	-

Table 3.1: *Projected sizes and speeds of the XZ Tauri outer bowshock (and an average speed for the brightest jet knot) as it evolves. Distances and widths are quoted for the second date of the observation interval. Errors are 3σ.*

Although remarkably bright in 1995, the knots in the XZ Tau jet appear very faint by 2001. The jet's position angle (PA) is around 15° in line with the major axis of the elongated outer bubble and its known extended optical outflow. The knots, however, are not in a perfectly straight line. Some deviation is evident and reminiscent of similar behaviour seen in flows like the HH 34 jet close to its source (Reipurth et al. 2002).

Significant proper motions were observed as the bubble expanded away from XZ Tau. Tangential velocities for the central jet knot and outer shock (see for example the bottom right 'difference' frame in Figure 3.2) were obtained from the long F675W exposures. The latter were used since they include the main HH emission lines, i.e. [O I]$\lambda\lambda$6300,6363, Hα and [S II]$\lambda\lambda$6717,6731. The distance to the binary was assumed to be 140 pc as in K99. In Table 3.1, I list the derived tangential velocities as a function of epoch for the outer shock and an average velocity for the jet. Longitudinal sizes and speeds were calculated along the jet axis (PA ~15°). Transverse sizes and speeds were calculated perpendicular to the jet axis at the bubble's widest zone. As the shock expands it grows fainter and so its width is not given for later observations. The central knot also grows very faint, especially at later epochs, so I prefer to quote an average for the jet speed. Finally, although the inner shock or bubble was seen to expand, changes from year to year proved difficult to trace and so no tangential velocity is given here.

From Table 3.1, a deceleration of the outer shock is clear. Although the errors appear large, examination of the 1998-2001 interval yields a longitudinal speed of $121 \pm 24\,km\,s^{-1}$ (cf. $146 \pm 28\,km\,s^{-1}$ from 1995 to 1998) indicating that the shock front is indeed decelerating. Simulations were carried out in order to model the observations using plausible jet and ambient medium parameters (see §3.3 below). Observed speeds are as expected in order to maintain the observed low aspect ratio of the bubble (i.e. the length to width ratio is numerically greater than one, but is still lower, relatively speaking, than that of

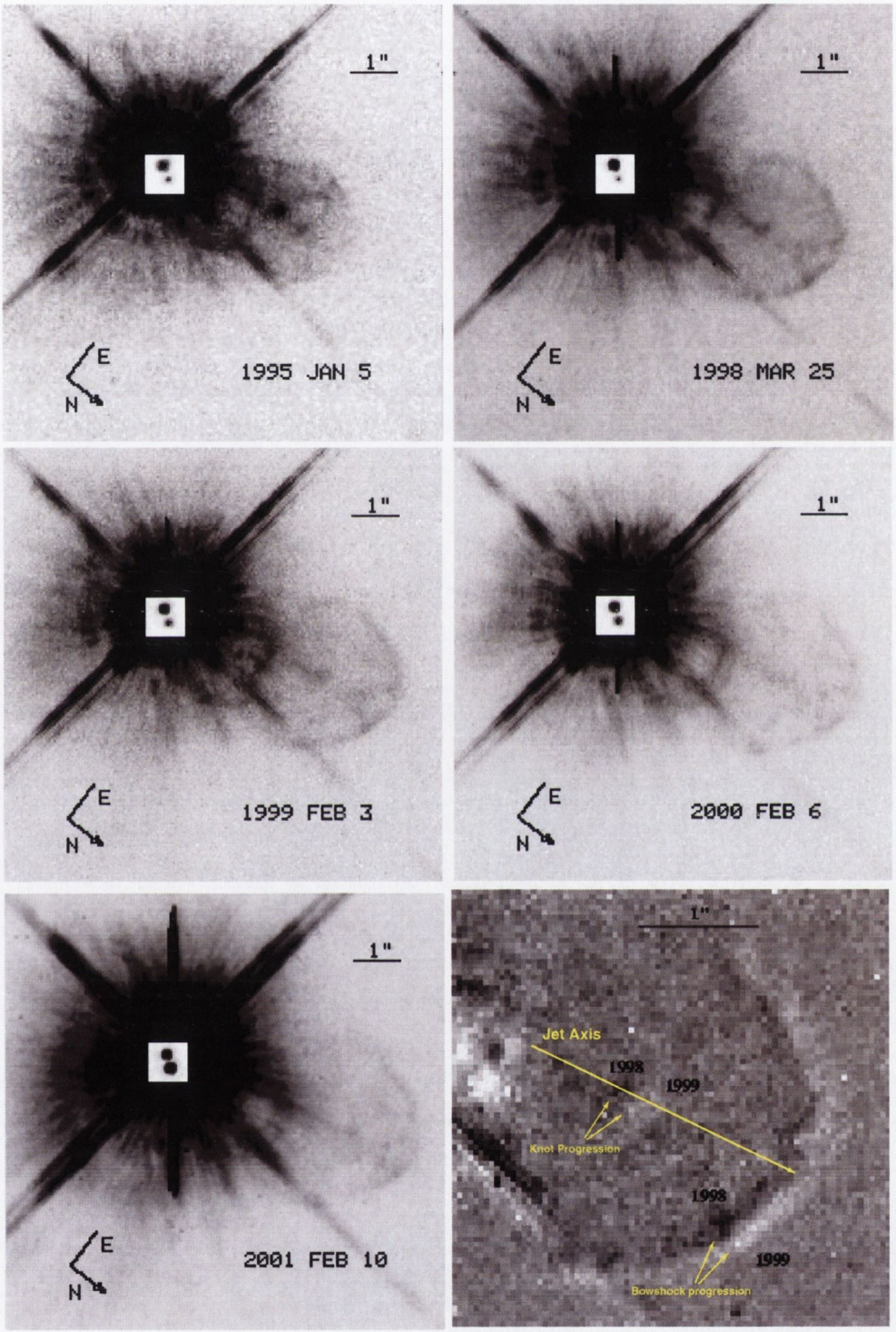

Figure 3.2: *HST/WFPC2 F675W (R-band) images of XZ Tau and its outflow on: 1995 Jan 5; 1998 Mar 25; 1999 Feb 3; 2000 Feb 6; and 2001 Feb 10. The short exposure image of the binary is superimposed on the long exposure image in each case. The bottom right frame is an R-band difference image 1999-1998 showing proper motion in the jet and the outer shock.*

Date of Observation	Separation (arcsec)	Position Angle (degrees)
1995 Jan 5	0.302	146.35 ±0.38
1998 Mar 25	0.299	145.50 ±0.25
1999 Feb 3	0.303	144.85 ±0.26
2000 Feb 6	0.300	143.30 ±0.25
2001 Feb 10	0.298	142.38 ±0.24

Table 3.2: *Separation and position angle of the XZ Tau binary. Errors in separation angles are estimated to be* ±0.″005.

many YSO outflows which have a much narrower shape), and are in the same region as those given by the simulation, (see Table 3.4 below). As a further check the simulated and observed [S II]λλ6317,6731 luminosities were compared. The latter was found from the 2001 F631N filter images for the outer shock only, i.e. excluding the inner shock region which is contaminated with diffraction spikes and nebulosity near the star. First, I obtained an average number of the counts per pixel for the background, and then for the outer shock region (excluding the jet knot emission and any defective pixels). A background subtracted total number of counts was then calculated for the area of the outer shock. The appropriate flux per count was obtained from the values given in the WFPC Instrument Handbook for this filter's wavelength region. The apparent luminosity was then determined, from the total flux at a distance of 140 pc, to be $2.5\,(\pm 3.6) \times 10^{28}\,\mathrm{erg\,s^{-1}}$. Assuming a total optical extinction of $A_v \sim 1.39$ towards the bubble, i.e. the same as towards the binary (WG01), the intrinsic luminosity increases to $\sim 4.3 \times 10^{28}\,\mathrm{erg\,s^{-1}}$. This, of course, is probably an overestimate since the source is likely to be more embedded than the outflow.

3.3.2 Stellar Astrometry & Photometry

Using the short R-band exposures, the separation and position angle of the binary were determined for each epoch and are listed in Table 3.2. Within errors, no changes were detected in the separation of the XZ Tau binary. The difference between the first and final observations reveals an average decrease of $0.75\,^\circ\,\mathrm{yr^{-1}}$ in the binary position angle, a value somewhat higher than derived by K99 based on earlier *HST* data (of $0.5\,^\circ\,\mathrm{yr^{-1}}$) but at the same time lower than that found by Woitas et al. (2001) using speckle interferometry (of $\sim 1.3\,^\circ\,\mathrm{yr^{-1}}$). Following K99, assuming a face-on orbit, the total mass for the binary is about $0.3\,M_\odot$. Although such a value is clearly too low, note that the combined mass is very sensitive to the projection angle. Such a figure is certainly below the estimates of Hartigan et al. (2003) and WG01 who suggested a combined mass closer to $1\,M_\odot$.

Broadband R and I magnitudes were calculated for the binary, using the method outlined in the WFPC2 Data Reduction Handbook and interpolated Johnson offsets appropriate for the spectral types of XZ Tau North and South, i.e. M2 and M3.5 respectively (Hartigan & Kenyon 2003). My results are presented in Table 3.3 and the R-band WFPC2 data were used to plot a light curve for each component, Figure 3.3. Over the six years of observations, XZ Tau South varies by at most 0.3 magnitudes (in R-band) and has a mean R magnitude of around 13.5. In contrast, XZ Tau North shows an initial reduction in brightness of about a magnitude in R until 1998 and thereafter its brightness increases dramatically by around 3 magnitudes. This flaring behaviour means that by 2001 XZ Tau North was actually the brighter star. Similar variations are seen in the I-band although the data are somewhat more sparse.

The dramatic brightening of XZ Tau North suggests it is an EXor. EXors, named after their prototype EX Lupi, are extreme classical T Tauri stars that periodically undergo outbursts from the ultraviolet to the optical. Although increases by several magnitudes with rise times of up to a few years have been recorded (Herbig 1989), the changes in these YSOs are not as extreme as in FU Orionis stars. EXor spectra, for example, even in outburst continue to resemble those of T Tauri stars. The phenomenon is thought to be due to major increases in the underlying disk accretion rate, but the number of known EXors is relatively few. The proposition that XZ Tau North is such a YSO is further strengthened by the *HST* spectroscopic data of Hartigan et al. (2003). As with other EXors, the spectrum shows not only very strong Balmer lines but also strong Ca II and moderate Na I in emission (see, for example, Parsamian et al. 2002). Such strong spectral emission lines coupled with high variability makes XZ Tau North the most likely source of the outflow. Finally, WFPC2 images taken in March 1997, as part of *HST* GO Programme 6735, show XZ Tauri North comparable in brightness with XZ Tauri South at short optical wavelengths, i.e. both having magnitude 16.9 in U-band (WG01). This suggests that EXor behaviour *may be visible at the shortest wavelengths first* or that, before the outburst, both stars were comparable in U-band magnitude but the southern component has always been redder. Either way, the comparable U-band magnitude of the components would explain why the 1996 *HST*/FOS acquisition of XZ Tauri taken at a central wavelength of 3600 Å (Proposal ID 6014) unexpectedly locked onto the wrong (northern) star (WG01).

3.3.3 Outflow Simulations

Numerical simulations of the XZ Tauri outflow were conducted to check the physical interpretation of the observations. The code used is that described in Downes & Ray (1999). It

Filter	Observation Date	Flux Ratio South/North	XZ South Magnitude	XZ North Magnitude
R-band	1995 Jan 5	5.11	13.16	14.93
	1997 Mar 8	5.39	13.47	15.38
	1998 Mar 25	9.02	13.22	15.68
	1999 Feb 3	3.66	13.45	14.93
	2000 Feb 6	2.43	13.32	14.36
	2001 Feb 10	0.63	13.25	12.82
I-band	1995 Jan 5	4.80	12.03	13.78
	1997 Mar 8	6.30	11.97	14.02
	1999 Feb 3	3.38	12.04	13.42
	2000 Feb 6	1.98	12.02	12.82

Table 3.3: *Johnson apparent magnitudes of the XZ Tauri binary. Errors in magnitude of ±0.05 were estimated based on the affect of changing aperture size, given that the stellar PSFs are overlapping. The 1995 Jan 5 R-band data is from K97 using Tiny Tim PSF fitting to the saturated R-band images. The 1997 Mar 8 data is from HST GO Programme 6735.*

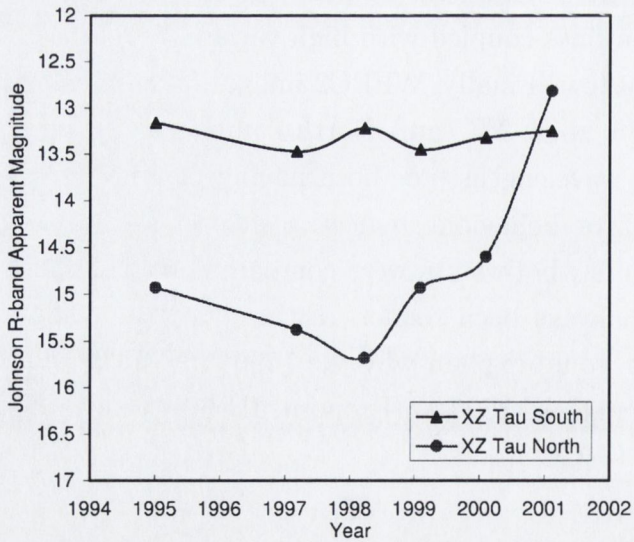

Figure 3.3: *Stellar Johnson R-band apparent magnitudes of the XZ Tauri binary.*

is a properly upwinded second order (in time and space), cylindrically symmetric code for solving the inviscid Euler equations. In addition to tracking the hydrodynamic variables (density, velocity and pressure), the code also tracks the ionisation state of hydrogen, without the assumption of ionisation equilibrium. It also has the capacity to track the number density of H_2, but this number density was set to zero for these simulations.

3.3.3.1 Initial conditions

The gas is taken to be one of solar abundances. The initial ambient density is assumed to be $100\,\mathrm{cm}^{-3}$ close to the source, rising to a value of $600\,\mathrm{cm}^{-3}$ at a distance of 1.25×10^{16} cm (835 AU) from the source, (see below for a discussion of why this behaviour is assumed). The ambient pressure was taken to be uniform, giving a temperature of 10^3 K close to the source, and dropping to approximately 160 K at the rise in ambient density. The resolution was set to 1×10^{13} cm in both the radial and poloidal (outflow) directions (r and z respectively), and the total grid size was 450×1500 cells. To estimate the mass flux in the outflow, it is assumed that approximately 2% of the accreted mass ultimately ends up in the outflow (Hartigan et al. 1995). A mass accretion rate for XZ Tau North of $1 \times 10^{-7}\,M_\odot\,\mathrm{yr}^{-1}$ was used (Hartigan & Kenyon 2003) based on recent photospheric line veiling measurements.

Assuming no change in jet radius, which is taken as $r_{\mathrm{jet}} \sim 2 \times 10^{14}$ cm (0.″1) based on the observed knots, the inferred mass flux implies a large jet density (i.e. much higher than the ambient density). But, since the jet is assumed to be highly supersonic with respect to the sound speed in the ambient medium in order to produce a shock front, the jet would then plough through the ambient medium creating a very narrow bowshock - contrary to the low aspect ratio observed.

One way of explaining the observations is to invoke a moderately collimated wind. A wind with a moderate opening angle will have a density which decreases significantly with distance from the source, and will also have a larger radius with distance. These effects each lead to a broader bowshock, in line with the observed morphology of the system. In addition, if the flow is not in the plane of the sky, the bowshock will appear to have a lower aspect ratio due to projection effects. An angle of 30 ° between the plane of the sky and the axis of the outflow is assumed, given the jet radial velocity of $80\,\mathrm{km\,s}^{-1}$ at 5.″0 (Mundt et al. 1990) and its proper motion of $145\,\mathrm{km\,s}^{-1}$ at 700 AU (Table 3.1).

With these considerations in mind, the full opening angle of the wind was set to 22 ° with an initial diameter (i.e. FWHM in density) of 4×10^{14} cm, or 40 grid cells. The wind density was given a linear profile across the outflow axis, with a density range from $\sim 1800\,\mathrm{cm}^{-3}$ along the jet axis to $\sim 100\,\mathrm{cm}^{-3}$ at the edge, and was chosen so that the total

Simulation age /age interval (years)	Corresponding observation date/interval	Distance from source (AU)	Bubble width (AU)	Longitudinal speed ($km\,s^{-1}$)	Transverse speed ($km\,s^{-1}$)
15	1995 Jan 5	590	288	-	-
15 - 18	1995 Jan 5 to 1998 Mar 25	695	360	164	67
18 - 19	1998 Mar 25 to 1999 Feb 3	722	386	148	63
19 - 20	1999 Feb 3 to 2000 Feb 6	749	402	129	51
20 - 21	2000 Feb 6 to 2001 Feb 10	775	420	115	44

Table 3.4: *Projected sizes and speeds of the simulated XZ Tauri outer bowshock as it evolves. Distances are quoted for the latter year of the age interval. There is a minimum error of* $\pm 6\,km\,s^{-1}$ *in the simulation speeds.*

mass flux was $2 \times 10^{-9}\,M_{\odot}\,yr^{-1}$. Hence it is assumed that the jet (traced by the knots) does not dominate the dynamics of the system.

The observed longitudinal speed of the jet averages at $130\,km\,s^{-1}$, but since it must be travelling faster than the shock front the actual value is more realistically in the range of 130–$200\,km\,s^{-1}$. Choosing a constant jet velocity of $250\,km\,s^{-1}$ will give a longitudinal velocity for the jet fluid of roughly $216\,km\,s^{-1}$. Since the bowshock appears to be decelerating significantly (see Table 3.1), some way to slow it down is needed. Turning off the jet will not, on its own, give the observed deceleration since the momentum density of the material in the cooled shell between the bowshock and jetshock is very large. It was found that the most effective way of decelerating the bowshock was to impose a significant increase in the ambient density. A six-fold increase, by the time the simulated shock reached 835 AU, was found to roughly reproduce the observed velocities.

3.3.3.2 Simulation results

Figure 3.4 contains a greyscale plot of the distribution of density at $t = 21$ yrs, the time at which the simulation roughly matches the 2001 observations. It can be seen that the bowshock has begun to encounter the rise in the ambient density (see Section 3.3.3.1), leading to a marked decrease in its speed of advance as can be seen from Table 3.4. Comparing this to Table 3.1 shows that the simulated behaviour of the outer shock velocity matches the observed reasonably well. The non-zero opening angle of the jet is also clearly noticeable, along with a number of bowshock irregularities which probably arise from the Vishniac instability, although they could also arise from Rayleigh-Taylor instability (since the bowshock is decelerating implying that the density of the bowshock is increased compared to the less dense ambient medium).

Figure 3.5 is a simulated [S II] image calculated for the density distribution shown in Figure 3.4, assuming an angle to the plane of the sky of $30\,°$. In calculating this, it is

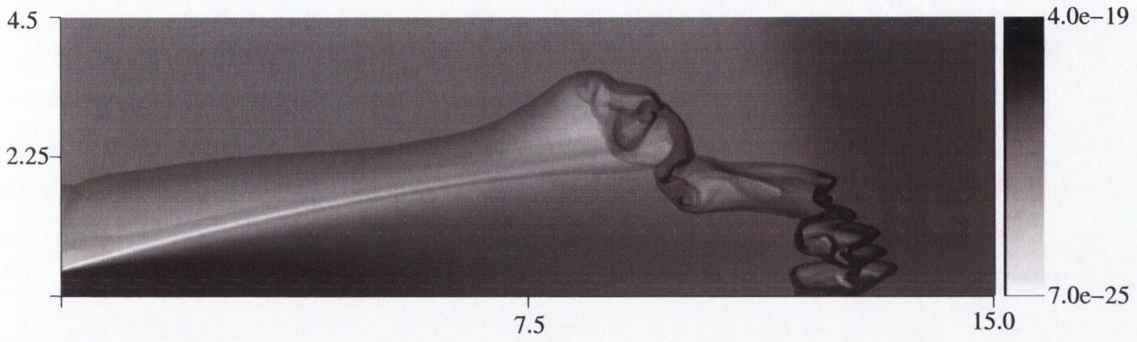

Figure 3.4: *Log-scale plot of the distribution of density at $t = 21\,yrs$. The distance scales are in units of $10^{15}\,cm$ ($15.0\times10^{15}\,cm = 1\,000\,AU$) and the intensity scale is in units of $g\,cm^{-3}$*

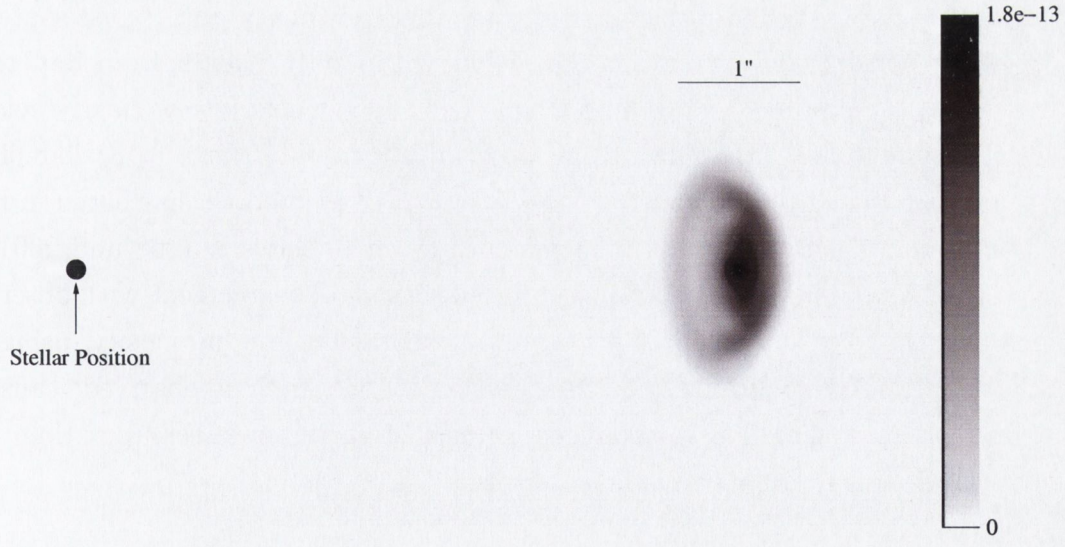

Figure 3.5: *Simulated [S II] image projected onto the sky (assuming an inclination with respect to the plane of the sky of 30°) at $t = 21\,yrs$ (see text). The intensity scale is in flux units of $erg\,cm^{-2}\,s^{-1}$.*

assumed that the fractional ionisation of sulphur can be described by coronal ionisation equilibrium (Arnaud et al. 1985) and that the line emission is not in local thermal equilibrium. The emission is plotted on a linear scale (similar to that in Figure 3.2). It has been projected onto the sky and convolved with a Gaussian of FWHM = 0.″1.

It can be seen that there is reasonable agreement between the observations and the simulation, certainly in terms of the morphology close to the head of the bowshock. The ring-like features arise from the assumption of cylindrical symmetry in the simulation. The emission would, in fact, be expected to be a little more 'clumpy' rather than ring-like.

Finally, the total [S II] luminosity calculated from the simulation is $1.1 \times 10^{29}\,\mathrm{erg\,s^{-1}}$. This is in good agreement with that observed (i.e. $4.3\ (\pm 3.6) \times 10^{28}\,\mathrm{erg\,s^{-1}}$ which, I remarked, is probably an overestimate, see Section 3.3.1). Note however that the bowshock apex appears much brighter with respect to the wings than is actually observed. This is most likely due to the use of cylindrical symmetry which results in a focussing of shocked material onto the axis in a way which would be very unlikely to happen in three dimensions.

3.4 Conclusions

Multi-epoch *HST*/WFPC observations of the XZ Tau binary and its associated outflow have shown considerable changes in the system within only 6 years, from 1995 to 2001. In the outflow, the presence of *two* limb-brightened shock fronts is now clearly evident, with a deceleration of the outer shock from $\sim 145\,\mathrm{km\,s^{-1}}$ to $\sim 115\,\mathrm{km\,s^{-1}}$. Stellar photometry revealed that the suspected source of the outflow, XZ Tau North, has flared in EXor-type fashion increasing in brightness by 3 magnitudes in R between 1998 and 2001. Finally, numerical simulations of the outflow produced reasonable agreement with observations in terms of morphology, dynamical evolution and emission line luminosity, using plausible ambient and outflow parameters. Deceleration by the amount observed, caused by the ambient medium, should have produced a much brighter bowshock apex than that seen. The cause of this discrepancy is not obvious.

4

YSO Jet Rotation at Optical Wavelengths

This chapter examines YSO jet generation through a survey of pre-main sequence jets, using *HST* spectroscopic observations at optical wavelengths.

4.1 Introduction

A key question in star formation research concerns the mechanisms behind the launch of jets from young stars. As described in detail in Chapter 2, these jets are believed to play an important role in the removal of excess angular momentum from the system, thus allowing accretion of matter onto the star up to its final mass. To briefly recap, it is generally acknowledged that magneto-centrifugal forces are responsible for jet launching. In particular in the so-called 'Disk wind' model, e.g. Ferreira (1997); Königl et al. (2000), the jet is launched from the disk surface within a few AU from the star; while in the 'X wind' model, i.e. Shu et al. (2000), the base of the flow is located at a few stellar radii from the source. To date, resolution constraints on observations have impeded progress in validating the magneto-centrifugal mechanism, since jet launching occurs on small scales (i.e. less than 20 AU from the star); moreover, infall and outflow kinematics are complex and confused close to the source, which is often heavily embedded. Recently, however, interesting results have been obtained from observations of jets from more evolved, less

embedded YSOs (i.e. classical T Tauri stars) for which the jet can be optically traced back to its origin.

Observational backing for canonical models would require, for example, proof of rotation around the symmetry axis, close to the base where the jet is launched. The first hint of jet rotation was reported for the HH212 system (Davis et al. 2000). However the knots were located at 2×10^3 - 10^4 AU from the jet source. This distance is too far for jet launch studies as material will have interacted with the local environment causing the jet kinematics to be disturbed. Independently, asymmetries in velocities within the first 110 AU of the outflow from the T Tauri star DG Tau were found (Bacciotti et al. 2002), indicative of rotation. These results were obtained through an analysis of high angular resolution spectra taken with the *HST* Space Telescope Imaging Spectrograph (*HST*/STIS), aimed at probing the acceleration and collimation region of a YSO jet. Further confirmation of the rotation hypothesis came from Owens Valley Radio Observatory (OVRO) observations, which report the sense of rotation of the disk of DG Tau to be the same as that of the jet (Testi et al. 2002). Moreover, the derived toroidal velocities in the observed portion of the jet were seen to be in agreement with the predictions of the magneto-centrifugal models, and indeed they can be used to find the location on the disk plane of the launching point of the wind, (Bacciotti et al. 2002; Anderson et al. 2003; Dougados et al. 2004; Pesenti et al. 2004).

These results provided the motivation to conduct a survey to establish conclusively whether jets from young stars rotate. A series of observations were conducted with *HST*/STIS of six T Tauri stars (i.e. YSOs which have evolved to a point where their jets have become visible in the optical region of the spectrum) in order to examine their jets close to the source and hence determine if there is any sign of rotation before the jet has interacted with the environment. I present here a radial velocity analysis of eight jet targets, each from one of six T Tauri stars listed in Table 4.1, i.e. the bi-polar jets from TH 28 and RW Aur, and the approaching jet from LkHα 321, DG Tau, CW Tau and HH 30.

4.2 Observations

Spectroscopic observations, in the optical wavelength region, were made at the base of eight jets, each from one of six T Tauri stars (listed in Table 4.1). An acquisition of the stellar peak intensity prior to science observations allowed the slit to be centred accurately on the star before being offset to a position perpendicular to the jet axis at a fraction of an arcsecond from the source, Figure 4.1.

Target	Location	Distance (pc)	$M_\star$ ($M_\odot$)	v_{hel} (km s^{-1})	i_{jet} (deg)	References
TH 28	Lupus 3	170	...	+5	10	1, 2
RW Aur	Auriga	140	1	+23	44	3, 4
LkHα 321	Cygnus	550	...	-7	...	5, 6
DG Tau	Taurus	140	0.67	+16.5	52	7
CW Tau	Taurus	140	1.4	+14.5	41	8, 9, 10
HH 30	Taurus	140	0.67	+17	1	11, 12

Table 4.1: *Details of T Tauri star jet targets in this survey. All radial velocity results, v_{rad}, in subsequent sections are quoted having corrected for the heliocentric velocity of the system, v_{hel}, unless otherwise stated. The inclination angle of the jet, i_{jet}, is given with respect to the plane of the sky. The value of i_{jet} for LkHα 321 is assumed to be 45° (arbitrary, since unknown, although spectroastrometric measurements suggest an even larger value (Whelan et al. 2003). References: 1 - Graham et al. (1988); 2 - Krautter (1986); 3 - Woitas et al. (2001, 2002); 4 - Martin et al. (2003); 5 - Mundt et al. (1998); 6 - E. Whelan (2003), private communication; 7 - Bacciotti et al. (2002); 8 - Gomez de Castro (1993); 9 - Hartmann et al. (1986); 10 - Hartigan et al. (2004) 11 - Pety et al. (2002); 12 - Mundt et al. (1990).*

HST/STIS optical observations were conducted of each lobe of the bipolar jet from the classical T Tauri stars TH 28 and RW Aur, and of the approaching jets from T Tauri stars LkHα 321, DG Tau, CW Tau and HH 30 (proposal ID 9435). A slit offset of 0.″3 was used in all cases, except for the approaching jet of RW Aur and CW Tau where 0.″2 was used (due to lack of line emission at 0.″3 (Woitas et al. 2002), and HH 30 where 0.″6 was used (due to obscuration of the star and base of the jet by the disk). This slit offset represented a de-projected distance along each jet of: 52 AU for TH 28; 39 and 58 AU for RW Aur; 233 AU for LkHα 321; 68 AU for DG Tau; 32 AU for CW Tau and 84 AU for HH 30. The optical CCD detector was used with the G750M grating, centred on 6581 Å, and a slit of aperture 52×0.1 arcsec^2. Spectral sampling was 0.554 Å pixel^{-1}, corresponding to a radial velocity of $\sim$25 km^{-1} for the wavelength range covered, and spatial/angular sampling was 0.″05 pixel^{-1}. Long exposures were made of individual jet targets, such that each exposure time lay within the range $\sim$2000 s to 2700 s. One long exposure was made of each lobe of the bipolar jet from TH 28 on June 22 2002, and RW Aur on October 3 2002. Similarly, one long exposure was made of the approaching jet from DG Tau on December 1 2003 and CW Tau on December 21 2003, while two such long exposures (which were coadded to improve signal-to-noise) were made of the approaching jet from LkHα 321 on August 20 2002, and HH 30 on November 30 2003.

In total, this yielded eight spectra, in the transverse direction at the base of the jets,

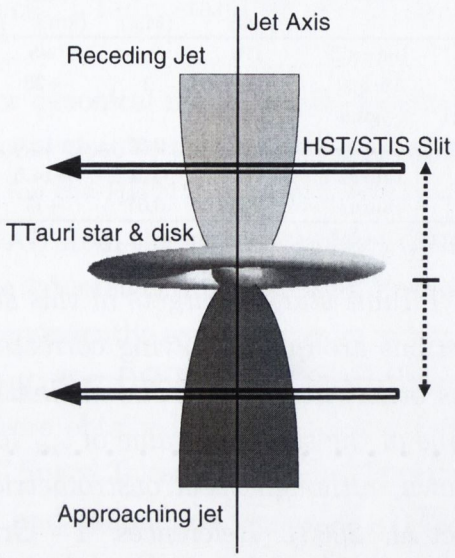

Figure 4.1: *HST/STIS observing mode used for all targets.*

which included Hα, [O I]$\lambda\lambda$6300,6363, [N II]$\lambda\lambda$6548,6583 and [S II]$\lambda\lambda$6716,6731. The data were calibrated through the standard *HST* pipeline (details of which can be found in Chapter 15 of the *HST*/STIS instrument handbook, http://www.stsci.edu/). IRAF data reduction tools were then used to perform subtraction of the reflected stellar continuum and removal of cosmic rays and defective pixels.

4.3 Results

The presence of jet rotation can be inferred from a difference in radial velocities on either side of the jet axis. As a qualitative indication of rotation, position-velocity contour plots of each emission line were examined for a tilt, or skew, in their shape. Following this, the data analysis procedure first involved centering the peak of each emission line in the spectrum on the nominal zero arcsecond position of the detector (since the peak is assumed to correspond to the jet axis), so that radial velocity comparisons between the two sides of the jet are conducted equidistant from the jet axis. Two methods were used to recentre the peak, i.e. a resampling technique and an interpolation technique, and the results compared to ensure accuracy. Single Gaussian fitting was then employed to determine where the emission peaked in each pixel row parallel to the jet axis, and the results were compared with those of a cross-correlation routine. From this analysis radial velocities were determined, and a radial velocity profile of the jet in the transverse direction was obtained. The difference in radial velocities equidistant on either side of the

jet axis was interpreted as jet rotation.

Analysis was not always possible for all of the observed optical emission lines (i.e. Hα, [O I]$\lambda\lambda$6300,6363, [N II]$\lambda\lambda$6548,6583 and [S II]$\lambda\lambda$6716,6731). Certain problems were common in a given emission line in many targets, e.g. the [O I]λ6300 line was sometimes blueshifted off the detector, the location of the [O I]λ6363 emission usually coincided with the location of a defective pixel, the [N II]λ6548 line was often too low in flux, and the Hα line was contaminated by stellar emission from any reflection nebula present thus making analysis difficult. The only exception regarding Hα emission was LkHα 321 where the greater Doppler shift of the jet away from the reflected stellar emission resulted in a clear separation of the two contributors to Hα emission. Only the spectrum from DG Tau's jet was bright enough to show two additional optical emission lines, one of which was identified as He I λ6678. However, neither of the two lines was bright enough to analyse. In order to clarify the results in subsequent figures, the orientation of the jet and slit for each target is illustrated in Figure 4.2.

4.3.1 Qualitative Indications of Rotation

Position-velocity contour plots for a sample of emission lines are shown in Figures 4.3 to 4.11, with corresponding contour levels given in Table 4.2. The positive direction of the y-axis corresponds to the slit direction in Figure 4.2. All radial velocities are systemic, i.e. they are quoted with respect to the mean heliocentric velocity of the star, which has been measured from photospheric lines. The lower order contours trace the outer jet channel where the jet is not so well collimated and where the lower velocities lie. If rotation is present, there will be a difference in radial velocities between the two sides of the jet. This difference will be evident graphically as a skew in the contours of the transverse position-velocity diagram. Such a skew is indeed observed in the outer contour lines for most cases. This suggests the presence of rotation in at least the low velocity component of the flow near the outer borders of the jet channel. The high velocity component, which is located much closer to the jet axis and gives rise to the emission peak (Bacciotti et al. 2000), appears not to be spatially resolved in these spectra. For this reason it is difficult to determine whether there is any velocity difference in the high velocity component between the the two sides of the flow, i.e. rotation for this velocity component is not detectable. On the other hand, the jet is clearly spatially resolved close to 0 km s^{-1}, as is evident in cases where the emission is extended along the dispersion direction in the contour diagrams. For example, for the DG Tau and CW Tau jets, the [O I] and [S II] emission extends over a range of almost 200 km s^{-1}.

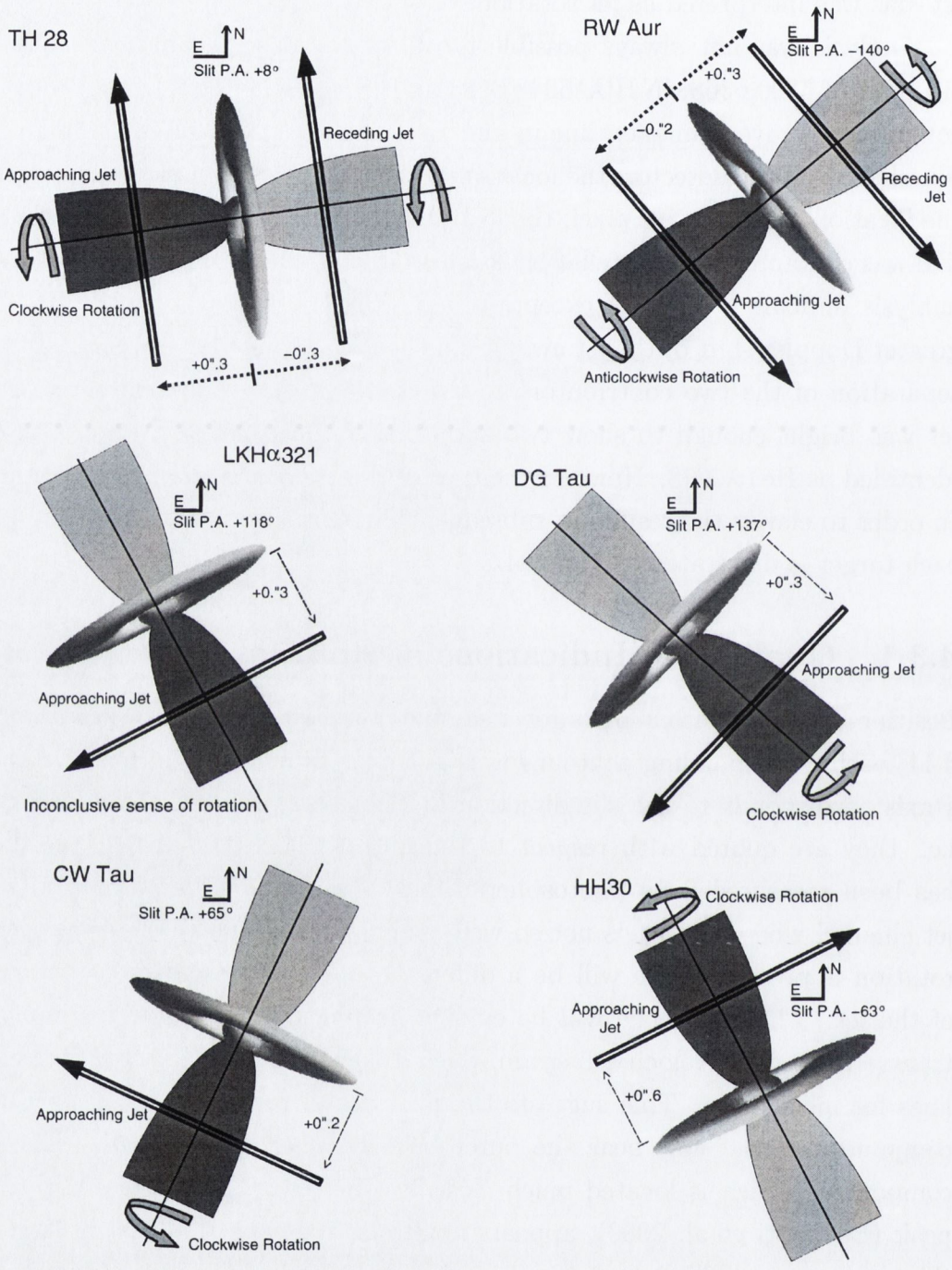

Figure 4.2: *Orientation of the jet and slit for each target. The arrow on the slit indicates the positive direction of the y-axis on the position-velocity contour plots, Figures 4.3 to 4.11, and the jet orientation can be compared with that given in the upper corners of each radial velocity profile, Figures 4.13 and 4.14. The arrow around the jet axis indicates the direction of rotation as the observer looks down the approaching jet towards the source. The distance between the star and the slit is given in terms of the offset of the star from the slit.*

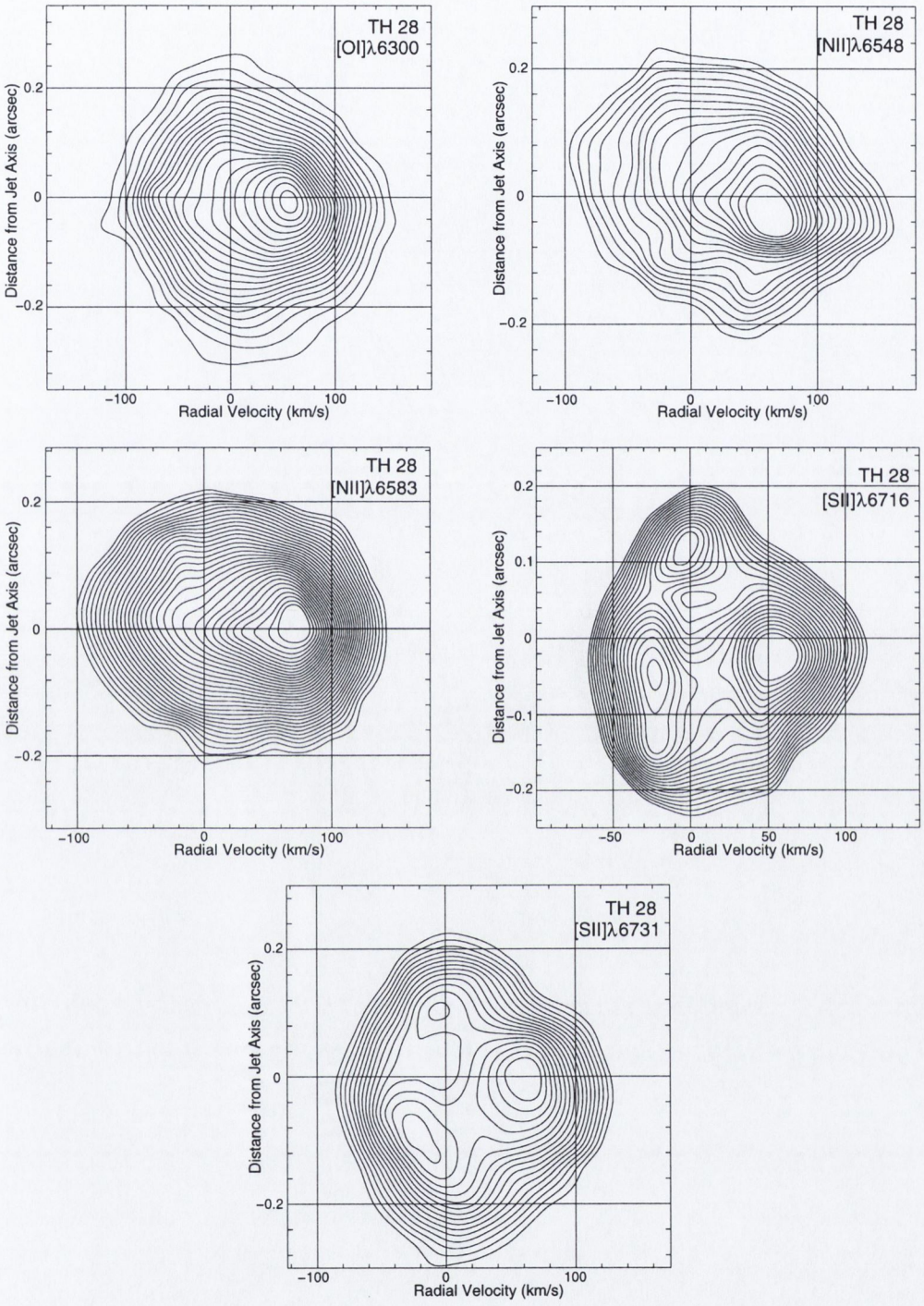

Figure 4.3: *Position-velocity contour plots for selected optical emission lines for the TH 28 receding jet. The [O I]λ6363 line was severely contaminated by a defective pixel. The skew in lower order contours is indicative of rotation in the outer jet channel, while the high velocity component remains unresolved. The positive direction of the y-axis is illustrated pictorially as the slit direction in Figure 4.2. Plots are corrected for systemic radial velocity, and contour values for each panel are given in Table 4.2.*

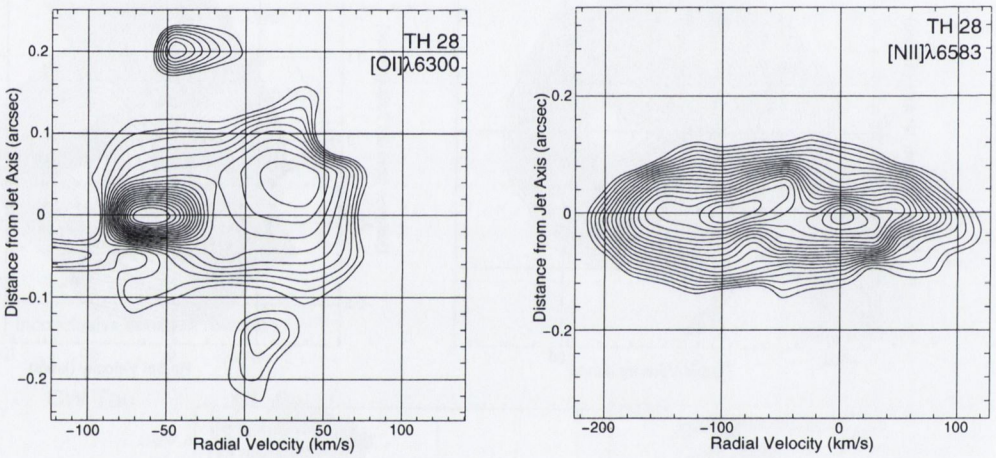

Figure 4.4: *Same as Figure 4.3, but for the TH 28 approaching jet. In this case, the [O I]λ6363, [N II]λ6548 and [S II]λλ6716,6731 lines were too faint to analyse.*

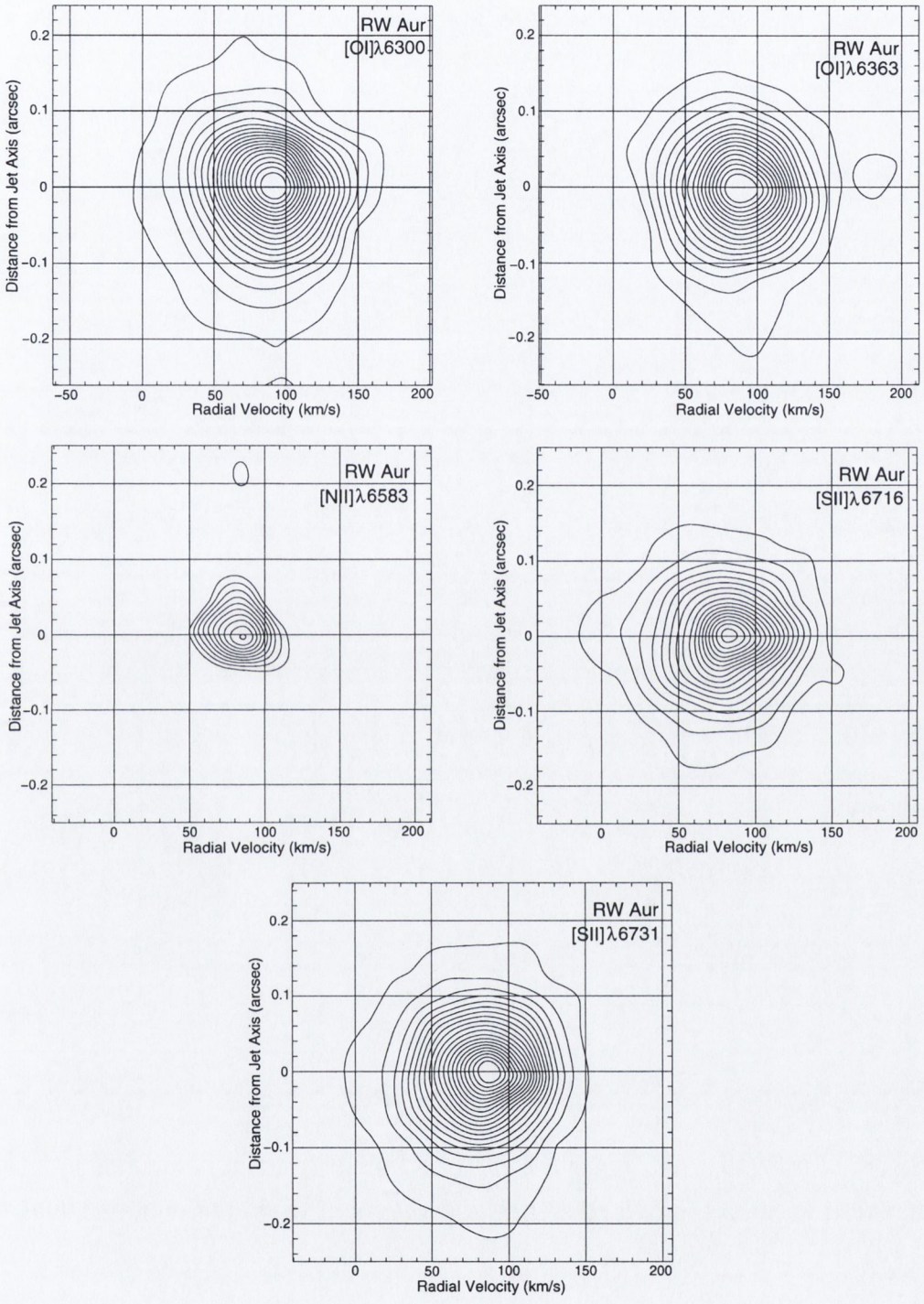

Figure 4.5: *Same as Figure 4.3, but for the RW Aur receding jet. The [N II]λ6548 line was redshifted to a point where it is blended with the Hα emission from the star.*

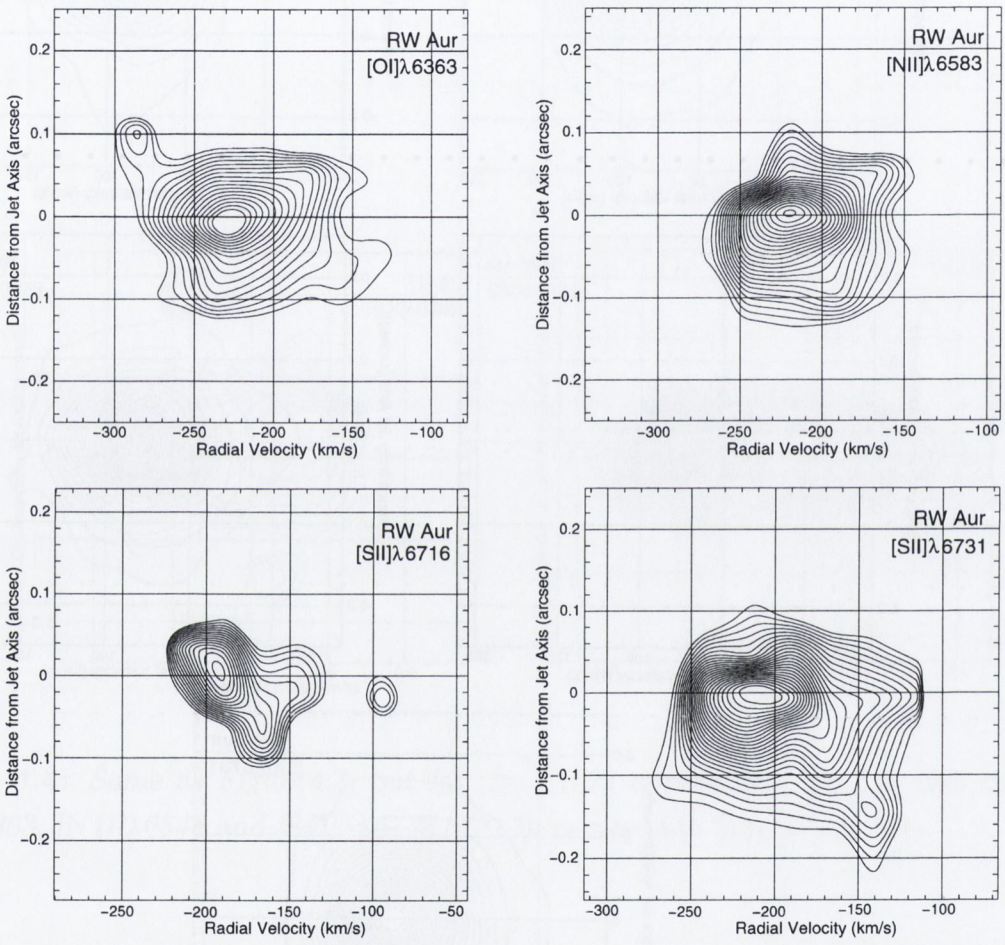

Figure 4.6: *Same as Figure 4.3, but for the RW Aur approaching jet. The [O I]λ6300 line was blueshifted off the detector and the [N II]λ6548 line was too faint to detect.*

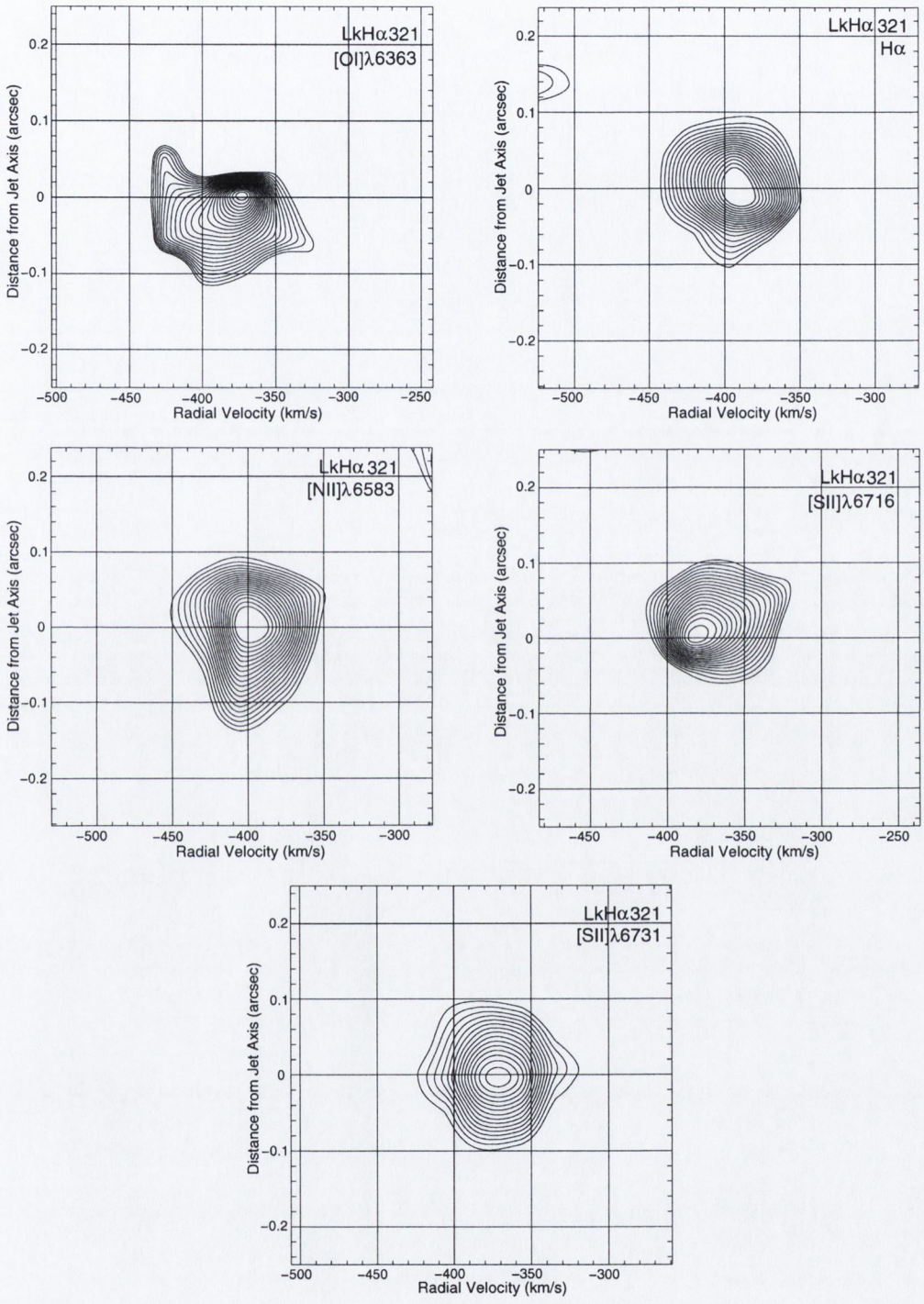

Figure 4.7: *Same as Figure 4.3, but for the LkHα 321 approaching jet. The [O I]λ6300 line was blueshifted off the detector and the [N II]λ6548 line was too faint to detect.*

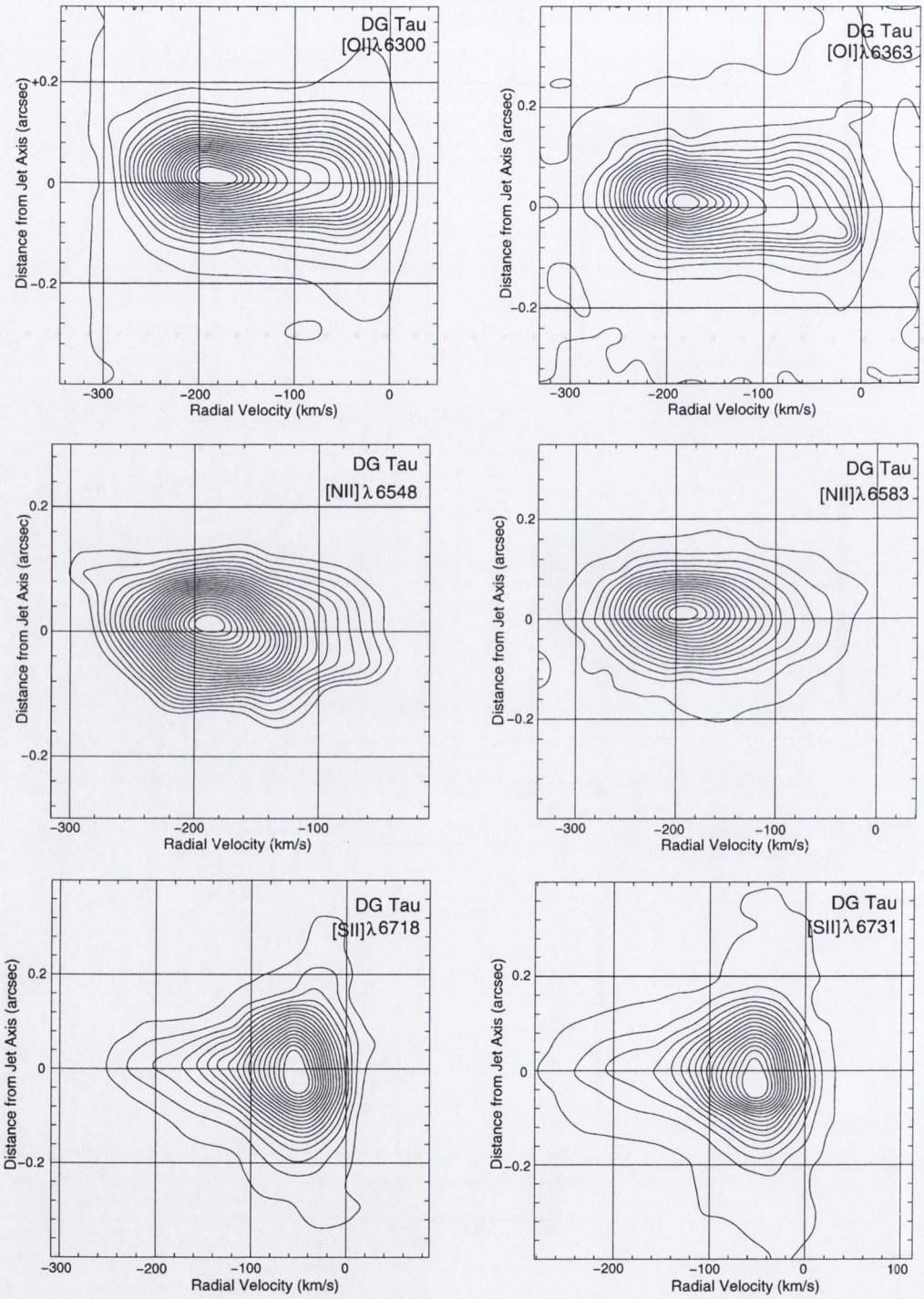

Figure 4.8: *Same as Figure 4.3, but for the DG Tau approaching jet.*

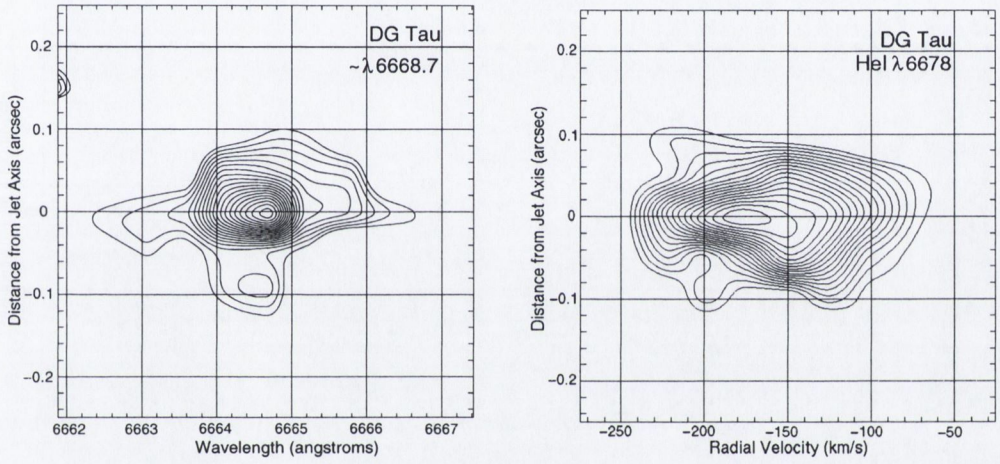

Figure 4.9: *Same as Figure 4.3, but for additional lines in the DG Tau approaching jet, which could be observed due to the higher level of signal-to-noise compared to other targets. One of these was identified as He I λ6678, while the other appears to have a rest wavelength of* $\sim 6668.7\,\text{Å}$, *assuming a radial velocity of* $180\,\text{km}\,s^{-1}$.

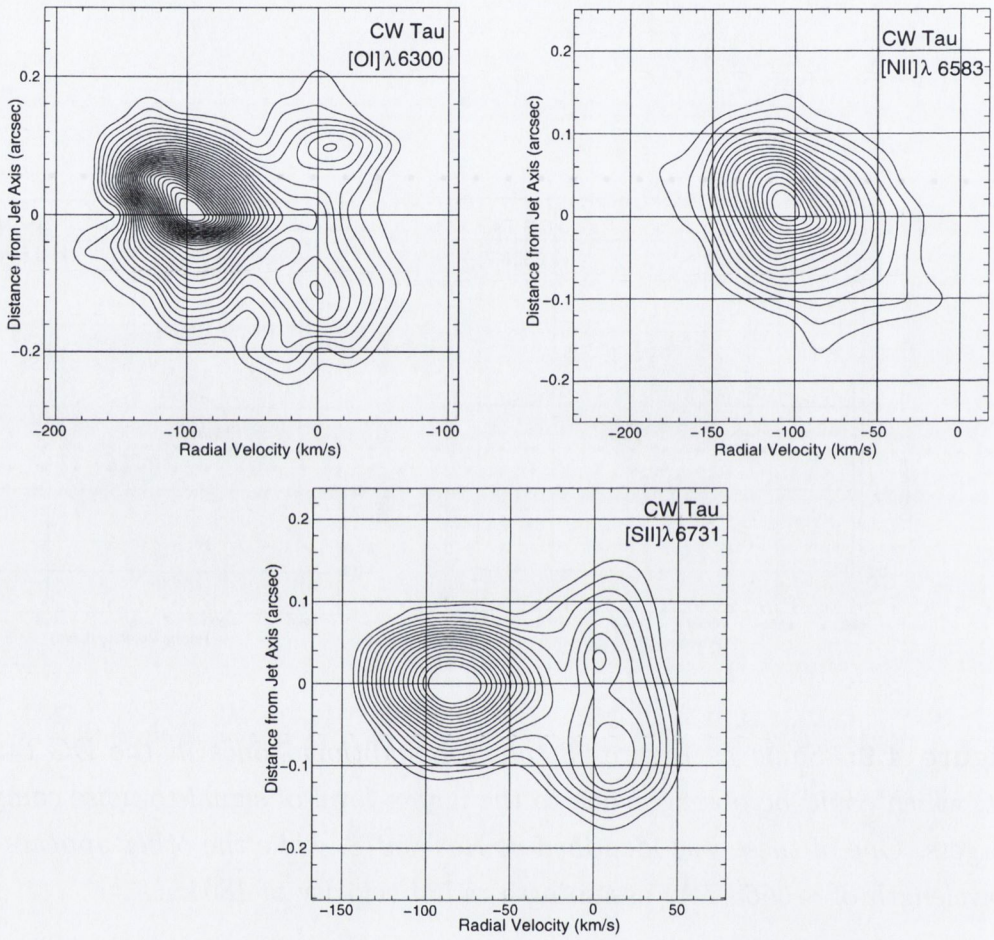

Figure 4.10: *Same as Figure 4.3, but for the approaching jet from CW Tau. The [O I]λ6363 and [S II]λ6716 lines were contaminated by a defective pixel, and the [N II]λ6548 line was too faint to analyse.*

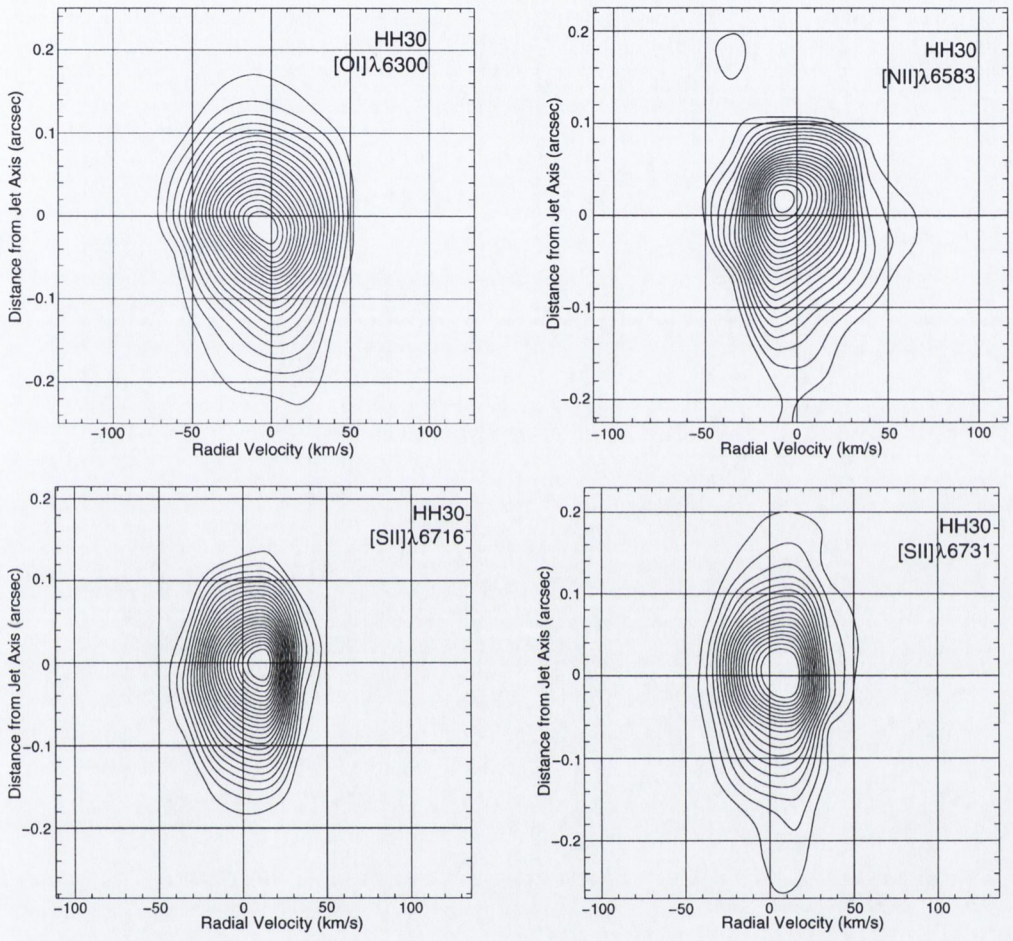

Figure 4.11: *Same as Figure 4.3, but for the approaching jet from HH 30. The [O I]λ6363 line was contaminated by a defective pixel, the [N II]λ6548 line was too faint to analyse. Although plots are corrected for systemic radial velocity, it appears that the value for HH 30 is underestimated in Table 4.1 by at least +4 km s^{-1}, as revealed by the apparent redshift of the lower velocity [S II] emission (see Figure 4.14 for a clearer illustration of this).*

Target	Emission line	Contour Floor	Contour Ceiling	Contour Interval
TH 28 receding jet	[O I]λ6300	5.0×10^{-15}	6.8×10^{-14}	3.0×10^{-15}
	[N II]λ6548	2.0×10^{-15}	1.2×10^{-14}	6.0×10^{-16}
	[N II]λ6583	5.0×10^{-15}	3.6×10^{-14}	1.0×10^{-15}
	[S II]λ6716	5.0×10^{-15}	1.1×10^{-14}	3.0×10^{-16}
	[S II]λ6731	5.0×10^{-15}	2.1×10^{-14}	1.0×10^{-15}
TH 28 approaching jet	[O I]λ6300	3.5×10^{-15}	8.9×10^{-15}	3.0×10^{-16}
	[N II]λ6583	3.5×10^{-15}	1.2×10^{-14}	5.0×10^{-16}
RW Aur receding jet	[O I]λ6300	6.5×10^{-15}	1.9×10^{-13}	1.0×10^{-14}
	[O I]λ6363	4.0×10^{-15}	6.8×10^{-14}	4.0×10^{-15}
	[N II]λ6583	4.0×10^{-15}	9.9×10^{-15}	6.5×10^{-16}
	[S II]λ6716	4.0×10^{-15}	1.0×10^{-13}	6.0×10^{-15}
	[S II]λ6731	4.0×10^{-15}	2.0×10^{-13}	1.0×10^{-14}
RW Aur approaching jet	[O I]λ6363	1.5×10^{-14}	4.7×10^{-14}	2.0×10^{-15}
	[N II]λ6583	2.0×10^{-15}	2.4×10^{-14}	1.0×10^{-15}
	[S II]λ6716	5.0×10^{-15}	2.0×10^{-14}	4.0×10^{-16}
	[S II]λ6731	5.0×10^{-15}	3.0×10^{-14}	1.0×10^{-15}
LkHα 321 approaching jet	[O I]λ6363	3.0×10^{-15}	7.6×10^{-15}	2.0×10^{-16}
	Hα λ6563	3.0×10^{-15}	2.0×10^{-14}	1.0×10^{-15}
	[N II]λ6583	3.0×10^{-15}	1.2×10^{-14}	5.0×10^{-16}
	[S II]λ6716	3.0×10^{-15}	8.0×10^{-15}	3.0×10^{-16}
	[S II]λ6731	3.0×10^{-15}	3.0×10^{-14}	1.0×10^{-15}
DG Tau approaching jet	[O I]λ6300	1.0×10^{-15}	4.4×10^{-13}	2.0×10^{-14}
	[O I]λ6363	1.0×10^{-15}	1.7×10^{-13}	1.0×10^{-14}
	[N II]λ6548	3.0×10^{-15}	2.6×10^{-14}	1.0×10^{-15}
	[N II]λ6583	3.0×10^{-15}	8.3×10^{-14}	5.0×10^{-15}
	He I λ6678	3.0×10^{-15}	1.0×10^{-14}	4.0×10^{-15}
	[S II]λ6716	3.0×10^{-15}	7.1×10^{-14}	4.0×10^{-15}
	[S II]λ6731	3.0×10^{-15}	1.6×10^{-13}	1.0×10^{-14}
CW Tau approaching jet	[O I]λ6300	5.0×10^{-15}	3.2×10^{-14}	1.0×10^{-15}
	[N II]λ6583	2.0×10^{-15}	1.3×10^{-14}	7.0×10^{-16}
	[S II]λ6731	3.0×10^{-15}	1.4×10^{-14}	7.0×10^{-16}
HH 30 approaching jet	[O I]λ6300	7.0×10^{-15}	6.4×10^{-14}	3.0×10^{-15}
	[N II]λ6583	3.0×10^{-15}	2.3×10^{-14}	1.0×10^{-15}
	[S II]λ6716	6.0×10^{-15}	5.0×10^{-14}	2.0×10^{-15}
	[S II]λ6731	1.0×10^{-14}	9.5×10^{-14}	5.0×10^{-15}

Table 4.2: *Linear contour intervals relating to position-velocity plots, Figures 4.3 to 4.11, in units of erg cm^{-2} s^{-1} Å^{-1} arcsec^{-2}.*

4.3.2 Quantitative Analysis

To give a quantitative estimate of the observed radial velocity differences, it was firstly necessary to ensure that I measured radial velocities at equal distances on either side of the jet axis. To this purpose, I assumed that the peak of the high velocity emission traces the position of the axis and measured, with a Gaussian fit along the dispersion direction, its distance from the nominal centre of the slit. I then shifted the image, recentering the emission peak on the nominal zero arcsecond position. In all cases a small offset (≤ 0.5 pixels) was required (see Section 4.4.7 for further discussion).

Once the emission was centred on the nominal zero arcsecond position of the detector, single Gaussian fitting was then used to find the peak of the intensity profile for each pixel row parallel to the jet axis (i.e. parallel to the x-axis in the position-velocity plots), thus giving a radial velocity profile of the jet in the transverse direction for each emission line, Figures 4.13 and 4.14. The position angle, derived from Figure 4.2, is given in the upper corners of each velocity profile plot. Where lower and higher velocity jet material is clearly distinguishable, the plots have been divided in to lower and higher velocity components. Note that the profile of DG Tau, in particular, shows how different emission lines trace different velocities within the jet: [N II] lines appear to trace only higher velocities; [O I] lines trace higher and lower velocities; and [S II] lines mainly trace lower velocities. Plots reveal that, in general, the on-axis jet material is travelling fastest while the borders of the jet are travelling slower, resulting overall in an v-shaped profile. However, these profiles are not symmetrical. Velocities on one side of the axis are lower than on the other. Furthermore, each emission line traces a different degree of asymmetry. In general, [O I] lines are clearly asymmetric, while [S II] lines show much more symmetric profiles. This combination of contributions from different emission lines and different velocity components can draw from the clarity of some of these radial velocity plots. The clearest case is perhaps the plot for the TH 28 receding jet. Here it can be seen how radial velocity varies with distance from the central axis, an important parameter in constraining models of outflow dynamics, e.g. Pesenti et al. (2004).

The location of the peak intensity of pixel rows on either side of the central row were then compared for velocity differences. Figure 4.12 shows an example of the intensity profiles of each pair of pixel rows symmetric about the jet axis, while the single curve at the bottom in each case is the intensity of the central on-axis pixel row. Two methods were used in velocity measurements. The first was a cross-correlation technique (a standard statistical method of estimating the degree to which two series are correlated, and may be used to determine the degree of similarity between two similar images, or, with the addition of a linear offset to one of the images, the spatial shift or spatial correlation

between the images), the results of which are independent of the shape of the line profile. The second was a Gaussian fitting technique, which acts as a suitable check given the simple shape of the line profile in most cases. Specifically, each pair of pixel rows mirrored in distance from the jet axis was cross-correlated, and Gaussian fits for each pair of rows were also compared. The outcomes of the two methods were consistent, showing clear radial velocity differences of up to $\sim 30\ (\pm\ 5)\ \mathrm{km\,s^{-1}}$ for opposing jet edges in all jet targets observed, see Table 4.3 and corresponding plots in Figures 4.15 and 4.16. The *sign* of the velocity difference was determined by a subtraction of the peak radial velocity of each pixel row above the central row on the CCD from the one below the central row corresponding to the same distance. In other words, a *negative* slope in the position-velocity contour tilt between two points either side of the axis corresponds to a *positive* velocity difference.

Given sufficient signal-to-noise, it is possible to routinely measure radial velocity differences to one fifth of the velocity sampling, giving an accuracy of $\pm 5\,\mathrm{km\,s^{-1}}$. In a small number of cases, flagged in the table with an asterisk, the emission had to be filtered out of a background which was causing velocity measurements to be artificially changed due to either oversubtraction of the background or low signal-to-noise at crucial positions.

Note that the [O I]λ6300 line for the TH 28 approaching jet is not included in Figure 4.13 since the profile of this emission line did not allow measurement of velocity peaks with Gaussian fitting. In these cases, measurements were made using a cross-correlation routine alone, resulting only in velocity difference measurements. Also, it appears that the value for the HH 30 systemic velocity reported in Table 4.1 is underestimated by at least $+4\,\mathrm{km\,s^{-1}}$, as revealed by the apparent redshift of the lower velocity [S II] emission in Figure 4.14 which originates in the *approaching* jet.

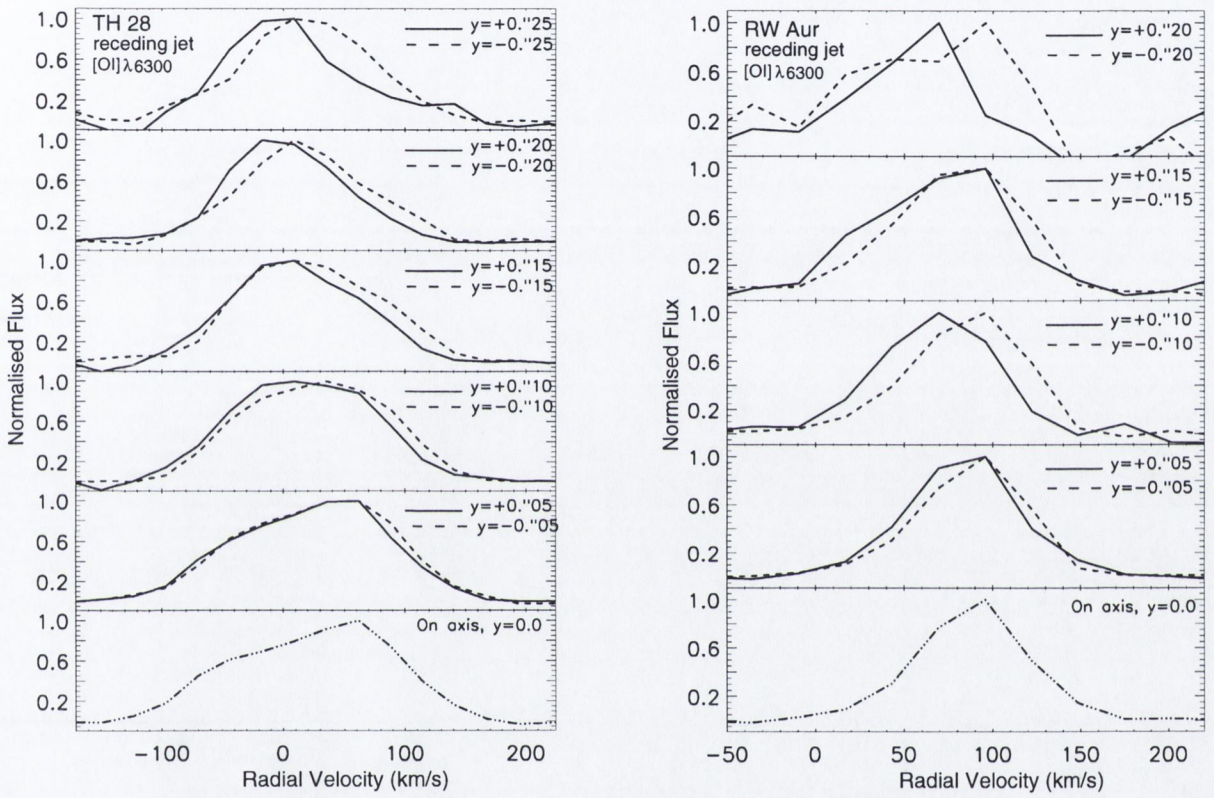

Figure 4.12: *Normalised intensity profiles along horizontal cuts for a sample of position-velocity plots, to illustrate peak velocity differences. Each plot compares the intensity peaks at positions symmetrically opposed with respect to the jet axis. The displacement of one peak with respect to the other illustrates the difference in radial velocities between one side of the jet axis and the other.*

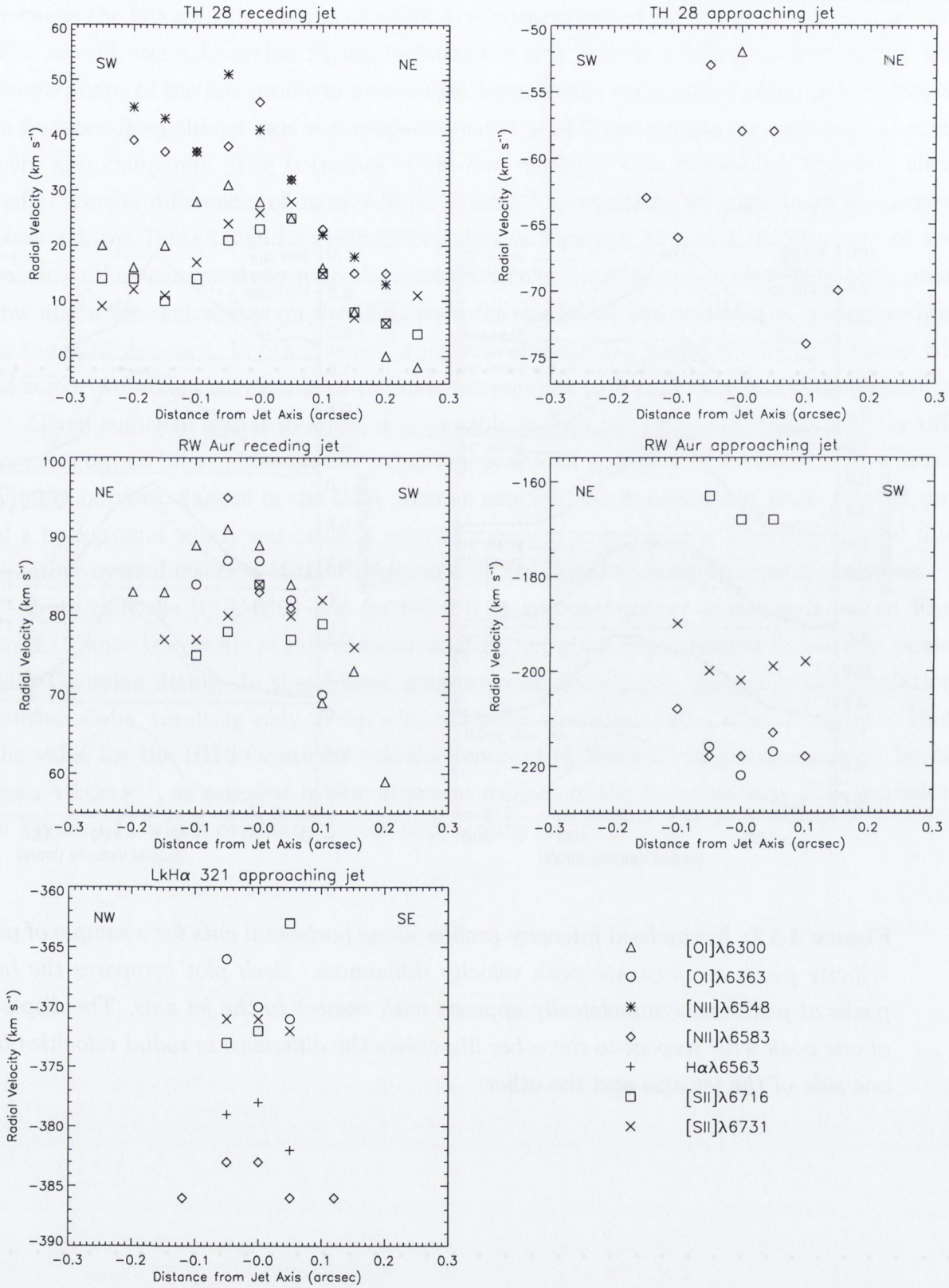

Figure 4.13: *Radial velocity profile across the jet in various optical emission lines LkHα 321. Profile asymmetries are interpreted as resulting from jet rotation. All radial velocities are corrected for systemic radial velocity.*

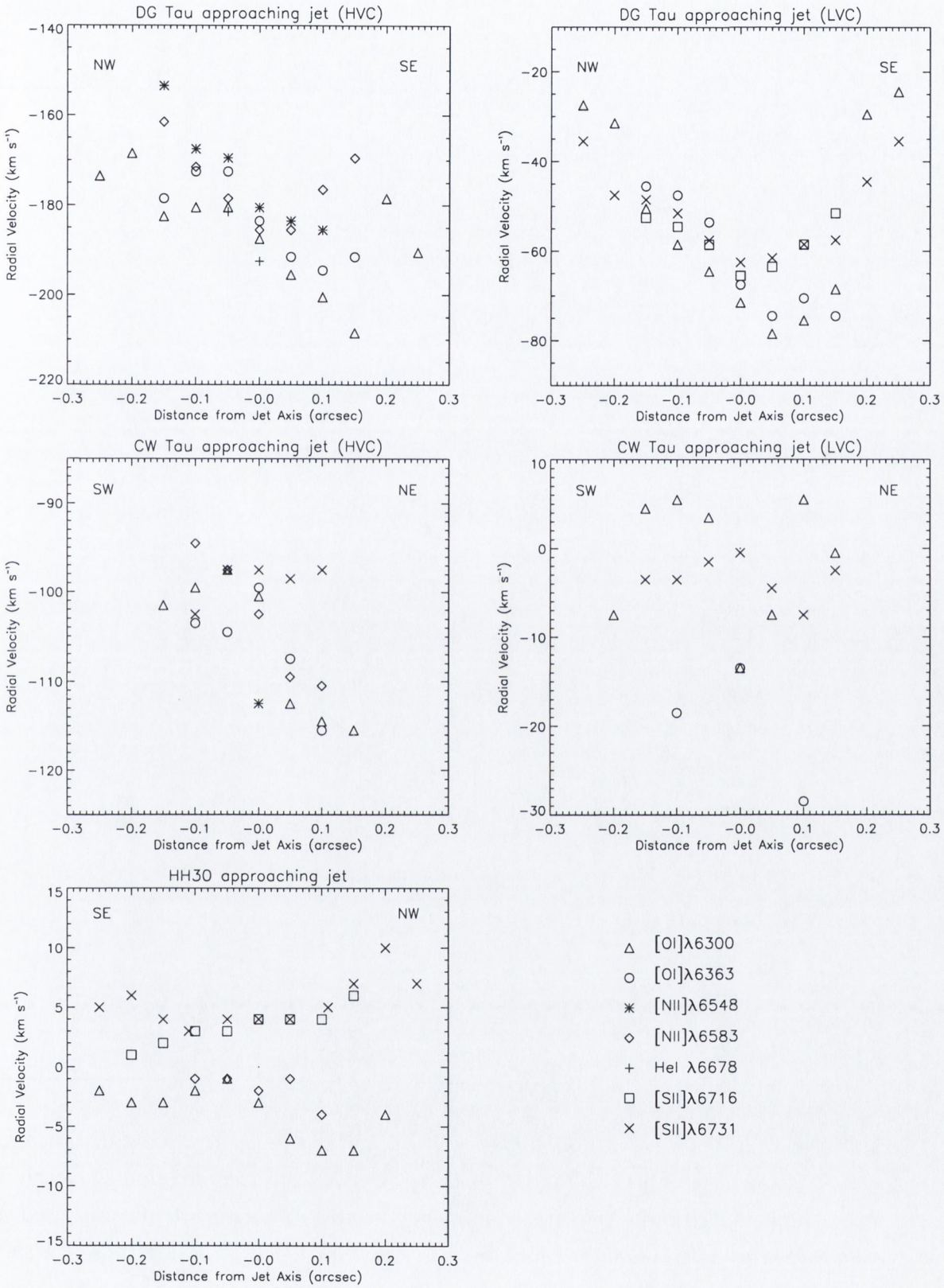

Figure 4.14: *Same as Figure 4.13 but for the approaching jets from DG Tau, CW Tau and HH 30. Due to their spread, DG Tau and CW Tau have been divided into a higher (HVC) and lower velocity component (LVC). All velocities are corrected for systemic radial velocity.*

Target (Distance from star)	Distance to jet axis (arcsec)	Δv_{rad} for [O I]λ6300 ($km\,s^{-1}$)	Δv_{rad} for [O I]λ6363 ($km\,s^{-1}$)	Δv_{rad} for [N II]λ6548 ($km\,s^{-1}$)	Δv_{rad} for Hα ($km\,s^{-1}$)	Δv_{rad} for [N II]λ6583 ($km\,s^{-1}$)	Δv_{rad} for [S II]λ6716 ($km\,s^{-1}$)	Δv_{rad} for [S II]λ6731 ($km\,s^{-1}$)
TH 28	0.05	5	...	20	...	6	-5	-4
receding	0.10	12	...	15	...	14	-1	1
jet	0.15	11	...	25	...	21	3	3
(0.″3)	0.20	16	...	32	...	25	8	7
	0.25	23	...	...	...	...	10	-1
TH 28	0.05	2*	...	...	...	5	...	...
approaching	0.10	3*	...	...	...	8	...	...
jet	0.15	8	...	...	...	7	...	...
(0.″3)	0.20	15	...	...	...	...	...	...
RW Aur	0.05	7	5	...	...	14	1	-1
receding	0.10	20	14	...	...	...	-4	-5
jet	0.15	10	...	...	...	...	...	2
(0.″3)	0.20	24	...	...	...	...	...	...
RW Aur	0.05	...	1	...	...	-5*	5	1
approaching	0.10	...	...	...	...	10	...	8
jet	0.15	...	...	...	...	...	...	...
(0.″2)	0.20	...	...	...	...	...	...	...
LkHα 321	0.05	...	5	...	3	3	-10*	1
approaching	0.10	...	...	...	...	0	...	...
jet	0.15	...	...	...	...	...	...	...
(0.″3)	0.20	...	...	...	...	...	...	...
DG Tau	0.05	15 (14)	19 (21)	14	...	7	5	4
approaching	0.10	20 (17)	22 (23)	18	...	5	4	6
jet	0.15	26 (18)	13 (29)	...	...	8	-1	9
(0.″3)	0.20	10 (-2)	...	...	...	...	...	...
	0.25	17 (-3)	...	...	...	...	...	...
CW Tau	0.05	15 (11)	...	...	...	12	...	2 (3)
approaching	0.10	15 (0)	...	...	...	26	...	-6 (4)
jet	0.15	12 (5)	...	...	...	...	...	2 (-1)
(0.″2)	0.20	...	...	...	...	...	...	...
HH 30	0.05	5	...	...	...	0	-1	0
approaching	0.10	5	...	...	...	3	1	-2
jet	0.15	4	...	...	...	...	-4	-3
(0.″6)	0.20	1	...	...	...	...	...	-4

Table 4.3: *Radial velocity differences, Δv_{rad}, across the jet at a fixed distance from the source (given in the first column). In those cases where the emission is clearly divided into a higher and lower velocity component, double Gaussian fitting was used and the results for the lower velocity component are given in brackets beside those for the higher velocity component. The asterisks mark data points which have been manually filtered out of a low signal-to-noise environment. Where dots appear in the table, the emission was either shifted off the CCD, or was too faint to analyse. The accuracy reached with the data analysis is approximately $\pm 5\,km\,s^{-1}$.*

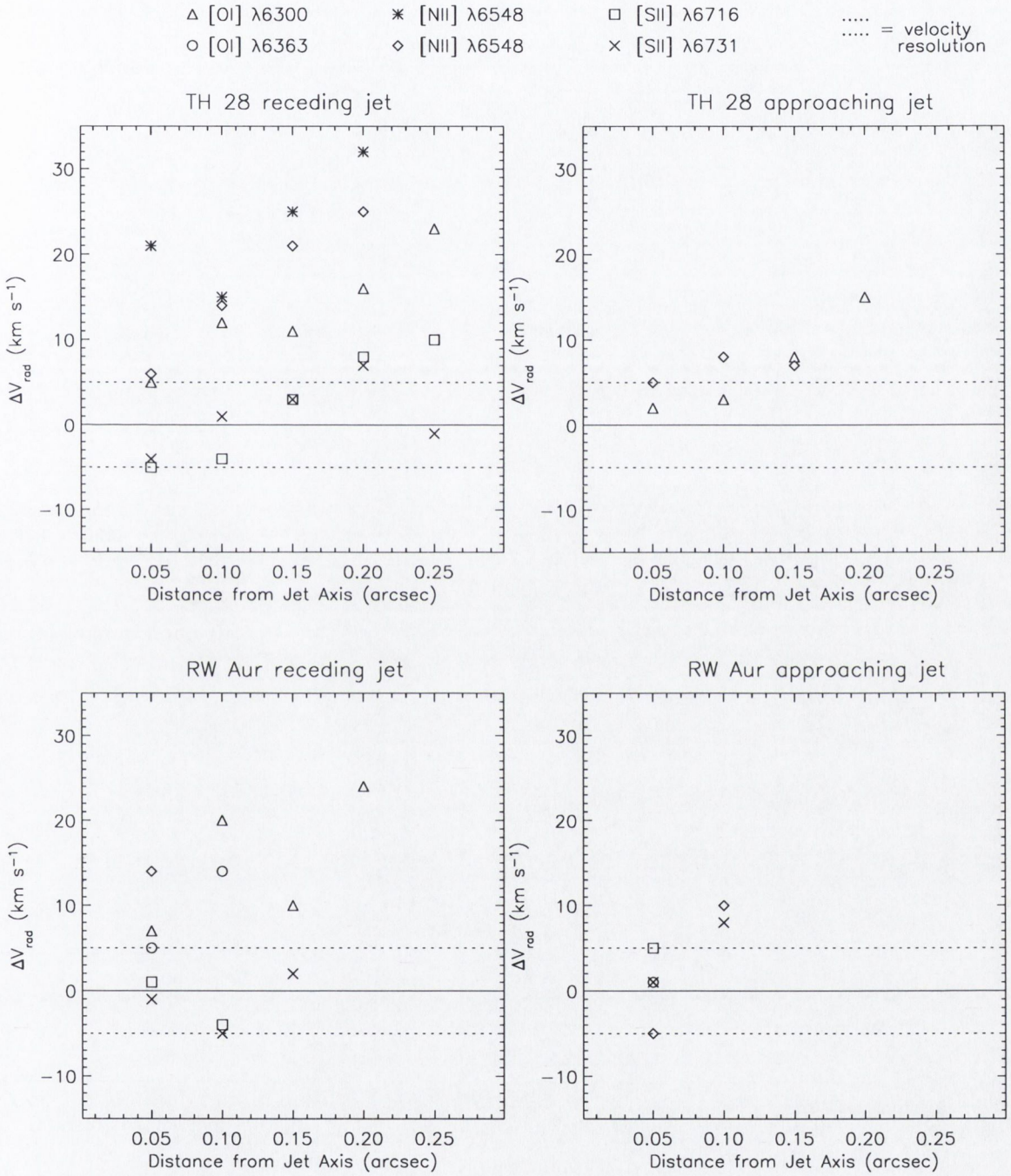

Figure 4.15: *Radial velocity differences, Δv_{rad}, as a function of distance from the jet axis. All targets show positive radial velocity differences. Furthermore, the sense of rotation of the bipolar jet lobes are in agreement in both cases.*

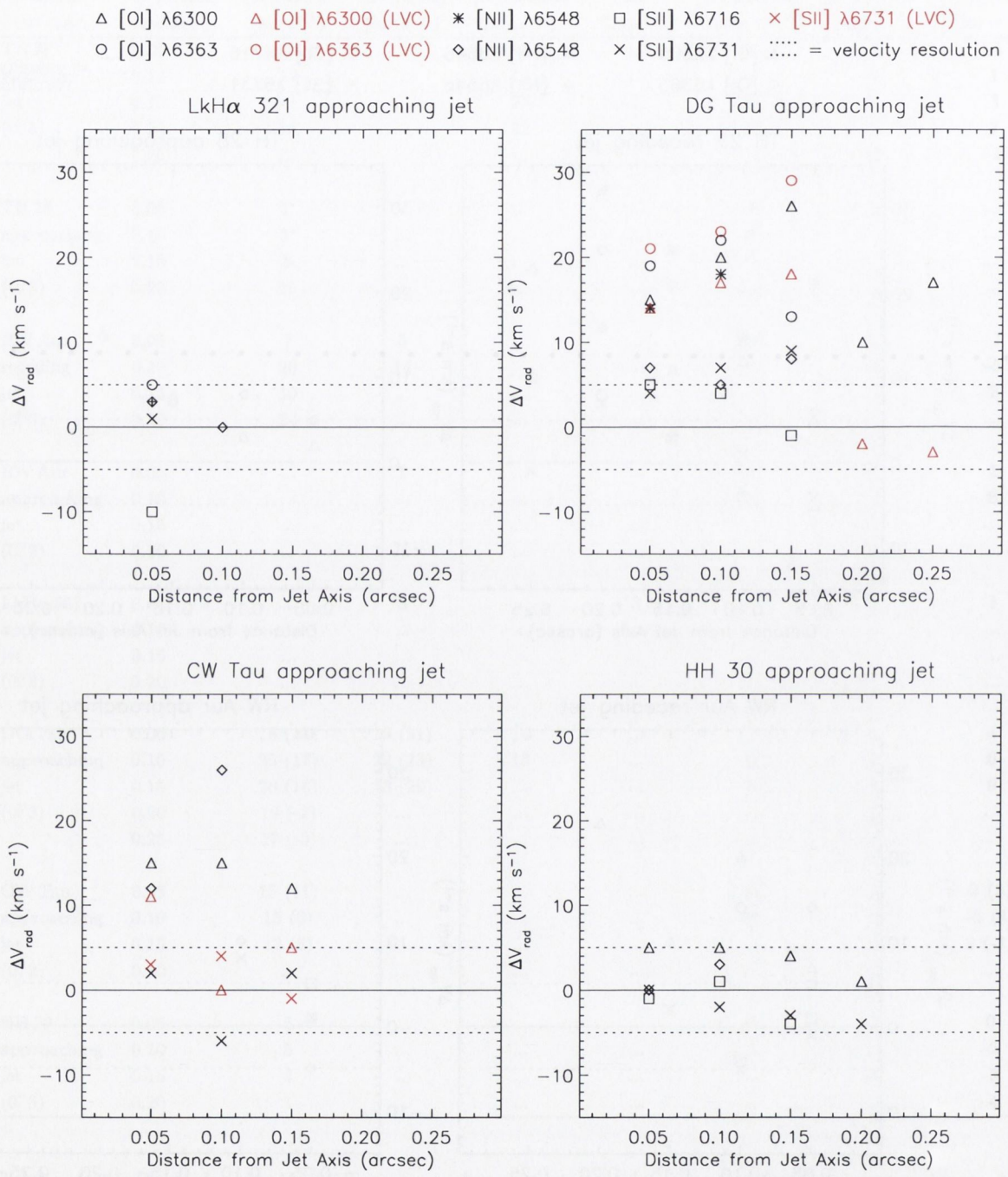

Figure 4.16: *Radial velocity differences, Δv_{rad}, as a function of distance from the jet axis. All targets, except LkHα 321, show positive radial velocity differences. The [O I] emission line shows the strongest signatures in all other targets, and so it seems to be the clearest indicator of velocity differences. For HH 30, therefore, it can be said that velocity differences are positive even though the values are close to the error bars. The red points represent the lower velocity component in cases where double Gaussian fitting was necessary.*

4.4 Discussion

Assuming that emission from the jet is axially symmetric, I interpret my findings of velocity differences between the two sides of the jet, Table 4.3, as indications of rotation at its base. Most importantly, in the cases of TH 28 and RW Aur, the receding and approaching jet lobes were found to rotate with the same sense. This implies that the helicity in the receding and approaching lobes (i.e. the handedness of toroidal with respect to the poloidal velocity) is opposite in opposite directions. Such a result is predicted by MHD models where the ambient field is wrapped around due to disk rotation, but will occur for any bipolar outflow emerging from a disk that is rotating in one direction. Before looking at each target individually, there are a few general comments to be made about the results in Table 4.3.

Firstly, in some cases, the velocity difference measurements close to the jet axis (i.e. at the 0.″05 position) are noticeably smaller than points further away. Also, velocity differences are generally higher further from the jet axis than at intermediate distances. This effect may at first appear in contradiction with the notion that the central portions of the jet should rotate faster. Detailed comparisons with 'Disk wind' model predictions (e.g. Pesenti et al. 2004; Dougados et al. 2004) show, however, that the apparent decrease of the observed velocity difference towards the jet axis is likely to be due to the effects of projection and beam smearing. Such an effect is more important for regions closer to the axis, while the values measured at the outer jet borders are less contaminated and so are in better agreement with theoretically predicted toroidal velocities. In other words, this effect does not reflect a true kinematic feature, but is expected on the basis of MHD acceleration models when combined with my observing mode. Secondly, it should be noted that the size of velocity differences in different emission lines does not represent scattering around an average value but rather is due to the fact that emission has its origin at different positions along the line of sight. And lastly, the [N II] lines show higher velocities and smaller spatial FWHM values compared to other emission lines, illustrating that they trace the central more collimated higher velocity region of the flow, (Bacciotti et al. 2000; Martin et al. 2003; Pesenti et al. 2004).

4.4.1 TH 28

The set of results for the TH 28 receding jet is one of the clearest. Velocity differences are positive, with a few exceptions mainly in the [S II] lines. Also, the data close to the jet axis are not well resolved as explained in the previous paragraph. The stronger [O I] and [N II] lines have values of 5 and 6 $\mathrm{km\,s^{-1}}$ at 0.″05 from the axis compared to 10 to 20 $\mathrm{km\,s^{-1}}$

further from the axis, while the outer jet channel seems to have higher radial velocity differences of about 24 km s^{-1}. Values in the approaching jet are less clear, but [N II] and [O I] emission gives positive differences consistent with the receding jet. All other usable data points fall within the error bars about zero. Globally, I find indications that both lobes of the jet rotate in a clockwise direction, looking down the approaching jet towards the source (Figure 4.2), with a measured radial velocity difference of 10 to 25 km s^{-1}, at a de-projected distance of 52 AU from the star.

4.4.2 RW Aur

The RW Aur bipolar jet also shows clear indications of rotational velocities. Exceptions mainly lie in the [S II] values of the receding jet. Also, points close to the jet axis show smaller radial velocity differences, as previously discussed. However, the [O I] lines give clear results with higher radial velocity difference evident at 0.″2 from the jet axis. The values for the approaching jet are less definite, but nevertheless velocity differences outside the error bars are positive, in line with the receding jet. Overall, results show an anticlockwise rotation looking down the approaching jet towards the source (Figure 4.2), again with radial velocity differences of 10 to 25 km s^{-1}, at a de-projected distance of 39 to 58 AU from the star (depending of jet lobe). These findings are consistent in magnitude and direction with results of similar research on the RW Aur jet (Woitas et al. 2005) in which rotational velocities of the same sense and in the range of 10 to 20 km s^{-1} have been observed, in the form of radial velocity differences between the borders of the flow. For that study *HST*/STIS was also used, but the spectra were taken in a set of positions along the jet such that the slit direction was *parallel* to the jet axis.

4.4.3 LkHα 321

In the case of LkHα 321, located at 550 pc (more than three times the distance of the other targets), emission lines were very faint despite having combined two spectra to increase the signal-to-noise ratio. Velocity differences lie within error bars about zero in all cases, except for the [S II]λ6716 emission which gives a value of -10 km s^{-1}. This is not likely to be a physical phenonenon since it is not mirrored by the [S II]λ6731 emission, nor by any other emission. It is also not consistent with the fact that all [S II] emission for the other targets consistently shows no rotation, regardless of the results for other emission lines of the same target. The anomalous result is likely to be due to erroneous continuum fitting, although care was taken to re-examine this possibility and no improvement could be made. Overall, the results for the LkHα 321 jet prove inconclusive (Figure 4.2).

4.4.4 DG Tau

Perhaps the best dataset is that for DG Tau. Emission in all optical lines has high signal-to-noise and is uncontaminated by defective pixels. In this case the indications of jet rotation are significant with radial velocity differences of comparable magnitude recorded for all emission lines. Even the [S II] lines, which usually only show hints of rotation, give reasonable velocity differences of 6 to 9 km s^{-1} at 0.″1 to 0.″15 from the jet axis. For the [O I] and [N II] doublets, values range from 10 to 35 km s^{-1} at 0.″05 to 0.″15 from the jet axis, and at a de-projected distance of 68 AU from the star. Referring to Figure 4.2, jet rotation is clockwise looking down the approaching jet towards the source. The velocity differences are of the same magnitude and direction as those reported by Bacciotti et al. (2002), where values of 5 to 10 km s^{-1} were measured with the *HST*/STIS slit placed *parallel* to the DG Tau approaching jet.

4.4.5 CW Tau

In the case of CW Tau, the usable data is limited due to faint emission or contamination by defective pixels. Otherwise, the signal-to-noise is good, and clear contour tilts are evident in the position-velocity diagrams available. Radial velocity differences are significant, reaching 12 to 26 km s^{-1} at 0.″05 to 0.″10 from the jet axis, and at a de-projected distance of 32 AU from the star. There is a clear separation in lower and higher velocity components for the [S II] emission but, as with many other targets, radial velocity differences are scattered about zero and within the error bars in these lines. Referring to Figure 4.2, jet rotation is clockwise looking down the approaching jet towards the source.

4.4.6 HH 30

The HH 30 bipolar jet lies almost in the plane of the sky. Therefore, as would be expected, both the position-velocity diagrams and radial velocity plots for the approaching jet clearly indicate that the jet possesses a low radial velocity, once the systemic radial velocity of the system has been taken into account. Differences in radial velocities detected for HH 30 lie close to or within the error bars about zero. Nonetheless, the results are reinforced by the visible tilt in the [O I]λ6300 contour plot. Therefore, it is possible to say that radial velocity differences for this target range from 5 to 8 km s^{-1} at 0.″05 to 0.″2 from the jet axis, and at a de-projected distance of 84 AU from the star. Referring to Figure 4.2, jet rotation is clockwise looking down the approaching jet towards the source.

4.4.7 Sources of Error

The fact that the same sense of jet rotation with respect to the orientation of the slit/detector (Figure 4.2) is detected for all jets in the survey (with the possible exception of LkHα 321) might be regarded as unusual. It is reassuring that I obtain *much lower* radial velocity differences in the case of the HH 30 [O I]λ6300 emission compared to the higher [O I]λ6300 differences observed for the other targets. This implies that I am not measuring an instrumental effect (as I am comparing the *same* rows on the CCD detector in all cases). Nevertheless, a careful study of possible instrumental error was conducted.

4.4.7.1 Instrumental Error

To expand, it should be mentioned that during the first stage of data reduction when each emission peak was recentred to the nominal zero arcsecond position, a trend was observed in the pixel offsets from the jet axis for each emission line. Peak offsets ranged from 0.1 to 1.5 pixels depending on the target, although offsets in emission lines for a given target varied by <0.5 pixels. This highlighted three types of possible instrument misalignments which had the potential to contribute to position-velocity contour tilt and thus mimic rotation (details of which were revealed by the Space Telescope Science Institute helpdesk, query reference CNSHD478125).

The first is physical tilt (i.e. a tilt of the slit with regard to the nominal observing position angle), and is known to have a value of $+0.22\,^{\circ}$ in the optical region. The second is optical distortion tilt (i.e. the slit image on the detector is curved and tilted) which varies in angle across the detector depending on the grating used, and is known to have a value of $+0.001^{\circ}$ in the optical region. The third is position angle error (i.e. an error in the slit position angle specified for the observations with regard to the true jet position angle), and could be on the order of a few degrees. An analysis of the error contribution of each was conducted and all were found to be insignificant (i.e. $< 1\,\mathrm{km\,s^{-1}}$ which is well within the rotation error bars of $\pm\,5\,\mathrm{km\,s^{-1}}$). Nonetheless, all erroneous tilts were corrected for before data analysis was conducted. The *HST* pipeline calibration accounted for physical tilt, while optical distortion was adequately accounted for by recentering the emission peaks. The remaining tilt to be addressed is possible inaccuracy in the position angle specified for the observations.

Conceivably, a slight misalignment of the slit with respect to the transverse direction of the jet (i.e. inaccurate position angle specified in the pointing of the instrument) may produce a signature similar to rotation. In this case, the position of the real jet axis will then be offset with respect to the nominal zero arcsecond position, and the slit will not be exactly perpendicular to the jet axis but at a slight angle. Although I have shifted the

spectral image back to the zero arcsecond position to account for the erroneous offset (as previously described in Section 4.3), the erroneous angle subtended remains a possible problem. It could produce a rotation signature even in a non-rotating jet, since the high and low velocity components of the jet are at different spatial locations on the CCD with respect to the zero arcsecond row of pixels. This would imply that I am not probing symmetric regions of the jet with respect to its real axis. Given such a misalignment has occurred, the extent of the contamination does not, however, have a dramatic affect on my results. The main evidence negating the significance of this effect is that the same contour tilt does not occur in *all* emission lines, as would be the case given a position angle error. [S II] emission shows little or no tilt while [O I] and [N II] emission show clear tilts, and so any error in the position angle has insignificant impact on the spectra once recentering has been carried out. Furthermore, for RW Aur, the same position angle was used here for slit positioning as in a previous study (Woitas et al. 2004), where it was found that the magnitude of the false rotation signature contamination due to incorrect position angle was at most 1 to $5\,\mathrm{km\,s^{-1}}$ prior to centering the peak. However, the sense of the false signature is in fact opposite in direction to that of the jet's rotation, and so the values I have measured are actually lower limits on any true rotation. It is also possible that marginal corrections may make the problem worse, and so a careful study was made of the effect of recentering on velocity differences values. Recall from Section 4.3 that both resampling and interpolation techniques were used. The impact was minimal, falling well within error bars, and typically less than $1\,\mathrm{km\,s^{-1}}$.

Hence, all known instrumental contributions were corrected or compensated for, although they proved insignificant. Unknown instrumental effects may still be present, but any such effects would result not only in the same sense of jet rotation but also in the same *magnitude* of radial velocity differences. Although I find the same sense of rotation, I do find varying magnitudes. HH 30 is the prime example of this, where rotation in the [O I]λ6300 line is measured at only $5\,\mathrm{km\,s^{-1}}$ compared with the other sources which reach 20 to $30\,\mathrm{km\,s^{-1}}$. Furthermore, a similar analysis of the radial velocities within the jets from T Tauri stars DG Tau (Bacciotti et al. 2002) and RW Aur (Woitas et al. 2004) with the slit placed *parallel* to the jet axis yielded results in agreement with my observing mode in which the slit is perpendicular to the jet axis. Any instrumental effect mimicking rotation would have to cause the same errors when the slit/detector is rotated by 90 °, which is not a likely scenario.

4.4.7.2 Archival Data Check

As a final check, I searched the *HST*/STIS archive for data from another astrophysical object observed with the same instrument configuration as my optical survey. The best dataset I could find which has a flux level comparable to my data in terms of intensity and spatial extension, and which hits the detector in the region of the [O I] doublet (since this is where I see the largest contour tilts), was data for Menzel 3 (Mz 3). M 3 is one of the most complex bipolar nebulae, often called the Ant Nebula due to its characteristic morphology (Menzel 1922). A long-slit spectrum of Mz 3 (of exposure time 290 s) was obtained with *HST*/STIS on June 23, 2002 (Proposal ID 9050). The same grating (G750M) and detector (CCD) were used here as in my optical survey, but the slit aperture size used was slightly different (i.e. $52\times0.05\,\mathrm{arcsec}^2$ rather than $52\times0.1\,\mathrm{arcsec}^2$ as in my observations). Nevertheless, these slits are coaligned and their optical paths are the same, so this difference in aperture size does not affect my investigation. Figure 4.17 shows position-velocity diagrams for the [O I] doublet, and for [S III] emission which falls between them on the detector. A tilt appears to be present in the [O I] doublet but, reassuringly, no tilt is present in the [S III] line. Furthermore, Gaussian fitting to pixel rows either side of the 0″position for the [S III] line revealed velocity differences of effectively zero (ie. $\leq0.5\,\mathrm{km\,s^{-1}}$). Given the extreme unlikelihood that instrumental effects could operate in this manner, this data supports the conclusion that the instrument is not introducing spurious contour tilts in my data.

4.4.7.3 Physical Effects Mimicking Rotation

Finally, apart from instrumental error, the only other obvious effect which could produce a contour skew mimicking rotation is asymmetrical interaction with the local environment on either side of the propagating jet, e.g. asymmetrical mass entrainment leading to asymmetrical poloidal velocities. However, such mimicking is unlikely because (apart from the fact that asymmetrical entrainment should also produce enhanced emission at one side of the jet, which is not seen in these spectra) I see the same asymmetry in both the receding and approaching jet lobes where present.

4.4.8 Implications for Theoretical Models

Overall, these observations are in line with the observations of the jet from the T Tauri star DG Tau (Bacciotti et al. 2002). In that case, it was demonstrated that the observed radial velocity differences were in the expected range for magnetically launched 'Disk winds', (Bacciotti et al. 2002, Anderson et al. 2003, Dougados et al. 2004). These values com-

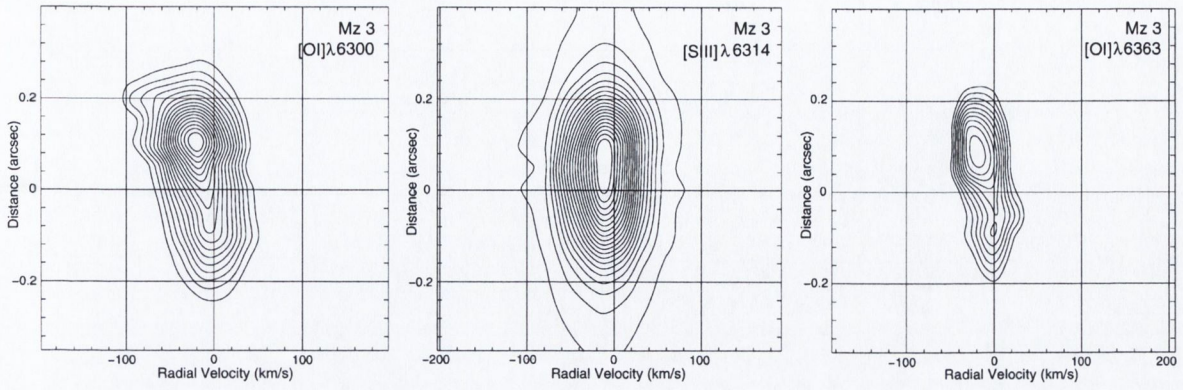

Figure 4.17: *Menzel 3 (Mz 3, or the Ant Nebula) observed with almost the same instrument configuration as that used in my optical survey. Any tilt present in OI emission should be present in each line of the doublet, as is seen here. Meanwhile, no tilt is present in the [S III] emission which falls between them on the detector, thus ruling out the possibility that instrumental effect are introducing spurious contour tilts in my data. Contour floor, ceiling and interval levels (in units of erg cm^{-2} s^{-1} Å^{-1} arcsec^{-2}) are 1.0×10^{-13}, 9.0×10^{-13} and 5.0×10^{-14} for [O I]λ6300; 1.0×10^{-13}, 5.8×10^{-12} and 3.0×10^{-13} for [S III]λ6314; 1.0×10^{-13}, 3.5×10^{-13} and 2.8×10^{-14} for [O I]λ6363.*

pare well with my results, which therefore also support the magneto-centrifugal scenario. Furthermore, the derived toroidal and poloidal velocities (Table 4.4) have the same ratio as theoretical predictions (Vlahakis et al. 2000).

4.4.8.1 Jet Footpoint

As explained in Chapter 2 (Section 2.2.3), I can use my radial velocity measurements, in combination with the values in Table 4.1, to find a range for the radius from the star, in the disk plane, of the jet footpoint (or launch point), $r_{0,obs}$. This was calculated using Equation 2.4 (Anderson et al. 2003), where $M_\star$ is the mass of the star which, where unknown, can be assumed to be 1 $M_\odot$ as a reasonable approximation.

The range for the jet footpoint radius for each target is given in Table 4.4. Values were calculated for a sample of emission lines (i.e. those with very high signal-to-noise, usually [O I]λ6300 and [N II]λ6583 lines), rather than giving an average for each target, since each line traces different levels of radial velocity. In some targets the effects of projection and beam smearing (see Pesenti et al. 2004) appear to be more pronounced. This can be seen from the sharp decrease in radial velocity differences at 0.″05, Table 4.3. In these cases, I have chosen measurements at 0.″1 and 0.″2 from the jet axis as limits of a suitable range for which to calculate the footpoint. Furthermore, it should be noted that

Target	Emission line	$r_{\infty,obs}$ (arcsec)	$r_{\infty,obs}$ (AU)	$\triangle v_{rad}$ (km s^{-1})	$\overline{v_{rad}}$ (km s^{-1})	v_ϕ (km s^{-1})	v_p (km s^{-1})	$r_{0,obs}$ (AU)
TH 28 receding jet	λ6300	0.10	17	12	27	6	155	0.4
	λ6300	0.20	34	16	13	8	75	2.0
	λ6583	0.10	17	14	35	7	202	0.5
	λ6583	0.20	34	25	32	13	184	0.8
TH 28 approaching jet	λ6583	0.10	17	8	65	4	374	0.1
	λ6583	0.15	26	7	62	3	357	0.1
RW Aur receding jet	λ6300	0.10	14	20	102	14	147	0.7
	λ6300	0.20	28	24	94	17	135	1.3
	λ6583	0.05	7	14	111	10	160	0.3
RW Aur approaching jet	λ6583	0.10	14	10	190	7	274	0.2
DG Tau approaching jet	λ6300	0.05	7	15 (14)	188 (72)	12 (11)	250 (91)	0.2 (0.6)
	λ6300	0.15	21	26 (18)	185 (60)	21 (15)	235 (76)	0.5 (1.2)
	λ6583	0.05	7	7	182	6	231	0.1
	λ6583	0.15	21	8	166	7	211	0.3
CW Tau approaching jet	λ6300	0.05	7	15	105	10	160	0.3
	λ6300	0.15	21	12	108	8	165	0.6
	λ6583	0.05	7	12	104	8	159	0.3
	λ6583	0.10	14	26	97	17	148	0.8
HH 30 approaching jet	λ6300	0.05	7	5	31	3	54	0.5
	λ6300	0.15	21	4	29	2	54	0.8

Table 4.4: *The radius from the star in the disk plane of the jet footpoint (or launch point), $r_{0,obs}$, calculated for the optical targets using the method described in Anderson et al. (2003). The TH 28 approaching jet [O I]λ6300 line is not included since the profile of this emission is very wide and did not allow measurement of velocity peaks with Gaussian fitting. In this case the rotational velocities were derived from cross-correlation routines alone, resulting only in velocity difference measurements. Values in brackets relate to the lower velocity component (although this lower velocity calculation was not carried out for the lower velocity component of CW Tau as the radial velocity was zero). The mean radial velocity taken from values equidistant either side of the jet axis, $\overline{v_{rad}}$, is quoted as an absolute value (after heliocentric velocity correction). Since i_{jet} is given with respect to the plane of the sky, I calculate $v_\phi = (\triangle v_{rad}/2)/\cos i$ and $v_p = (\overline{v_{rad}})/\sin i$. The error in v_p increases with decreasing values of i_{jet} so, in the case of HH 30, I use a value from the literature for v_p of 54 km s^{-1} measured at 72 AU along the approaching jet (Burrows et al. 1996).*

values at 0.″1 are less precise than those at 0.″2, when both are present, since increased projection effects close to the jet axis tend to reduce the line of sight averaged v_ϕ, and hence the resulting value of $r_{0,obs}$ (Pesenti et al. 2004). Finally, as an aside, the poloidal velocity asymmetry in the bipolar jet of RW Aur is well known from previous observations (Woitas et al. 2002), and a similar asymmetry was also previously recorded for the TH 28 bipolar jet, (Graham et al. 1988).

It can immediately be seen that the higher velocity [N II] lines tend to trace the base of the jet to a point closer to the star than the intermediate velocity [O I] lines. From the results of these emission lines, it can be seen that in general the higher velocity component appears to be launched from a distance of ~ 0.1 to 0.8 AU from the star along the disk plane in all jet targets. The lower velocity [O I] component for DG Tau appears to trace a wider part of the jet launched from ~ 0.6 to 1.2 AU. These values are in the same range as those estimated for the DG Tau jet of 1.8 AU by Bacciotti et al. (2002), and of 0.3 to 4 AU by Anderson et al. (2003) for the same dataset (where the analysis was carried out on only the lower velocity component of the jet). The results for the other targets also fall into this range determining the footpoint of the jet to be within 0.1 to 2 AU from the star. Furthermore, they consistently show that the jet is launched from a region not less than 0.1 AU from the star on the disk plane, for this velocity resolution. This holds true even for the higher velocity [N II] observations which trace the jet close to the axis.

Given the uncertainties associated with many of the physical parameters (such as stellar mass, inclination angle and distance to the T Tauri system), these calculations represent *estimates* of the jet footpoint and so no error bars are given. Nevertheless, the observational results presented here supports the idea that 'Disk winds' are launched, via the magneto-centrifugal mechanism (e.g. Königl et al. 2000), at footpoint radii within a few AU of the star. It should also be noted that the above calculation strictly gives only the footpoint of the flow surface for which the rotational velocity could be measured, and not the outer radius of the whole ejection region. For example, Takami et al. (2004) report the discovery of a cold and slow wind component emitting in H_2 lines, that surrounds the base of the optical jet from DG Tau. Such a component is probably anchored at larger footpoint radii than the optical component. Thus, the derived footpoint values may be considered as lower limits to the true extent of the launching region. Determination of the most appropriate model, however, requires higher spatial and spectral resolution observations (see Chapter 5).

4.4.8.2 Mass and Angular Momentum Fluxes

As described in Chapter 2 (Section 2.2.3), my observations allow an estimation of the bipolar jet contribution in angular momentum extraction from the jet-disk system.

It should be noted that jet mass flux determinations are naturally heavily dependent on electron density, n_e, and ionisation fraction, x_e. Unfortunately, these parameters are not well determined close to ($< 0\farcs5$) any T Tauri jet source. While the [S II]λ6716/λ6731 flux ratio is an indicator of electron density, figure 5.3 of Osterbrock (1989) illustrates that the [S II] critical density limit (i.e. $2\times10^4\,\mathrm{cm}^{-3}$) corresponds to a [S II] ratio of 0.45 at temperatures of 10^4 K, which is a typical jet temperature. The [S II] ratio is not sensitive to densities above this value, and so only ratios above 0.45 are useful indicators of electron density. Therefore, my values for this ratio (i.e. ranging from $\sim$0.43 to 0.53 depending on jet target) border the sensitivity of the [S II] doublet to electron density levels.

Nevertheless, consider the case of RW Aur. My measured [S II] flux ratio is 0.48 (yielding $n_e = 1.5\times10^4\,\mathrm{cm}^{-3}$) at $0\farcs3$ along the receding jet. This ratio is just within the sensitivity limit. By comparison, for example, values obtained by Dougados et al. (2002), using the diagnostic techniques of Bacciotti et al. (1999), give an upper limit of $n_e \leq 4\times10^3\,\mathrm{cm}^{-3}$ at $0\farcs4$ along the receding jet. Although the latter technique is more accurate, the values relate to a distance further along the jet, for their lower resolution ground-based data. While I will use my own value of n_e, I have yet to carry out a full diagnostic study to determine x_e at $0\farcs3$ along the jet. Meanwhile, Dougados et al. (2002) reported upper limits for x_e of 0.01 and 0.007 at $0\farcs4$ and $0\farcs6$ along the jet respectively. These points represent a scatter in a general trend of decreasing ionisation fraction close to the star. Extrapolating their results gives a value of 0.007 at $0\farcs3$ along the jet.

The case of the RW Aur receding jet provides information on all of the required parameters, allowing greatest accuracy in determination of angular momentum extraction. Other sources have either little diagnostic information (at close proximity to the star) available in the literature, or poor rotation measurements (Table 4.3). It is also unfortunate that the RW Aur approaching jet shows poor measurements of rotation, and a [S II] flux ratio which borders the critical density sensitivity limit. Since jet mass flux is so heavily dependant on the accuracy of electron density and ionisation fraction, the error introduced by approximations can be substantial. The uncertainties resulting from these gaps in information do not justify calculating the contribution of the approaching jet to angular momentum extraction from the RW Aur system. Instead, I choose to calculate the contribution of the receding jet for which diagnostic and kinematic values are of reasonable certainty, and then multiply this value by 2. Although this is not the most desirable approach, considering that asymmetry in T Tauri bipolar jets is well known, it

should nevertheless serve as a good indication of the role that bipolar jets play in the star formation process.

Tables 4.5 and 4.6 list measured and derived physical parameters for the RW Aur receding jet and the RW Aur jet-disk system respectively. The [O I]λ6300 emission line measurements were chosen for the calculation as this line best represents typical jet parameters in terms of FWHM, radial velocity, and radial velocity differences. I have taken $r_{0,co} = 0.06$ AU, calculated from the rotation period of RW Aur A (the optically brightest component of this triplet system) of 5.5 days (Petrov et al. 2001), see Section 2.2.3. This value for the corotation radius gives $v_{K,co} = 122\,\mathrm{km\,s^{-1}}$.

My estimates indicate that the jet could in fact extract most if not all of the angular momentum from the system (Table 4.5), thus allowing the T Tauri star to rotate more slowly and further accrete the material of its circumstellar disk. The calculated jet mass and angular momentum fluxes, $\dot{M}_{jet}$ and $\dot{L}_{jet}$ (Table 4.5), compare well with the disk mass and angular momentum fluxes, $\dot{M}_{disk,co}$ and $\dot{L}_{disk}$ (Table 4.6), in that they provide the expected ratios of mass ejection to accretion (i.e. 7%) and disk-to-jet angular momentum transfer (i.e. 81%). Mass accretion rates in the literature are reported to be between 1 and 10% (e.g. Hartigan et al. 1995), and my results are in very good agreement with similar calculations by Woitas et al. (2005) who report jet angular momentum extraction of between 66% and 82%.

While these results provide good indications of the potential role bipolar jets play in star formation, they still represent rough estimations. Errors introduced by inaccuracy in diagnostic parameters may be considerable (leading to variations in angular momentum transfer in the region of $\pm\,50\%$ or more), and so I find it meaningless to give error estimations for the calculations. This highlights the importance of a diagnostic study on the jet close to the launch region. Using the diagnostic code developed by Bacciotti et al. (1999), I intend to use my optical data to find more accurate values of electron density and ionisation fraction, thus providing for the first time detailed diagnostic information close to the jet source (see Chapter 6). Regardless, my calculations succeed in demonstrating *observationally* that it is very reasonable to assume jets can indeed play a significant role in angular momentum transport.

4.5 Conclusions

HST/STIS was used to observe the base of eight jet targets, each from one of six T Tauri stars (i.e. the bi-polar jets from TH 28 and RW Aur, and the approaching jet from LkHα 321, DG Tau, CW Tau and HH 30). All except LkHα 321 showed distinct and sys-

Target	n_e ($\mathrm{km\,s^{-1}}$)	x_e	$v_\mathrm{p}{}^a$ ($\mathrm{cm^{-3}}$)	$FWHM^b$ (arcsec)	$r_{0,obs}{}^a$ (AU)	$\dot{M}_{jet}$ ($\mathrm{M_\odot\,yr^{-1}}$)	$\dot{L}_{jet}$ ($\mathrm{M_\odot\,yr^{-1}\,AU\,km\,s^{-1}}$)
RW Aur receding jet	1.5×10^4	0.007	135	0.145	1.3	5.6×10^{-8}	1.9×10^{-5}

Table 4.5: *Measured derived physical quantites for the RW Aur receding jet at 0.″3 from the source.* [a] *For the [O I]λ6300 emission at $r_{0,obs} = 0.''20$ (see Table 4.3);* [b] *Measured for the [O I]λ6300 emission.*

Target	$v_{K,obs}$ ($\mathrm{km\,s^{-1}}$)	$\dot{M}_{disk,co}{}^a$ ($\mathrm{M_\odot\,yr^{-1}}$)	$\dot{M}_{disk,obs}$ ($\mathrm{M_\odot\,yr^{-1}}$)	$\dot{L}_{disk}$ ($\mathrm{M_\odot\,yr^{-1}\,AU\,km\,s^{-1}}$)	$\dot{M}_{jet}/\dot{M}_{acc}{}^b$	$\dot{L}_{jet}/\dot{L}_{disk}{}^b$
RW Aur disk	26	1.6×10^{-6}	1.7×10^{-6}	4.6×10^{-5}	0.07	0.81

Table 4.6: *Measured and derived physical quantites for the RW Aur jet-disk system.* [a] *Hartigan et al. (1995);* [b] *The ratio considers the contribution of the bipolar jet, i.e. by multiplying the contribution of the receding jet by 2 (see text). (Recall that $\dot{M}_{disk,co}$ is usually referred to as $\dot{M}_{acc}$ in the literature.)*

tematic radial velocity asymmetries in opposing positions with respect to the jet axis, within 100 AU from the source. Radial velocity differences were found to be on the order of 10 to 25 (±5) $\mathrm{km\,s^{-1}}$. I interpret these radial velocity asymmetries as rotation signatures in the region close to the star where the jet has been collimated but has not yet manifestly interacted with the environment. For the bipolar jets from TH 28 and RW Aur, the velocity differences have the same direction in both lobes, i.e. opposite helicity in opposing jets. The sense of rotation of the jets, looking down the approaching jet towards the star, is clockwise for all targets except RW Aur, for which it is anticlockwise.

My findings are reinforced in a number of ways: the radial velocity differences in the DG Tau jet are of the same magnitude and direction as those previously measured of 5 to 10 $\mathrm{km\,s^{-1}}$ (Bacciotti et al. 2002), which was shown to be in agreement with the predictions of MHD 'Disk wind' models (Bacciotti et al. 2002, Anderson et al. 2003, Dougados et al. 2004, Pesenti et al. 2004); my findings are in line with similar research on the RW Aur jet (Woitas et al. 2005) which yields rotational velocities of 10 to 20 $\mathrm{km\,s^{-1}}$ with the same sense of rotation; and finally, my results lead to estimates for the distance of the jet footpoint from the central axis of typically ~0.1 to 0.8 AU for the higher velocity gas in the jet and ~0.6 to 1.2 AU for the lower velocity material, i.e. values which are consistent with models of magneto-centrifugal launching (Anderson et al. 2003).

Finally, my estimates of jet mass and angular momentum fluxes, based on observations

of radial velocity differences, indicate that the jet could in fact extract most, if not all, of the angular momentum from the system. This demonstrates *observationally* that it is very reasonable to assume jets can indeed play a significant role in angular momentum transport, allowing the T Tauri star to rotate more slowly and further accrete the material of its circumstellar disk.

5

YSO Jet Rotation in the Near Ultraviolet

This chapter examines YSO jet generation through a survey of pre-main sequence jets, using *HST* spectroscopic observations at NUV wavelengths.

5.1 Introduction

Although the results of Chapter 4 are encouraging, it is evident that I am only marginally resolving the effects of rotation because of the limiting resolution (spatially and spectrally) of *HST*/STIS at optical wavelengths. However, emission from protostellar outflows is dominated by lines in the ultraviolet. In particular, shock models (Hartigan, Raymond & Hartmann 1987) and observations (Hartigan et al. 1999) show that low excitation Mg II doublet emission at 2796 Å and 2803 Å is stronger in protostellar outflows than traditionally observed optical lines such as the [O I]$\lambda\lambda$6300,6363 doublet. Furthermore, observing with *HST*/STIS at NUV wavelengths affords double the spatial resolution of the optical region, and so holds the potential for me to extend my study to the currently unresolved higher velocity jet core. Also, since the accuracy of velocity determinations are typically a fifth of the velocity sampling, the NUV holds the potential to achieve errors as low as $2\,\mathrm{km\,s^{-1}}$, compared to $5\,\mathrm{km\,s^{-1}}$ in the optical region.

Therefore, based on the findings of Chapter 4, *HST*/STIS observations were planned

to examine the same targets at NUV wavelengths. Unfortunately, due to the failure of a *HST*/STIS power supply on August 3rd 2004, only three of five scheduled observations were conducted. On the other hand, there now exists NUV data for these three targets.

In this chapter, I present a velocity analysis for my NUV dataset of three jet targets namely, both lobes of the bipolar jet from TH 28 and the approaching jet from DG Tau.

5.2 Observations

Spectroscopic observations were made in the NUV wavelength region at the base of three T Tauri star jets. As with the optical wavelength observations detailed in Section 4.2, the observing mode used involved centering the *HST*/STIS slit on the T Tauri star, and then offsetting the slit to a position perpendicular to the jet axis at a fraction of an arcsecond from the source, Figure 4.1.

HST/STIS NUV observations (proposal ID 9807) were conducted of the jets from T Tauri stars TH 28 and DG Tau (Table 4.1). The slit offset of 0.″3 represented a deprojected distance of 52 AU along the TH 28 jet and 68 AU along the DG Tau jet. The NUV Multi-Anode Microchannel Array (MAMA) detector was used with the E230M echelle grating, centred on 2707 Å, and a long slit of aperture $6\times0.2\,\mathrm{arcsec}^2$ (to ensure the full width of the jet was observed). Spectral sampling was $0.045\,\text{Å}^{-1}$, corresponding to a radial velocity of ~5 to $10\,\mathrm{km\,s^{-1}}$, and spatial sampling was $0.''029\,\mathrm{pixel^{-1}}$. Two long exposures (co-added to improve signal-to-noise) of ~2500 s were made of each lobe of the TH 28 bipolar jet on June 18 2004, and the approaching jet from DG Tau on December 1 2003.

Although the data were largely processed through the standard *HST* pipeline, the combination of an echelle grating with a long slit meant wavelength calibration was not conducted as part of the routine pipeline procedure (due to possible overlap of spectral orders arising from use of this instrument configuration), and so wavelength calibration was subsequently carried out using standard IRAF routines.

5.3 Results

All three NUV jet targets were found to be strong emitters in both lines of the Mg II doublet (i.e. at vacuum wavelengths of 2796.352 Å and 2803.531 Å). Their profiles are broad, extending over some $200\,\mathrm{km\,s^{-1}}$. Spatial extention is represented by FWHM values in the range of 0.″12 to 0.″20 for both jets from TH 28 (as opposed to 0.″27 and 0.″41 for [O I] and [S II] receding jet lines respectively), and of 0.″12 for the approaching jet from DG Tau (as opposed to 0.″15 and 0.″20 for [O I] and [S II] lines respectively). This shows

that the high excitation NUV lines preferentially originate in the axial region of the jet, consistent with the expectations of MHD models of the jet base where layers closer to the axis are predicted to be more excited than those further away.

Once wavelength calibration was conducted, the data analysis was carried out in the same way as for the optical survey (detailed in Section 4.3). Briefly, the peak of each emission line was centred on the nominal zero arcsecond position on the detector, since the peak is assumed to correspond to the jet axis. Radial velocities were then determined for the peak intensity of each pixel row parallel to the jet axis, using both a Gaussian fitting and cross-correlation technique to ensure accuracy. Systematic differences in radial velocities equidistant either side of the jet axis were interpreted as jet rotation.

5.3.1 Qualitative Indications of Rotation

Figures 5.1, 5.2 and 5.3 show position-velocity contour plots for the NUV Mg II $\lambda\lambda$2796,2803 doublet for each of the three jet targets observed (with corresponding contour levels given in Table 5.1). The positive direction of the y-axis corresponds to the slit direction in Figure 4.2, and all radial velocities are systemic. As previously described, if rotation is present radial velocities will be lower on one side of the jet axis than on the other, and will be evidenced by a skew in the contours of the transverse position-velocity diagram. While a position-velocity contour tilt can generally be recognised at optical wavelengths (Section 4.3.1), it is not so apparent in the NUV range. It is likely that the broad profile shape in the dispersion direction combined with the relatively narrow spatial FWHM may detract from the clarity of any tilt. The existence of an absorption feature for the NUV permitted transitions may also draw from the clarity of contour trends. Nevertheless, quantitative measurements yielded positive results.

5.3.2 Quantitative Analysis

Having recentred the emission peak on the nominal zero arcsecond position of the detector (as described in Section 4.3.2), radial velocities across the jet were determined using both the Gaussian fitting and cross-correlation techniques. The absorption feature, highlighted by the position-velocity contour plots, dominates the emission in the case of TH 28 more so than in the case of DG Tau. This is more apparent when emission is binned for plotting in one dimension (see Figure 5.4 with corresponding Mg II integrated fluxes and Mg II flux ratios given in Table 5.2). An absorption dip is located at low blueshifted velocities for all three targets. Radial velocities were found to be: $-23\,\mathrm{km\,s^{-1}}$ in the TH 28 receding jet; $-15\,\mathrm{km\,s^{-1}}$ in the TH 28 approaching jet; and $-23\,\mathrm{km\,s^{-1}}$ in the DG Tau approaching jet.

Note that these velocities heliocentric rather than systemic, since it is unclear whether or not the dip originates in part of the T Tauri system.

Single Gaussian fitting to the overall peak excluding the absorption region was carried out, and the results were compared to those from the cross-correlation routine, which were independent of the shape of the profile. There was good agreement in the results, although cross-correlation produced more consistent values in the case of TH 28 since the emission profile was significantly interrupted by absorption, rendering Gaussian fitting less accurate. Conversely, single Gaussian fitting proved more accurate in the case of DG Tau since the absorption features in the extreme wings of the profile, and cross-correlation is more sensitive to noise further from the jet axis where the flux diminishes. Nevertheless, there was good agreement between the two methods.

From this radial velocity analysis, a transverse radial velocity profile at the base of each jet was obtained, Figure 5.5. (Note that the measured absorption velocities quoted above are heliocentric, whereas the zeropoint of the radial velocity axis in the jet emission profiles is systemic.) The position angle, derived from Figure 4.2, is given in the upper corners of each plot. The asymmetric velocity trend, not visible in the contour diagrams, is now evident in these profiles giving a clear indication of rotation. The higher spatial resolution of the NUV observations yields a more detailed radial velocity profile than the optical dataset, showing how radial velocity varies across the jet including the region close to the high velocity axial core (i.e. 0.″029). Profiles from the two datasets are plotted on the same axes to illustrate how well they fit together, Figure 5.6. As with the optical dataset, plots reveal that the on-axis jet material is travelling fastest while the borders of the jet are travelling slower. The result is a v-shaped profile, but these profiles are not symmetrical. Velocities on one side of the axis are lower than on the other.

Differences in radial velocities at positions equidistant on either side of the jet axis were then determined. Table 5.3 gives results for individual emission lines in each jet lobe, and shows that there is consistent evidence of radial velocity differences across all three jet targets of up to $17\,\mathrm{km\,s^{-1}}$. Given sufficient signal-to-noise, it is possible to routinely measure radial velocity differences to one fifth of the velocity sampling, giving an accuracy of $\pm 2\,\mathrm{km\,s^{-1}}$ in the NUV. However, accuracy in determining profile peaks in the NUV is reduced by the broad line profiles, and additional uncertainties are introduced by the absorption features. Therefore, I prefer to give the conservative error estimate of $\pm 5\,\mathrm{km\,s^{-1}}$ for my NUV results. Meaningful analysis of much two fainter NUV emission peaks evident in these spectra was not possible. One was identified as the combined emission lines of C II] $\lambda\lambda$2324,2325,2326,2327,2328 (see Table 5.2 for comparative fluxes) travelling at $180\,\mathrm{km\,s^{-1}}$. The other appears to be [O II] λ2470 , for the same velocity.

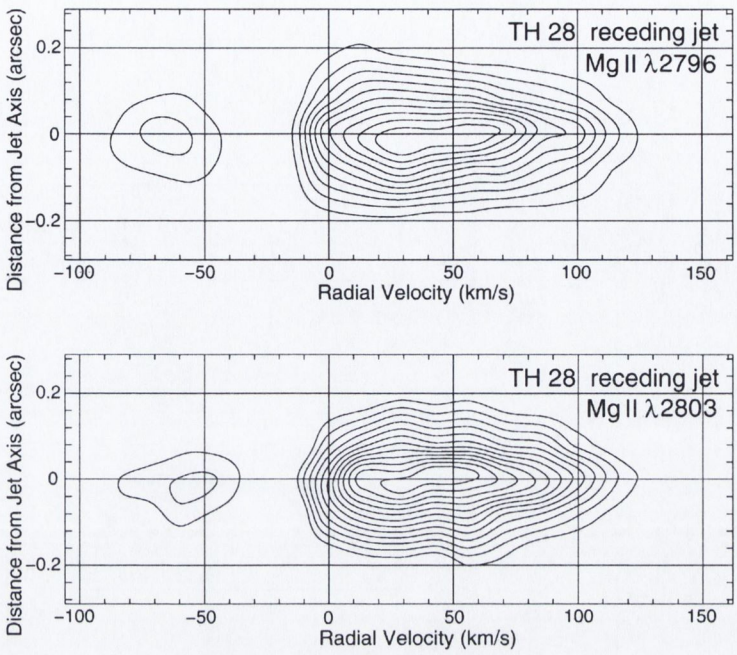

Figure 5.1: *Position-velocity diagrams of NUV emission lines for the TH 28 receding jet. Plots are corrected for the systemic velocity of TH 28. Contour values for each panel in units of erg cm^{-2}sec^{-1} Å^{-1} arcsec^{-2} are listed in Table 5.1.*

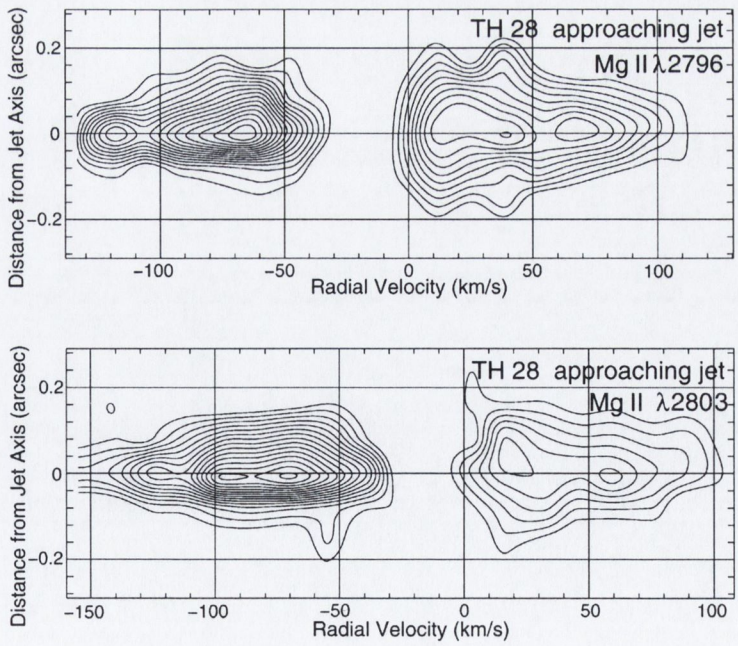

Figure 5.2: *Same as Figure 5.1 but for the approaching jet of TH 28.*

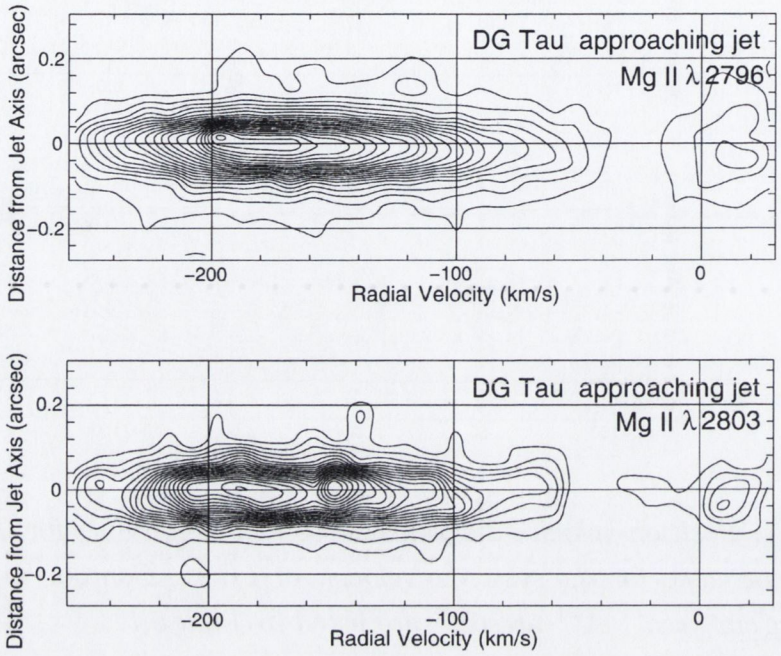

Figure 5.3: *Same as Figure 5.1 but for the approaching jet of DG Tau.*

Target	Emission line	Contour Floor	Contour Ceiling	Contour Interval
TH 28 receding jet	Mg II λ2796	2.0×10^{-13}	2.0×10^{-12}	1.3×10^{-13}
	Mg II λ2803	1.5×10^{-13}	9.0×10^{-13}	5.4×10^{-14}
TH 28 approaching jet	Mg II λ2796	1.0×10^{-13}	3.9×10^{-13}	2.1×10^{-14}
	Mg II λ2803	1.0×10^{-13}	5.2×10^{-13}	3.0×10^{-14}
DG Tau approaching jet	Mg II λ2796	1.0×10^{-13}	2.1×10^{-12}	1.0×10^{-13}
	Mg II λ2803	1.0×10^{-13}	1.2×10^{-12}	6.0×10^{-14}

Table 5.1: *Linear contour intervals relating to position-velocity plots, Figures 5.2 to 5.3, in units of erg cm^{-2} s^{-1} Å^{-1} arcsec^{-2}.*

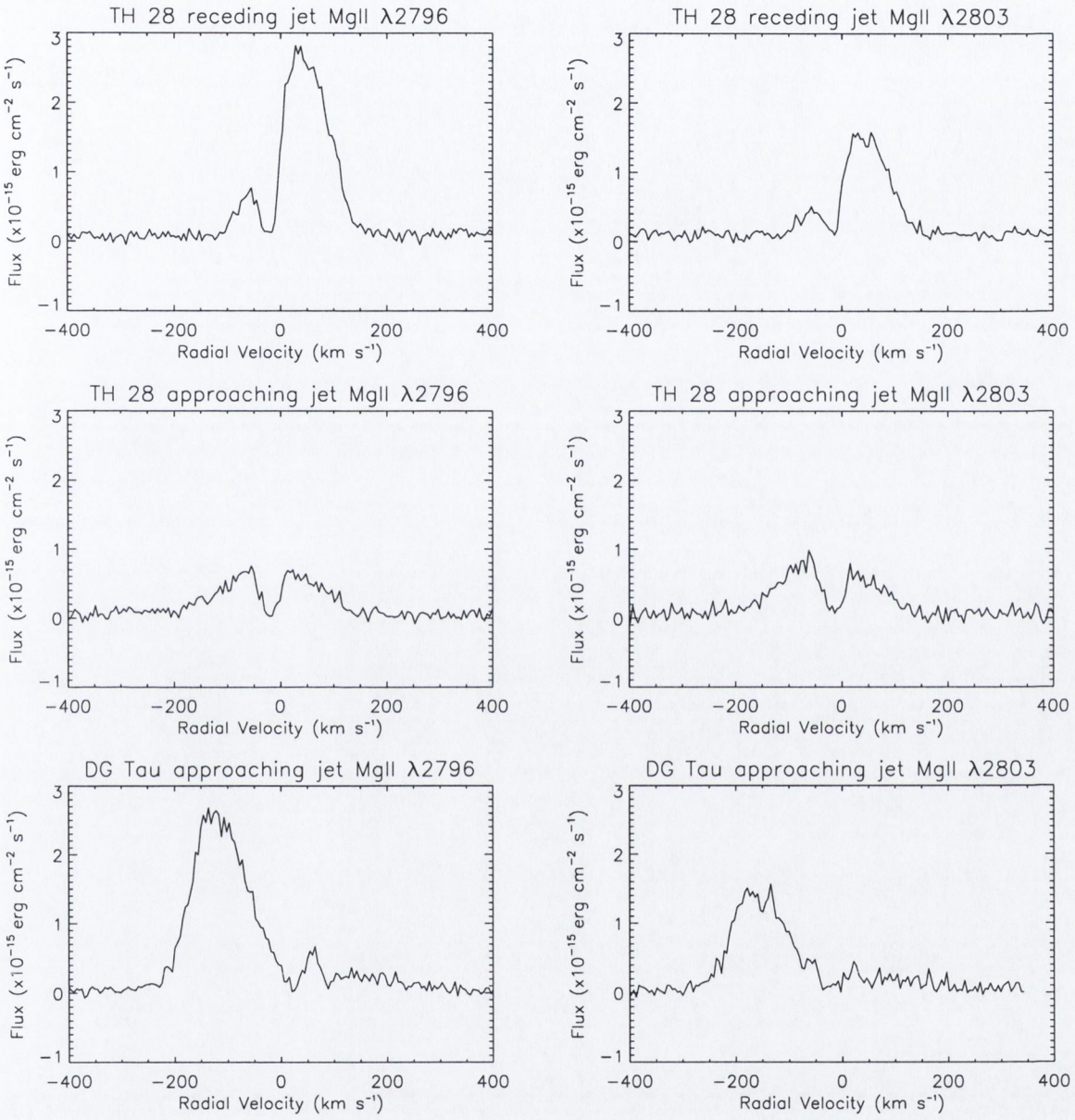

Figure 5.4: *Flux profiles of NUV emission lines, obtained by binning pixel rows over the entire jet width. The absorption feature is located at slightly blueshifted velocity for all three targets, (i.e.* $-23\,\mathrm{km\,s^{-1}}$ *in the TH 28 receding jet,* $-15\,\mathrm{km\,s^{-1}}$ *in the TH 28 approaching jet and* $-23\,\mathrm{km\,s^{-1}}$ *in the DG Tau approaching jet). Note that the measured absorption velocities quoted are heliocentric, whereas the zeropoint for the radial velocity axes above is the systemic velocity. Integrated fluxes are given in Table 5.2.*

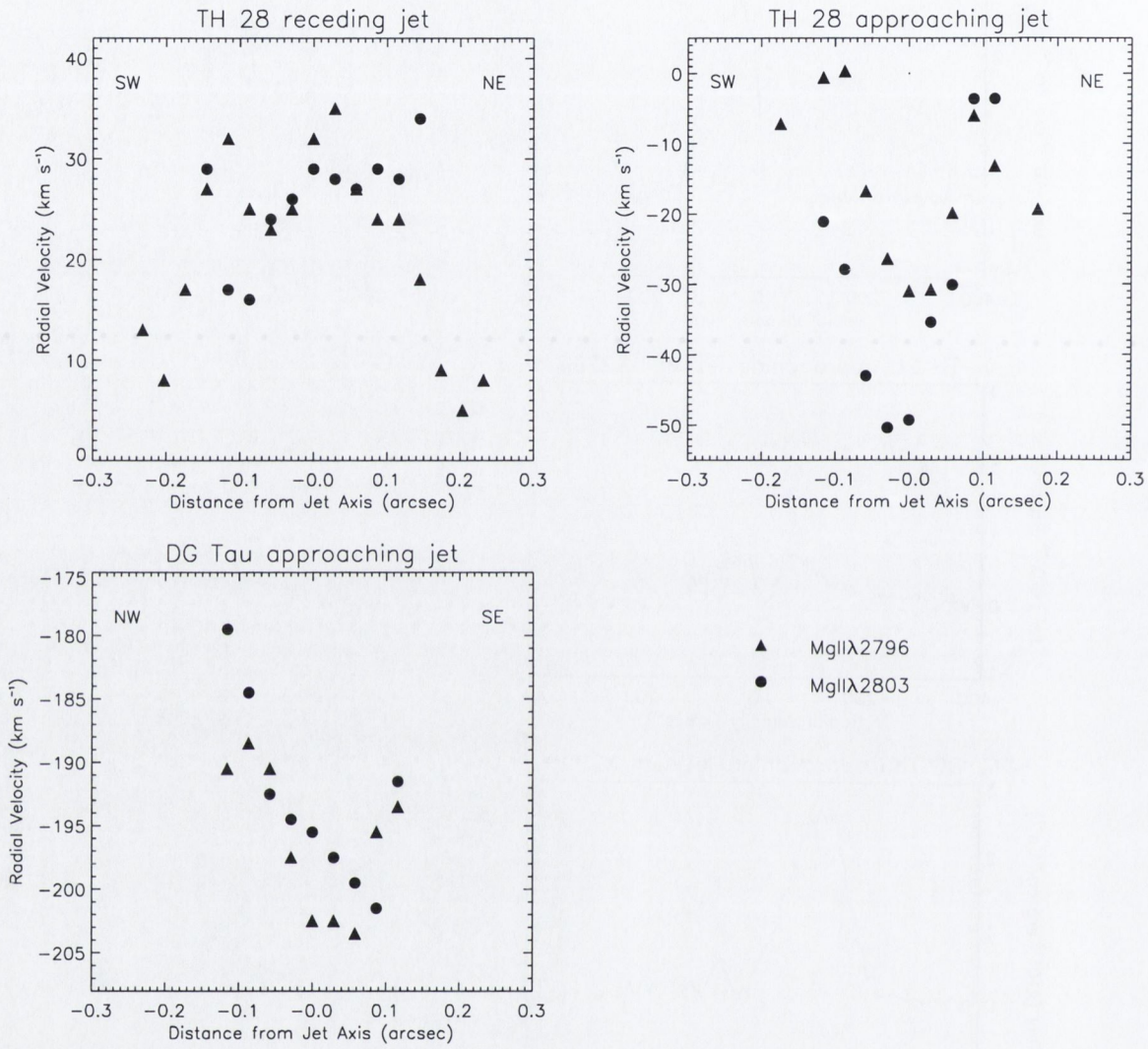

Figure 5.5: *Radial velocity profile across the jet for the NUV Mg II doublet of both the receding and approaching jet from TH 28, and the approaching jet from DG Tau. Profile asymmetries highlight the presence of jet rotation. All radial velocities are systemic. The profile for the TH 28 approaching jet should be considered an indication only. In this case, Gaussian fitting proved very difficult and so an accurate profile could not be constructed. Meanwhile, the radial velocity differences for this target were obtained by relying solely on a cross-correlation routine, as described in Section 5.3.2.*

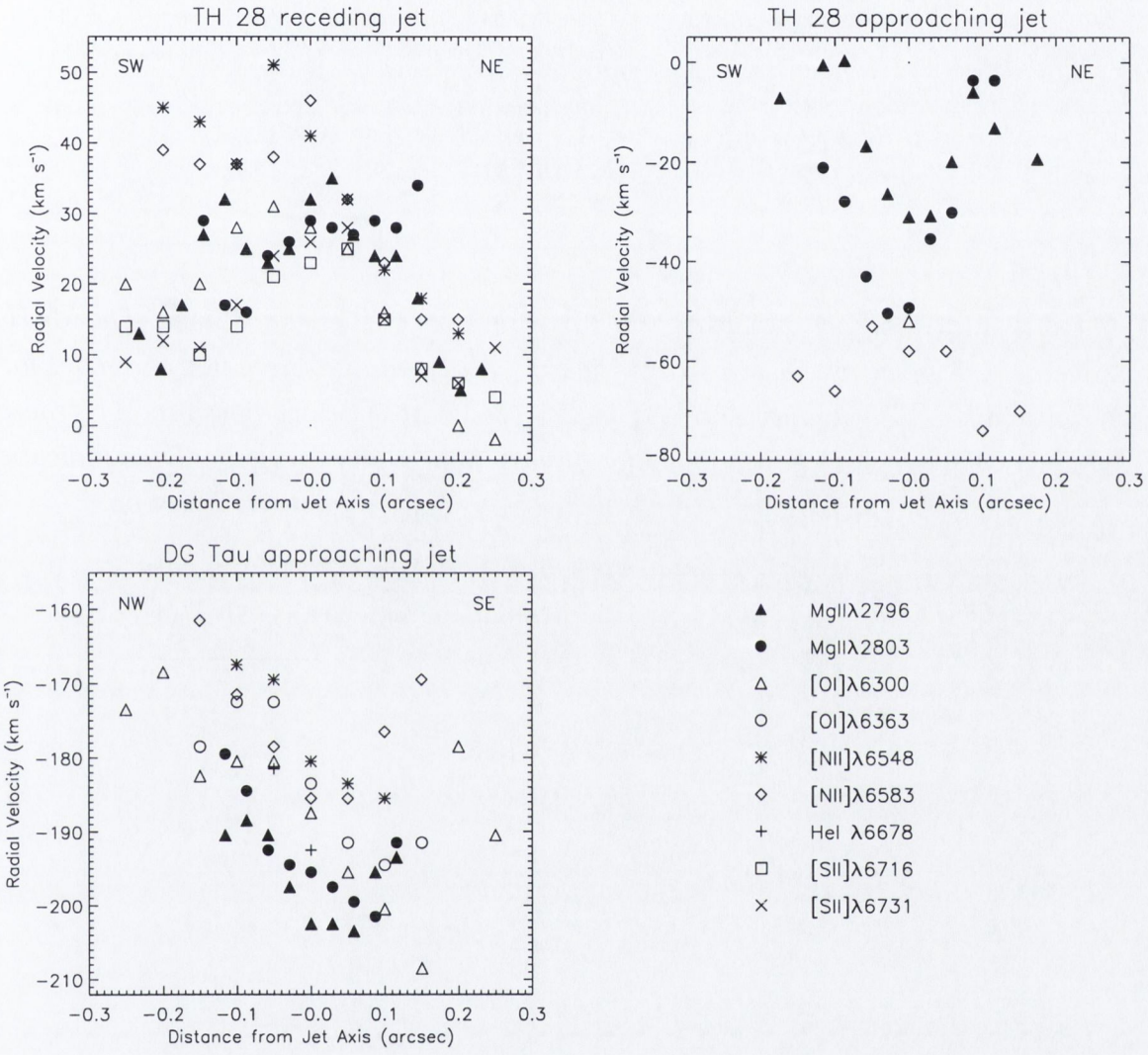

Figure 5.6: *Same as Figure 5.5 but with the optical datasets (Figures 4.13 and 4.14) overlaid on the NUV dataset, to illustrate how radial velocity changes with distance from the jet axis and how the results for the two wavelength regions compare.*

Target	Emission line	Flux ($erg\,s^{-1}\,cm^{-2}$)	Flux Ratio λ2796:λ2803
TH 28 receding jet	Mg II λ2796	3.2×10^{13}	...
	Mg II λ2803	1.9×10^{13}	1.7 : 1
	C II] λ2326	8.7×10^{16}	...
	[O II] λ2470	4.2×10^{16}	...
TH 28 approaching jet	Mg II λ2796	1.3×10^{13}	...
	Mg II λ2803	1.4×10^{13}	0.9 : 1
	C II] λ2326	2.0×10^{16}	...
	[O II] λ2470	...	...
DG Tau approaching jet	Mg II λ2796	3.0×10^{13}	...
	Mg II λ2803	1.8×10^{13}	1.6 : 1
	C II] λ2326	2.1×10^{15}	...
	[O II] λ2470	5.6×10^{16}	...

Table 5.2: *Flux measurements and flux ratios for NUV emission lines. The Mg II doublet integrated fluxes are illustrated in Figure 5.4. Flux values were not corrected for extinction. Also, no compensation was made for the absorption dip since the true emission profile shape is not known. Therefore, these values are provided only as indications. For the TH 28 approaching jet, the [O II] emission was too faint for detection.*

Target	Distance from jet axis (arcsec)	Δv_{rad} for Mg II λ2796 (km s^{-1})	Δv_{rad} for Mg II λ2804 (km s^{-1})
TH 28 receding jet	0.029	0	1
	0.058	-3	-3
	0.087	1	-8
	0.116	7	-3
	0.145	9	-4
	0.174	7	...
	0.203	6	...
	0.232	5	...
TH 28 approaching jet	0.029	0	-1
	0.058	2	-5
	0.087	0	11
	0.116	1	...
	0.145	5	...
	0.174	9	...
DG Tau approaching jet	0.029	6	3
	0.058	12	8
	0.087	7	17
	0.116	4	12

Table 5.3: *Radial velocity differences, Δv_{rad}, between one side of the jet axis and the other, measured using both single Gaussian fitting and a cross-correlation technique. Where dots appear in the table, the emission was either shifted off the detector, or was too faint to decipher. The accuracy reached with the data analysis was approximately $\pm 5\,km\ s^{-1}$.*

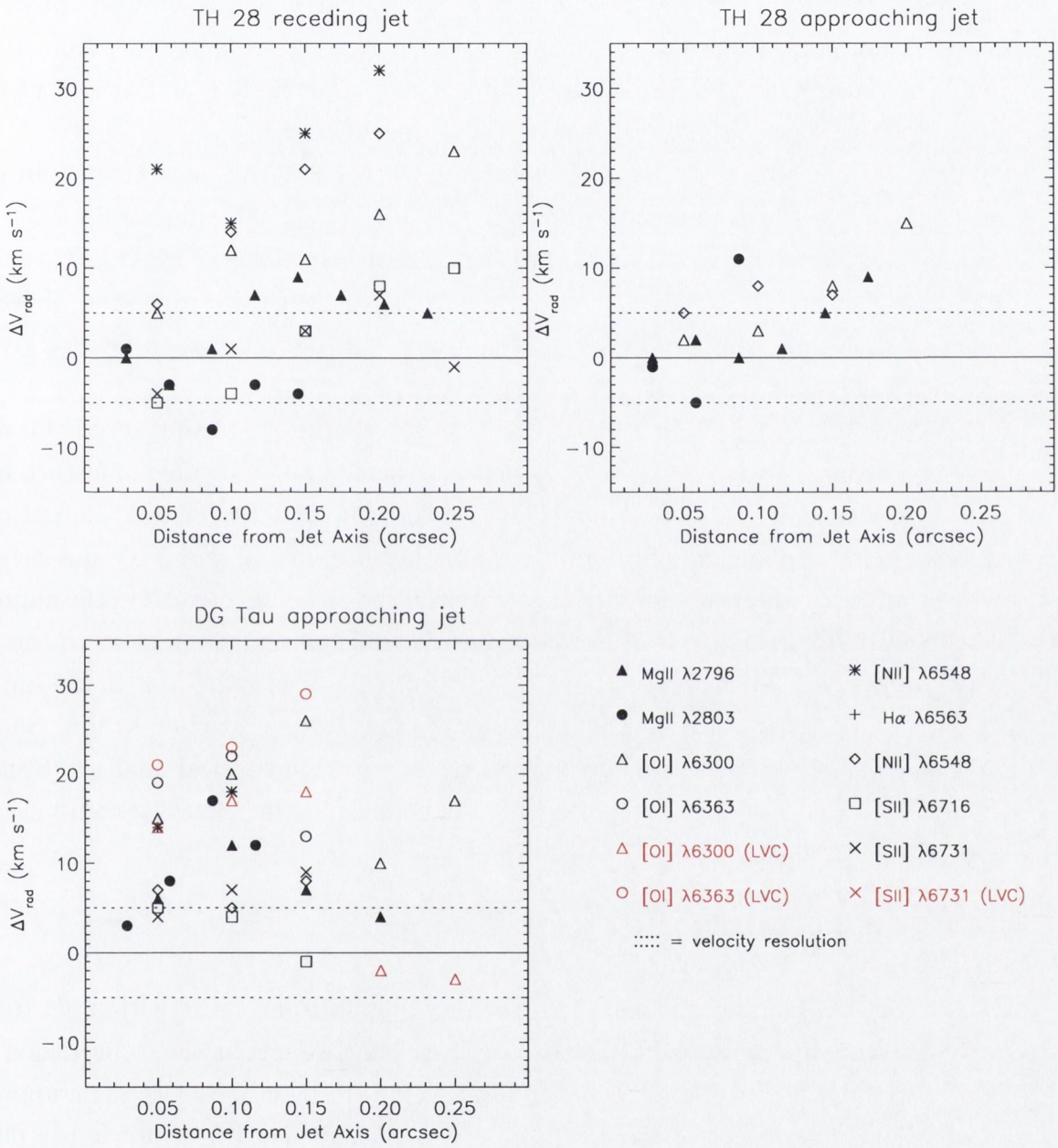

Figure 5.7: *Radial velocity differences, Δv_{rad}, as a function of distance from the jet axis. All targets show positive radial velocity differences. The NUV results are overlaid on the optical results for comparison. (The red points in the optical results represent the lower velocity component of the emission line in cases where double Gaussian fitting was necessary.)*

5.4 Discussion

The results in Table 5.3 show clear differences in radial velocities between either side of the jet axis for all three jet targets observed. Assuming that emission from the jet is axially symmetric, I interpret these radial velocity differences as indications of rotation within the jet close to the source where the jet is launched.

The first point to note about the results in Table 5.3 is the inconsistency in rotation direction within the doublets of TH 28, (i.e. the Mg II λ2803 emission appears to have mainly negative values, inconsistent with the positive values for the Mg II λ2796 emission). However, all negative values fall inside the error bars with the exception of $-8\,\mathrm{km\,s^{-1}}$ which possibly has additional error contribution from the absorption feature given that all other results are consistent.

The second point to note is the drop in Δv_{rad} values close to the jet axis for all three targets. For both jet lobes of TH 28, it appears there is no detectable difference in radial velocities within 0.″1 of the jet axis. This trend can also be seen in the optical data for both lobes at distances of 0.″05 (Table 4.3). In both optical and NUV datasets, radial velocity differences appear closer to the jet axis in the receding jet than in the approaching jet. Meanwhile, a similar drop in radial velocity differences is seen close to the jet axis of DG Tau in the NUV dataset from 0.″058 to 0.″029. This fall is not borne out by the optical results, but optical measurements were only possible as close as 0.″5. Such lower rotational velocities close to the axis were also noted in the optical analysis (Section 4.4) and outlined as possibly due to projection and beam smearing effects (Pesenti et al. 2004; Dougados et al. 2004).

5.4.1 TH 28

For the Mg II λ2796 line, the values for the receding jet from TH 28 within 0.″1 to 0.″2 rise to $9\,\mathrm{km\,s^{-1}}$, comparable to but somewhat lower than values in the same region for the [N II]λ6583 and [O I]λ6300 emission of 10 to $24\,\mathrm{km\,s^{-1}}$ (Section 4.4.1). The approaching jet of TH 28 gives values of up to $9\,\mathrm{km\,s^{-1}}$, in good agreement with previously published optical values of up to $8\,\mathrm{km\,s^{-1}}$ within 0.″15 of the jet axis. However, the results for the Mg II λ2803 line of the bipolar jet are mainly within the error bars of $5\,\mathrm{km\,s^{-1}}$ about zero. Overall, the Mg II λ2796 line indicates that both lobes of the TH 28 bipolar jet are rotating in the same direction, i.e. clockwise looking down the approaching jet towards the star (Figure 4.2), in agreement with the results from the optical dataset (Section 4.4.1).

5.4.2 DG Tau

For the approaching jet of DG Tau, both lines of the Mg II doublet have high signal to noise and are in agreement showing radial velocity differences ranging from 3 to 17 km s^{-1} within 0.″12 of the jet axis. This is in line with, although somewhat lower than, the optical values which lie mainly in the range of 10 to 27 km s^{-1} within 0.″15 of the jet axis (Section 4.4.4). The sense of rotation was found to be clockwise looking down the approaching jet towards the star (Figure 4.2), and in agreement with the results from the optical dataset (Section 4.4.4). Furthermore, the velocity differences are of the same magnitude and direction as those reported by Bacciotti et al. (2002), where values of 5 to 10 km s^{-1} were measured with the *HST*/STIS slit placed *parallel* to the DG Tau approaching jet.

5.4.3 Mg II Absorption

The Mg II resonance doublet is the strongest NUV feature in the spectrum of the T Tauri star itself and, being a permitted resonance transition, is very sensitive to cool gas absorption. Its broad emission profile has been shown to include narrow central absorption and wide blueshifted absorption (e.g. Calvet 1985). The central absorption can be produced by self-absorption or by the ISM (Basri & Linsky 1979), while the blueshifted dip has been attributed to absorption by a cool outflow (Calvet 1997). Indeed, all 8 T Tauri stars in a recent survey by Ardila et al. (2002) show both absorption features. The latter paper assumes all the Mg II emission originates in magnetospheric accretion; it shows that the central dip is too broad to originate in the ISM; and it concurs with Calvet (1997) in that the blueshifted dip originates in the outflow.

On the other hand, my spectra show that the jet is also *emitting* in Mg II, similar to spectra from HH 47 (Hartigan et al. 1999) which were successfully modelled as arising from composite shocks. It then becomes apparent that the spectra of Ardila et al. (2002) include Mg II emission from both magnetospheric accretion *and* the jet, since they integrate spectra over an aperture of diameter 2″ centred on the star (while my slit is of width 0.″2 and positioned 0.″3 from the star along the jet). A comparison of the two datasets in terms of the velocity and intensity of the blueshifted emission from DG Tau (i.e. comparing their Figure 5 with my Figure 5.4) shows this to be the case.

The blueshifted absorption in the stellar spectra of Ardila et al. (2002) is clearly caused by a low velocity wind, a conclusion drawn from the fact that the profile is very broad and asymmetric in shape. My jet observations also show dips in the profiles, which are blueshifted to $\sim -20 \pm 5$ km s^{-1} but have a narrower FWHM (~ 40 km s^{-1}) and are not

significantly asymmetric.

Typical interstellar Mg II absorption velocities are $\sim$-10 to -30 km s^{-1} with FWHM values of $\sim$2 to 4 km s^{-1} (e.g. Dring et al. 1997). The fact that each of my spectra shows a dip which coincides with typical interstellar absorption velocities suggests that the dip originates in interstellar cloud material. This conclusion is reinforced by the fact that the dip is blueshifted in all the observed targets, *including* the receding jet. In other words, the absorption cannot be caused by a low velocity wind component of the jet, otherwise the receding jet would instead show red-shifted absorption. The relatively broad FWHM, however, requires explanation.

Thermal broadening cannot account for the large FWHM as it yields an interstellar cloud temperature of $\sim 10^6$ K, which is too high to allow the presence of Mg II. If formed collisionally at low densities, the Mg II ion has a maximum population at 13 000 K (Arnaud & Raymond 1992). A possible explanation for the large FWHM is that several interstellar absorption components are present. This scenario is plausible given the large distance to our targets of about 150 pc. Relatively similar FWHM values have been recognised in previous studies and reasonably attributed to the contribution of more than one interstellar cloud. For example, similar Mg II interstellar absorption features (FWHM $\sim$ 20 km s^{-1}) are present in high resolution *HST*/STIS spectra of main sequence F stars (Böhm-Vitense et al. 2001). The latter paper remarks that, for some sources, two interstellar lines seem to merge when two clouds have almost the same velocity, while for other sources the Mg II emission line has a very broad central absorption which is too broad to be interstellar unless there are at least three strong components contributing.

The broad FWHM could perhaps be more readily explained by an expanding shell around the T Tauri system. In contrast to attributing the absorption to a cooler outflow wind, an expanding shell would be observed as a blue-shifted dip regardless of whether the observed jet is approaching or receding. This explanation would also account for the broad FWHM without having to envoke the combined absorption contribution of several interstellar clouds in the line of sight to all targets.

Another possible contributor to the profile dip is self-absorption, whereby absorption may originate in the jet itself. The gas will then be optically thick. The λ2796:λ2803 ratio is expected to be 2:1 if emitted by an optically thin gas (due to equal transition probabilities but different statistical weights of the two energy levels). Since absorption occurs in the same ratio as emission, and saturation of the λ2796 line occurs before the λ2803 line, self-absorption begins to affect the flux ratio of the Mg II doublet. As the material approaches optical thickness, so the flux ratio approaches 1:1. The flux ratios (Table 5.2) for the TH 28 receding jet and the DG Tau approaching jet demonstrate the gas

to be optically thin. The dip is therefore not likely to include a self-absorption component. On the other hand, the TH 28 approaching jet is evidently optically thick, and the FWHM of the dip is slightly larger here than for the other targets. Therefore, in this case, the dip is very likely to incorporate a self-absorption component. Besides, this jet is known to be heavily embedded in reflection nebulosity (Graham & Heyer 1998).

FELs are so called because the probability of radiative transition is low. They may be collisionally excited (e.g. via jet shocks) and then radiatively de-excited, provided the medium is of sufficiently low density such that collisional de-excitation does not dominate. Following this, the emitted photons are highly unlikely to be re-absorbed either through self-absorption or ISM absorption. Hence absorption dips do not appear in FEL profiles, and so the optical spectra (Chapter 4), which mainly comprise FELs, do not exhibit absorption features. Although it is probable that the Hα emission incorporates absorption similar to Mg II, the Hα line could not be analysed because there are too many possible contributions to its shape, e.g. reflection nebula emission, self-absorption and/or interstellar absorption.

Identification of the exact nature of the Mg II absorption feature requires further analysis. The important point is that the results of my analysis are independent of its nature, since they do not rely on absolute flux values but rather on relative radial velocities.

5.4.4 Sources of Error

5.4.4.1 Instrumental Error

A detailed report of possible contributions to error for the optical observations was presented in Section 4.4.7, and the same principles apply to the NUV observations. However, some differences to the instrument values apply, since a different grating and hence different optics were used. The physical tilt (i.e. a tilt of the slit with regard to the nominal observing position angle) is known to have a value of $+0.27\,^\circ$ in the NUV compared with $+0.22\,^\circ$ in the optical region, and the optical distortion (i.e. the slit image on the detector is curved and tilted), which varies in angle across the detector depending on the grating used, is known to have a value in the range of $+0.9$ to $+1.2\,^\circ$ in the NUV compared to $+0.001\,^\circ$ in the optical region. As with the optical dataset, an analysis of the error contribution of each was conducted and all were found to be insignificant (i.e. $< 1\,\mathrm{km\,s^{-1}}$ which is well within the error bars of $\pm 5\,\mathrm{km\,s^{-1}}$). Nevertheless, all erroneous tilts were corrected or compensated for before data analysis was conducted.

While, in the case of the optical data, physical tilt was corrected for in the *HST* pipeline calibration and optical distortion was adequately accounted for by recentering

the emission peaks, corrections to the NUV data proved more involved. Physical tilt was corrected during the wavelength calibration which had to be carried out on the data files after the standard *HST* pipeline procedure. However, the wavelength calibration highlighted erroneous data file keywords (namely 'shifta1' and 'shifta2'), caused by a previously unidentified bug in the pipeline software and resulting in the incorrect assignment of spectral orders to emission lines. Re-running a modified version of the pipeline procedures (carried out by the Space Telescope Science Institute), with particular attention to the location on the detector of the Mg II doublet, yielded the correct keywords. The science datafile headers were then updated with the corrected keyword values. These not only assigned the correct spectral order and hence wavelength to each emission line, but also more accurately accounted for the physical tilt of the detector. Next, the calibration lamp lines were used to determine optical distortion in the region of interest on the detector. This distortion was corrected for by altering the *HST*/STIS calibration reference tables prior to wavelength calibration with standard IRAF routines. (Specifically, the 'Aperture Description' (APD) table was edited by changing the value of the 'Angle' for the relevant aperture to a value determined by measuring the tilt in the calibration lamp lines at the location of interest on the detector.) The remaining tilt to be addressed is possible inaccuracy in the position angle specified for observations. Since the same position angles were specified in both the optical and NUV observations, and I have negated this effect in the optical region (Section 4.4.7), I can assume that any such effect also has insignificant impact on the NUV spectra once recentering of the emission peak has been carried out.

5.4.4.2 Combination of Studies

The fact was noted in Section 4.4.7 that it is unusual to see the same sense of rotation with regard to the slit orientation for all jets. Bear in mind however that, of the eight targets, the seven that show rotation signatures are launched from one of five T Tauri systems. This effectively reduces the sample size. It was also noted in Section 4.4.7 that a similar optical rotation analysis of the radial velocities within the jets from T Tauri stars DG Tau (Bacciotti et al. 2002) and RW Aur (Woitas et al. 2004) with the slit placed *parallel* to the jet axis yielded results in agreement with my observing mode in which the slit is *perpendicular* to the jet axis. To strengthen the case, it is important to also highlight the fact that the observations for the jets from both DG Tau and TH 28 in the optical and NUV regions were conducted with *different detectors* (and so different optics), and yet give consistent results. This combination of studies strongly suggests that, although it is improbable that all jets (with the possible exception of LkHα321) rotate in the same

Target	Emission line	$r_{\infty,obs}$ (arcsec)	$r_{\infty,obs}$ (AU)	$\triangle v_{rad}$ (km s^{-1})	$\overline{v_{rad}}$ (km s^{-1})	v_ϕ (km s^{-1})	v_p (km s^{-1})	$r_{0,obs}$ (AU)
TH 28 receding jet	λ2796	0.116	20	7	28	4	161	0.3
	λ2796	0.203	35	6	7	3	40	2.5
TH 28 approaching jet	λ2796	0.145	25	5	26*	3	150	0.3
	λ2796	0.174	30	9	23*	5	132	0.6
DG Tau approaching jet	λ2796	0.058	8	12	198	10	251	0.2
	λ2796	0.116	16	4	192	3	244	0.1

Table 5.4: *The radius from the star in the disk plane of the jet footpoint, $r_{0,obs}$, calculated for the NUV targets using the method described in Anderson et al. (2003). Only measurements for the Mg II λ2796 emission component of the doublet were used, since vaelocity differences for the Mg II λ2803 line were mainly within error bars about zero. The mean radial velocity taken from values equidistant either side of the jet axis, $\overline{v_{rad}}$, is quoted as an absolute value (after heliocentric velocity correction). Since i_{jet} is given with respect to the plane of the sky, I calculate $v_\phi = (\triangle v_{rad}/2)/\cos i$ and $v_p = (\overline{v_{rad}})/\sin i$. The asterisks mark points where the radial velocities could not be determined due to poor Gaussian fitting, and so values were extrapolated from measured data.*

direction with regard to the slit orientation, it is not impossible and does indeed seem to be the case. Finally, note that four of the five T Tauri systems with rotation signatures are located in the same cloud (i.e. Taurus-Auriga), but no particular pattern of system alignment could be readily identified.

5.4.5 Implications for Theoretical Models

5.4.5.1 Jet Footpoint

Finally, as in Section 4.4.8, I can use these radial velocity measurements (in combination with the values in Table 4.1) to find a range for the radius from the star on the disk plane of the jet launch point, $r_{0,obs}$.

The range for the jet footpoint radius for each target is given in Table 5.4. Values were calculated for Mg II λ2796 emission only, due to the higher signal to noise, and for distances further from the jet axis to minimise beam smearing and projection effects. Depending on the observation distance from the jet axis, the footpoint extends away from the star along the disk plane. At distances of 0.″05 to 0.″15 the footpoint is located in the range 0.1 to 0.3 AU. It then extends outwards, for observations at 0.″175 to 0.″2, from 0.6 to 2.5 AU respectively.

Given the uncertainties associated with many of the physical parameters (such as stellar mass, inclination angle and distance to the T Tauri system), these calculations

represent *estimates* of the jet footpoint and so no error bars are given. Nevertheless, the observational results presented here (as with the optical results of Chapter 4) supports the idea that disk winds are launched, via the magneto-centrifugal mechanism (e.g. Königl et al. 2000), at footpoint radii within a few AU of the star. The results consistently show that, even for the higher velocity NUV observations which trace the jet close to the axis, the jet appears to be launched from a region not less than 0.1 AU from the star on the disk plane for this velocity resolution.

5.5 Conclusions

The three jet targets observed at NUV wavelengths (i.e. the bipolar jet from TH 28 and the approaching jet from DG Tau) show systematic radial velocity asymmetries in opposing positions with respect to the jet axis, within 70 AU from the source. Radial velocity differences of up to $17\,(\pm 5)\,\mathrm{km\,s^{-1}}$ were found. I interpret these as rotation signatures in the region close to the star where the jet has been collimated but has not yet manifestly interacted with the environment. The sense of rotation of the jets is then clockwise for all three targets, looking down the approaching lobe towards the star. For the bipolar jet from TH 28, the velocity differences have the same direction in both lobes, indicating opposite helicity as might be expected. A Mg II blueshifted absorption feature was present in all three targets and possibly originates in interstellar cloud material or an expanding shell around the T Tauri system. Finally, my results are consistent with the optical survey (Chapter 4), and with previously published results for DG Tau (Bacciotti et al. 2002) which were shown to be in agreement with magneto-centrifugal 'Disk wind' predictions. My analysis leads to values for the distance of the jet footpoint from the star of ~ 0.1 to 2.5 AU, consistent with models of magneto-centrifugal jet launching (Anderson et al. 2003).

It was hoped that the higher spatial and spectral resolution of the *HST*/STIS in the NUV would afford a more quantitative analysis (i.e. error bars being typically one fifth of the spectral sampling). However, I did not expect to find the tricky combination of a broad profile shape in the dispersion direction, a relatively narrow spatial FWHM, and significant interruption by absorption. This forced me to adopt a conservative approach to errors, i.e $\pm 5\,\mathrm{km\,s^{-1}}$. Also, although the higher spatial resolution allows me to probe closer to the jet axis, beam smearing and projection effects appear to prevent me from obtaining the greater detail in radial velocity profiles that was hoped for. Nevertheless, the NUV measurements fit well with the results obtained from the optical data.

6

Overall Conclusions

This chapter draws together the overall conclusions of this thesis, and describes the direction of further research and collaborations.

6.1 Conclusions

In Chapters 3, 4 and 5, I have described research which examines both the generation and propagation of jets/outflows from T Tauri stars, with a view to improving understanding of the star formation process through the provision of observational contraints for numerical simulations and theoretical modelling.

Chapter 3 describes multi-epoch *HST*/WFPC observations of the XZ Tauri system which allowed a time evolution study of both the binary and its associated outflow. The considerable changes observed in both, over only 6 years, allowed a photometric study of stellar variability and a proper motion study of the limb-brightened shock front. Stellar photometry revealed that the northern component of the binary has flared in EXor-type fashion increasing in brightness by 3 magnitudes in the R-band over only 3 years. Such a dramatic change, when considered in the light of spectroscopic evidence available in the literature, suggest that this component is in fact the source of the outflow. Meanwhile,

proper motion studies of the bowshock revealed a marked deceleration, from $\sim 145\,\mathrm{km\,s^{-1}}$ to $\sim 115\,\mathrm{km\,s^{-1}}$, as it propagated from $\sim 600\,\mathrm{AU}$ to $\sim 800\,\mathrm{AU}$ from the source. Numerical simulations then highlighted the necessity of invoking a wide angle wind (of opening angle $\sim 20°$), to reproduce the low aspect ratio of the bubble, and a 6 fold increase in ambient density, to reproduce the shock deceleration.

Chapter 4 investigates several optically visible jets close to their stellar source, in order to determine whether or not jet rotation is present in the early stages of propagation. I have established, through a survey of 8 jets at optical wavelengths, that there consistently exist radial velocity differences of up to $\sim 30 \pm 5\,\mathrm{km\,s^{-1}}$ between one side of the jet and the other, before the jet has travelled beyond 100 AU from the source. I interpret these radial velocity asymmetries as rotation signatures in the region close to the star where the jet has been collimated but has not yet manifestly interacted with the environment. In the two cases where both lobes of the bipolar jet were examined, radial velocity differences were consistent in direction, i.e. opposite helicity in opposing jets. Using the standard 'Disk wind' model for centrifugally launched MHD jets, my results lead to values for the distance of the jet footpoint from the central axis of typically ~ 0.1 to 0.8 AU for the higher velocity gas in the jet and ~ 0.6 to 1.2 AU for the lower velocity material, i.e. values which are consistent with models of magneto-centrifugal launching (Anderson et al. 2003). Finally, my estimates of jet mass and angular momentum fluxes, based on these velocity differences, indicate that the jet could in fact extract most, if not all, of the angular momentum from the system. This demonstrates *observationally* that it is very reasonable to assume jets can indeed play a significant role in angular momentum transport, allowing the T Tauri star to rotate below break-up velocity and further accrete the material of its circumstellar disk.

Chapter 5 investigates YSO jets close to their stellar source at NUV wavelengths, in order to establish if the results of Chapter 4 are borne out at shorter wavelengths. A survey of 3 jets at near ultraviolet wavelengths revealed radial velocity differences of up to $17 \pm 5\,\mathrm{km\,s^{-1}}$. Again, I interpret these radial velocity asymmetries as rotation signatures within the jet. Two of these NUV targets form the bipolar jet of one system, and show the same sense of rotation with regard to each other and with regard to the optical results. These NUV results lead to values for the distance of the jet footpoint from the star of ~ 0.1 to 2.5 AU, in line with footpoints values for the optical dataset. The footpoint values are smaller for the NUV emission showing that these lines, which trace the higher velocity component of the jet close to its axis, are launched at a distance on the disk

plane closer to the star than the lower velocity optical lines. Lastly, a Mg II blueshifted absorption feature was present in all three targets, and was concluded to originate from interstellar cloud material.

In summary, I have used *HST* observations of optically visible outflows from T Tauri stars to attempt to address some long-standing questions regarding the star formation process. The high spatial resolution of *HST* images allowed me to carry out a temporal study of the XZ Tauri system over a very short time base compared to the capabilities of ground-based observing alone. Analysis of the observations taken over a 6 year period showed that the system changed dramatically. This short timescale proper motion study provided not simply velocity but also deceleration measurements and so, when tied to direct guidance of numerical simulations, represents the first of its kind to date in studies of T Tauri outflow propagation. Spectroscopically, the spatial resolution of *HST* allowed a radial velocity analysis across YSO jets extremely close to their source, at both optical and NUV wavelengths. Observations provided survey indications of T Tauri jet rotation, a valuable constraint in modeling jet launching. This constraint revealed its potential to differentiate between models of magnetocentrifugal jet launching mechanisms, and provided observational backing for the proposed theory of jets as extractors of angular momentum from protostellar systems.

6.2 Future Work

6.2.1 Circumstellar Disk Rotation

Unfortunately, due to the failure, in August 2004, of the power supply for *HST*/STIS, which was used in conducting the high resolution optical and NUV jet observations, the survey plans for the initial jet channel came to an abrupt end. However, ground-based adaptive optics facilities and interferometry provide alternative avenues for future work in the optical and near infrared regimes. With such facilities, this survey may be extended to include other jet targets, thus increasing the sample size and so ascertaining the commonality of T Tauri jet rotation.

Simultaneously, to continue this research in the same vein, it is interesting to study the disks which feed these jets in order to understand the dynamic relationship between the two. The ultimate confirmation of jet rotation would be provided by evidence of radial velocity differences across the millimetre wavelength emitting *disks* of our survey sources and, most importantly, evidence of whether there is *agreement in the direction* of radial

velocity differences within the jet/disk system, implying that both bipolar jet and disk rotate with the same sense. These objects are best examined through their cooler emission at longer wavelengths which can escape the dusty environment of the circumstellar disk. Observationally, the difficulty here lies in the fact T Tauri disks are weak CO emitters. Current facilities available to suit these purposes are the radio interferometer on Plateau de Bure near Grenoble, or the OVRO in California.

In 2002, results were published of high angular resolution millimetre wavelength OVRO observations of the circumstellar disk surrounding the young star DG Tauri (Testi et al. 2002). The velocity pattern in the inner regions of the disk was found to be consistent with Keplerian rotation about a central star. The disk rotation was also consistent with the toroidal velocity pattern in the initial channel of the optical jet discussed in Chapter 4, as inferred from *HST*/STIS spectra of the first 100 AU from the source. These observations support the tight relationship between disk and jet kinematics postulated by the popular magnetocentrifugal models for jet formation and collimation. Although the jet from the T Tauri star DG Tauri has been extensively studied at high resolution in recent years and displays properties that are in general agreement with magnetocentrifugal models for jet launching, results for one object are not enough to support general conclusions about disk rotation. In fact, Plateau de Burre observations of the disk around RW Aur (Cabrit et al. in preparation) revealed a disk perpendicular to the jet but showed rotation opposite in sense to that derived for the jet. However, the RW Aur system is quite complex due to the companion stars and so interpretation of the results is not straightforward. Observations of the disk rotation of HH30 have also proved inconclusive, and remain unpublished. It is therefore mandatory to extend the sample, the main goal being to establish whether disks do indeed rotate in the same direction as their accompanying bipolar jets, and to evaluate the balance of angular momentum between infall and outflow.

The first step in this project has already been taken, in that our recent proposal for observing time on the Plateau de Burre interferometer (P.I.: C Dougados, Grenoble) has been accepted. Observations of the CW Tau disk are planned for August 2005. The aim is to map molecular gas emission from the circumstellar disk, in order to check whether the sense of disk rotation is consistent with that of the jet. This study is part of a large-scale coordinated effort conducted in the context of the JETSET Marie Curie European Research and Training Network. Following this, the remaining targets in our jet rotation survey for which disk rotation has yet to be examined are TH 28 and LkHα 321.

6.2.2 Kinematics on Jet Launching Scales

The difficulties in obtaining observations of jet and disk rotation arise from the fact that these studies are bordering the limits of current observational capabilities. A detailed velocity analysis not only requires high spectral resolution but must also be accompanied by subarcsecond spatial resolution, even for the nearest star forming regions. With *HST* (of spatial resolution $\sim 0\farcs1$, i.e. ~ 14 AU in Taurus), I have been able to access the external border of the jets in the Taurus-Auriga cloud. Here there are indications for rotation around the symmetry axis for the resolved low/moderate velocity component of the jet. However, to truly test currently proposed models, there is a need to observe the interplay between accretion and ejection on the launching scale a few AU from the star.

The primary goal here is to observe with facilities that have the capability to reveal jet/disk dynamics in the *innermost* jet/disk region, in the hope of revealing the mechanisms at work in the central jet engine. Fortunately, this may be possible with the coming generation of interferometers. Currently, only observations with the new infrared spectrograph of the Astronomical Multiple BEam Recombiner (AMBER) on the Very Large Telescope Interferometer (VLTI) in Chile would meet this requirement, with spatial resolution of 1 milliarcsecond (~ 0.1 AU for Taurus).

Consequently, the natural extension of this research is to examine the kinematics of the jet/disk system with the greater resolution of with AMBER on the VLTI. The high resolution of AMBER will allow a search for interesting kinematic features, including signatures of rotation about the jet axis. This new ground-based observing facility will also allow exploration of the jet launch zone of less evolved more embedded protostars, as opposed to the optically visible sources I have examined in my jet survey. In such less evolved sources the jets are more powerful, due to higher levels of accretion activity, and so more pronounced kinematic features should be detectable. Therefore, high resolution observations of the inner jet/disk region in the infrared wavelength range should provide a breakdown, in unprecedented detail, of the complex infall and outflow kinematics present in protostellar accretion/ejection structures.

Furthermore, I will be collaborating with researchers at Arcetri Observatory in Italy. Considering that understanding star formation is one of the primary science goals of the AMBER project, Arcetri Observatory is part of an international consortium which has guaranteed observing time, thereby ensuring that this research is a fully achievable project.

6.2.3 Jet Diagnostics

Finally, although it is widely accepted that the emission spectrum of HH knots within the jet is produced from a gas excited by mild shocks, the detailed physical conditions of the plasma are still under debate. Furthermore, the importance of understanding jet diagnostics close to the source was highlighted in Chapter 4 (Section 4.4.8) in that it is necessary for calculation of accurate jet angular momentum fluxes.

Observationally, the electron density is easily found from the [S II] doublet (providing the density is below the critical density), but other crucial physical parameters such as the hydrogen ionisation fraction, the total electron density and the average electron temperature are poorly known. With a few basic assumptions, a spectroscopic diagnostic technique has been developed (Bacciotti & Eislöffel 1999) which allows the determination, from optical emission line ratios, of these parameters. Unlike other techniques, the results do not depend on any specific mechanism for jet formation and/or evolution. Briefly, the technique relies primarily on the assumptions that: standard solar abundances are adopted; all the sulfur is considered to be singly ionised, provided the jet is of low ionisation; and finally, ionisation of oxygen and nitrogen results primarily from charge exchange with hydrogen, based on low electron temperature and no photoionisation since the source is usually a low mass star with little production of ionising radiation. Under these three assumptions, the technique then relies on the relationship between three line ratios: the electron density is easily found from the [S II] doublet; the ratio of the oxygen to nitrogen lines is more sensitive to the ionisation fraction; and the sulfur to oxygen ratio is more sensitive to electron temperature. Since the ionisation state of oxygen and nitrogen can be expressed as a function of hydrogen ionisation fraction and electron temperature, the intensity ratio of any two observed emission lines is a *known* function of electron density, hydrogen ionisation fraction and electron temperature. So comparing the observed line ratios makes it possible to retrieve the values of these parameters and hence calculate the hydrogen density in the emitting gas, a crucial parameter in any jet model yet poorly known as it cannot be measured directly.

Using this code, the various line fluxes from my optical data will allow me to carry out a detailed excitation analysis of the initial jet channel of several sources.

Bibliography

Ambartsumian, V. A., 1957, IAUS, **3**, 177

Anderson, J. M., Li, Z.-Y., Krasnopolsky, R., & Blandford, R., 2003, ApJ, **590**, L107

Appenzeller, I., Oestreicher, R., & Jankovics, I., 1984, A&A, **141**, 108

Arce, H. G., & Sargent, A. I., 2005, ApJ, **624**, 232

Ardila, D. R., Basri, G., Walter, F., Valenti, J., & Johns-Krull, C., 2002, ApJ, **566**, 1100

Ardila, D. R., Basri, G., Walter, F. M., Valenti, J. A., & Johns-Krull, C. M., 2002, ApJ, **567**, 1013

Arnaud, M., & Rothenflug, R., 1985, A&A Suppl. Ser., **60**, 425

Arnaud, M., & Raymond, J., 1992, ApJ, **398**, 394

Bacciotti, F., Chiuderi, C., & Oliva, E., 1995, A&A, **296**, 185

Bacciotti, F., & Eislöffel, J., 1999, A&A, **342**, 717

Bacciotti, F., Hirth, G. A., & Natta, A., 1996, A&A, **310**, 309

Bacciotti, F., Mundt, R., Ray, T. P., Eislöffel, J., Solf, J., & Camezind, M., 2000, ApJ, **537**, L49

Bacciotti, F., Ray, T. P., Mundt, R., Eislöffel, J., & Solf, J., 2002, ApJ, **576**, 222

Bachiller, R., 1996, ARA&A, **34**, 111

Bally, J., Devine, D., & Reipurth, B., 1996, ApJ, **473**, L49

Balbus, S. A., 2001, ApJ, **562**, 909

Balbus, S. A., 2003, A&A, **41**, 555

Balbus, S. A., & Hawley, J. F., 2003, ApJ, **376**, 214

Basri, G. S., & Linsky, J. L., 1979, ApJ, **234**, 1023

Bastien, P., & Menard, F., 1988, ApJ, **326**, 334

Bedogni, R., & Woodward, P. R., 1990, A&A, **231**, 481

Beckwith, S. V. W., & Sargent, A. I., 1996, Nature, **383**, 139

Beckwith, S. V. W., Sargent, A. I., Chini, R. S., & Guesten, R., 1990, AJ, **99**, 924

Beckwith, S., Skrutskie, M. F., Zuckerman, B., & Dyck, H. M., 1984, ApJ, **287**, 793

Benson, P. J., Caselli, P., & Myers, P. C., 1998, ApJ, **506**, 743

Bally, J., & Devine, D., 1994, ApJ, **428**, L65

Blandford, R. D., & Payne, D. G., 1982, MNRAS, **199**, 883

Blitz, L., 1993, in Protostars and Planets III, ed. E. H. Levy & J. I. Lunine (Tuscon: Univ. Arizona Press), 125

Blondin, J. M., Königl, A., & Fryxell, B. A., 1989, ApJ, **337**, L37

Blondin, J. M., Fryxell, B. A., & Königl, A., 1990, ApJ, **360**, 370

Blondin, J. M., & Knerr, J. M., 1992, AAS, **181**, 6706

Bodenheimer, P., 1978, ApJ, **224**, 488

Bodenheimer, P., 1995, ARA&A, **33**, 199

Böhm-Vitense, E., Mena-Werth, J., Carpenter, K. G., & Robinson, R. D., 2001, ApJ, **550**, 457

Bonnell, I. A., Bate, M. R., & Zinnecker, H., 1998, MNRAS, **298**, 93

Boss, A. P., 1998, AREPS, **26**, 53

Burrows, C. J., Stapelfeldt, K. R., Watson, A. M., Krist, J. E., Ballester, G. E., Clarke, J. T., Crisp, D., Gallagher III, J. S., Griffiths, R. E., Hester, J. J., Hoessel, J. G., Holtzman, J. A., Mould, J. R., Scowen, P. A., Trauger, J. T., & Westphal, J. A., 1996, ApJ, **473**, 437

Butler, R. P., & Marcy, G. W., 1996, ApJ, **464**, L153

Cabrit, S., 2002, EAS, **3**, 147

Cabrit, S., & André, P., 1991, ApJ, **379**, L25

Cabrit, S., Edwards, S., Strom, S. E., & Strom, K. M., 1990, ApJ, **354**, 687

Cabrit, S., Lagage, P.-O., McCaughrean, M., & Olofsson, G., 1997, A&A, **321**, 523

Calvet, N., & Gullbring, E., 1998, ApJ, **509**, 802

Calvet, N., 1997, IAUS, **182**, 417

Calvet, N., Basri, G., Imhoff, C. L., & Giampapa, M. S., 1985, ApJ, **293**, 575

Calvet, N., Hartmann, L., & Strom, S. E., 2000, in Protostars and Planets IV, ed. V. Mannings, A. P. Boss & S. S. Russell (Tuscon: Univ. Arizona Press), 377

Cerqueira, A. H., & de Gouveia Dal Pino, E. M., 2004, A&A, **426**, L25

Cerqueira, A. H., de Gouveia dal Pino, E. M., & Herant, M., 1997, ApJ, **489**, L185

Casse, F., & Ferreira, J., 2000, A&A, **361**, 1178

Chandrasekhar S., 1961, Hydrodynamic and Hydromagnetic Stability. Oxford Univ. Press, Oxford, p. 225

Chavarría-K., C., & de Lara, E., RMxAA, 1981, **6**, 159

Cochran W. D., Hatzes, A. P., Butler, R. P., & Marcy, G. W., 1996, DPS, **28**, 1204

Coffey, D., Bacciotti, F., Woitas, J., Ray, T. P., & Eislöffel, J., 2004, ApJ, **604**, 758

Coffey, D., Downes, T. P., & Ray, T. P., 2004, A&A, **419**, 593

Cohen, M., Harvey, P. M., & Schwartz, R. D., 1985, ApJ, **296**, 633

Corcoran, M., & Ray, T. P., 1997, A&A, **321**, 189

Crawford, J. A., & Kraft, R. P., 1956, ApJ, **123**, 44

Crutcher, R. M., Troland, T. H., Goodman, A. A., Heiles, C., Kazes, I., & Myers, P. C., 1993, ApJ, **407**, 175

Davis, C. J., Berndsen, A., Smith, M. D., Chrysostomou, A., & Hobson, J., 2000, MNRAS, **314**, 241

DeCampli, W. M., 1981, ApJ, **244**, 124

De Young, D. S., 1986, ApJ, **307**, 62

Dgani, R., van Buren, D., & Noriega-Crespo, A., 1996, ApJ, **461**, 927

Dougados, C., Cabrit, S., Ferreira, J., Pesenti, N., Garcia, P., & O'Brien, D., 2004, AP&SS, **292**, 643

Dougados, C., Cabrit, S., Lavalley, C., & Ménard, F., 2000, A&A, **357**, L61

Dougados, C., Cabrit, S., & Lavalley-Fouquet, C., 2002, RMxAC, **13**, 43

Downes, T. P., & Ray, T. P., 1998, A&A, **331**, 1130

Downes, T. P., & Ray, T. P., 1999, AAp, **345**, 977

Dring, A. R., Linsky, J., Murthy, J., Henry, R. C., Moos, W., Vidal-Madjar, A., Audouze, J., & Landsman, W., 1997, ApJ, **488**, 760

Edwards, S., Cabrit, S., Strom, S. E., Heyer, I., Strom, K. M., & Anderson, E., 1987, ApJ, **321**, 473

Elias, J. H., 1978, ApJ, **224**, 857

Edwards, S., Ray, T. P., & Mundt, R., 1993, in Protostars and Planets III, ed. E. H. Levy & J. I. Lunine (Tuscon: Univ. Arizona Press), 567

Ferreira, J., 1997, A&A, **319**, 340

Fuller, G. A., Ladd, E. F., & Hodapp, K. W., 1996, ApJ, **463**, L97

Ghosh, P., & Lamb, F. K., 1977, ApJ, **217**, 578

Ghosh, P., & Lamb, F. K., 1978, ApJ, **223**, L83

Gomez de Castro, A. I., 1993, ApJ, **412**, 43

Goodman A. A., Barranco, J. A., Wilner, D. J., & Heyer, M. H., 1998, ApJ, **504**, 223

Gullbring, E., Calvet, N., Muzerolle, J., & Hartmann, L., 2000, ApJ, **544**, 927

Graham, J. A., & Elias, J. H., 1983, ApJ, **272**, 615

Graham, J. A., & Heyer, M. H., 1988, PASP, **100**, 1529

Haas, G. M., Leinert, C., & Zinnecker, H., 1990, AAp, **230**, L1

Haro, G., 1952, ApJ, **115**, 572

Haro, G., 1953, ApJ, **117**, 73

Hartigan, P., Bally, J., Reipurth, B., & Morse, J. A., 2000, in Protostars and Planets IV, ed. V. Mannings, A. P. Boss & S. S. Russell (Tuscon: Univ. Arizona Press), 841

Hartigan, P., Edwards, S., & Ghandour, L., 1995, ApJ, **452**, 736

Hartigan, P., Edwards, S., & Pierson, R., 2004, ApJ, **609**, 261

Hartigan, P., & Kenyon, S. J., 2003, ApJ, **583**, 334

Hartigan, P., Morse, J. A., Tumlinson, J., Raymond, J., & Heathcote, S., 1999, ApJ, **512**, 901

Hartmann, L., Hewett, R., Stahler, S., & Mathieu, R. D., 1986, ApJ, **309**, 275

Hartmann, L., & Kenyon, S. J., 1996, ARA&A, **34**, 207

Hawley, J. F., Balbus, S. A., & Winters, W. F., 1999, ApJ, **518**, 394

Herbst, W., Herbst, D. K., Grossman, E. J., & Weinstein, D., 1994, ApJ, **108**, 1906

Herbig, G. H., 1950, ApJ, **111**, 11

Herbig, G. H., 1951, ApJ, **113**, 697

Herbig, G. H., 1989, Proc. of the ESO Workshop on Low Mass Star Formation and Pre-main Sequence Objects, Garching, Germany, ed. Bo Reipurth, 233

Jennison, R. C., & Das Gupta, M. K., 1953, Nature, **172**, 996

Joy, A. H, 1945, ApJ, **102**, 168

Königl, A., 1986, Can. J. Phys., **64**, 362

Königl, A., & Pudritz, R., 2000, in Protostars and Planets IV, ed. V. Mannings, A. P. Boss & S. S. Russell (Tuscon: Univ. Arizona Press), 759

Krautter, J., 1986, A&A, **161**, 195

Krist, J. E., Burrows, C. J., Stapelfeldt, K. R., Ballester, G. E., Clarke, J. T., Crisp, D., Evans, R. W., Gallagher III, J. S., Griffiths, R. E., Hester, J. J., Holtzman, J. A., Hoessel, J. G., Mould, J. R., Scowen, P. A., Trauger, J. T., Watson, A. M., & Westphal, J. A., 1997, ApJ, **481**, 447 (K97)

Krist, J. E., Stapelfeldt, K. E., Burrows, C. J., Hester, J. J., Watson, A. M., Ballester, G. E., Clarke, J. T., Crisp, D., Evans, W. R., Gallagher III, J. S., Griffiths, R. E., Hoessel, J. G., Holtzman, J. A., Mould, J. R, Scowen, P. A., & Trauger, J. T., 1999, ApJ, **515**, L35 (K99)

Kwan, J., & Tademaru, E., 1988, AJ, **332**, L41

Lada, C. J., 1999, in The Origin of Stars and Planetary Systems, ed. C. J. Lada & N. D. Kylafis (Dordrecht: Kluwer), 143L

de Laplace, P. S., 1796, Exposition du Système du monde, Paris

Larson, R. B., 1969, MNRAS, **145**, 297

Lighthill, J., 1978, Waves in Fluids (Cambridge Univ. Press)

Lin, D. N. C., & Papaloizou, J. C. B., 1996, ARA&A, **34**, 703

López, J. A., Vázquez, R., & Rodríguez, L. F., 1995, ApJ, **455**, L63

López-Martín, L., Cabrit, S., & Dougados, C., 2003, A&A, **405**, L1

Lovelace, R. V. E., Romanova, M. M., & Bisnovatyi-Kogan, G. S., 1995, MNRAS, **275**, 244

Mayor, M., & Queloz, D., 1995, Nature, **378**, 355

McCaughrean, M. J., & O'Dell, C. R., 1996, AJ, **111**, 1977

McCray, R., & Kafatos, M., 1987, ApJ, **317**, 190

McGroarty, F., & Ray, T. P., 2004, A&A, **420**, 975

McKee, C. F., & Cowie, L. L., 1975, ApJ, **195**, 715

Mestel, L., & Spitzer, L., 1956, MNRAS, **116**, 503

Motte, F., Andre, P., & Neri, R., 1998, A&A, **336**, 150

Mundt, R., Buehrke, T., Fried, J. W., Neckel, T., Sarcander, M., & Stocke, J., 1984, A&A, **140**, 17

Mundt, R., Buehrke, T., Solf, J., Ray, T. P., & Raga, A. C., 1990, A&A, **232**, 37

Mundt, R., Brugel, E. W., & Buehrke, T., 1987, ApJ, **319**, 275

Mundt, R., & Eislöffel, J., 1998, AJ, **116**, 860

Mundt, R., & Fried, J. W., 1983, ApJ, **274**, L83

Mundt, R., Ray, T.P., & Buhrke, T. 1988, ApJ, **333**, L39

Mundt, R., Buehrke, T., Solf, J., Ray, T. P., & Raga, A. C., 1990, A&A, **232**, 37

Mundy L. G., Looney, L. W., Erickson, W., Grossman, A., Welch, W. J., Forster, J. R., Wright, M. C. H., Plambeck, R. L., Lugten, J., & Thornton, D. D., 1996, ApJ, **464**, L169

Mundy, L. G., Looney, L. W., & Welch, W. J., 2000, in Protostars and Planets IV, ed. V. Mannings, A. P. Boss & S. S. Russell (Tuscon: Univ. Arizona Press), 355

Muzerolle, J., Calvet, N., & Hartmann, L., 2001, ApJ, **550**, 944

Muzerolle, J., Calvet, N., & Hartmann, L., 1998a, ApJ, **492**, 743

Muzerolle, J., Hartmann, L., & Calvet, N., 1998b, AJ, **116**, 455

Myers, P. C., 1995, in Molecular Clouds and Star Formation, ed. C. Yuan & J. H. You (Singapore: World Scientific), 47

Norman, M. L., Smarr, L., Winkler, K. H., & Smith, M. D., 1982, A&A., **113**, 285

O'Dell, C. R., Wen, Z., & Hu, X., 1993, ApJ, **410**, 696

O'Dell, C. R., & Wen, Z., 1994, ApJ, **436**, 194

O'Sullivan, S., & Ray, T. P., 2000, A&A, **363**, 355

Osterbrock, D. E., 1989, SvA, **33**, 694

Ostriker, E. C., & Shu, F., 1995, ApJ, **447**, 813

Padoan, P., Jimenez, R., Juvela, M., & Nordlund, A., 2004, ApJ, **604**, L49

Palla, F., & Stahler, S. W., 1991, ApJ, **375**, 288

Papaloizou, J. C. B., & Lin, D. N. C., 1995, ARA&A, **33**, 505

Parker, E. N., 1958, ApJ, **128**, 664

Parker, E. N., 1965, SSRv, **4**, 666

Parsamian, E. S., Mujica, R., & Corral, L., 2002, Astrophysics, **45**, 393

Pesenti, N., Dougados, S., Cabrit, S., Ferreira, J., Casse, F., Garcia, P., & O'Brien, D., 2004, A&A, **416**, L9

Pety, J., Gueth, F., Guilloteau, S., & Dutrey, A., in Semaine de l'Astrophysique Francaise, ed. F. Combes & D. Barret (Editions de Physique), 2002, 481

Petrov, P. P., Gahm, G. F., Gameiro, J. F., Duemmler, R., Ilyin, I. V., Laakkonen, T., Lago, M. T. V. T., & Tuominen, I., 2001, A&A, **369**, 993

Piirola, V., Scaltriti, F., & Coyne, G. V., 1992, Nature, **359**, 399

Pratap, P., Dickens, J. E., Snell, R. L., Miralles, M. P., Bergin, E. A., Irvine, W. M., & Schloerb, F. P., 1997, ApJ, **486**, 862

Pudritz, R. E., & Norman, C. A., 1983, ApJ, **274**, 677

Raga, A. C., 1988, ApJ, **335**, 820

Raga, A. C., Binette, L., Canto, J., & Calvet, N., 1990, ApJ, **364**, 601

Raga, A. C., Taylor, S. D., Cabrit, S., & Biro, S., 1995, A&A, **296**, 833

Ray, T. P., 1987, A&A, **171**, 145

Ray, T. P., 2000, in Laser Guide Star Adaptive Optics for Astronomy, ed. N. Ageorges & C. Dainty (Dordrecht: Kluwer), 263

Ray, T. P., Mundt, R., Dyson, J. E., Falle, S. A. E. G., & Raga, A. C., 1996, ApJ, **468**, L103

Ray, T., Muxlow, T., Axon, D., Brown, A., Corcoran, D., Dyson, J., & Mundt, R., 1997, Nature, **385**, 415

Reipurth B., & Bally, J., 2001, ARA&A, **39**, 403

Reipurth, B., Bally, J., Graham, J. A., Lane, A. P., & Zealey, W. J., 1986, A&A, **164**, 51

Reipurth B., & Heathcote, S., 1991, A&A, **246**, 511

Reipurth B., Heathcote, S., Morse, J., Hartigan, P., & Bally, J., 2002, ApJ, **123**, 362

Richer J. S., Shepherd, D. S., Cabrit, S., Bachiller, R., & Churchwell, E., 2000, Protostars and Planets IV, V. Mannings, A. P. Boss & S. S. Russell (Tuscon: Univ. Arizona Press), 867

Salmerson, R., & Königl, A., 2005, in Protostars and Planets V, http://www.lpi.usra.edu/meetings/ppv2005/pdf/8382.pdf

Sargent, A. I., & Beckwith, S., 1987, ApJ, **323**, 294

Sgro, A. G., 1975, ApJ, **197**, 621

Shakura, N. I., & Sunyaev, R. A., 1973, A&A, **24**, 337

Shu, F. H., Adams, F. C., & Lizano, S., 1987, ARA&A, **25**, 23

Shu, F. H., Najita, J. R., Shang, H., & Li, Z.-Y., 2000, in Protostars and Planets IV, ed. V. Mannings, A. P. Boss & S. S. Russell (Tuscon: Univ. Arizona Press), 789

Shu, F., Najita, J., Galli, D., Ostriker, E., & Lizano, S., 1993, in Protostars and Planets III, ed. E. H. Levy & J. I. Lunine (Tuscon: Univ. Arizona Press), 3

Shu, F., Najita, J., Ostriker, E., Wilken, F., Ruden, S., & Lizano, S., 1994, ApJ, **429**, 781

Stone, J. M., & Norman, M. L., 1993, ApJ, **413**, 198

Suttner, G., Smith, M. D., Yorke, H. W., & Zinnecker, H., 1997, A&A, **318**, 595

Schwartz, 1975, BAAS, **7**, 548

Takami, M., Chrysostomou, A., Ray, T. P., Davis, C., Dent, W. R. F., Bailey, J., Tamura, M., & Terada, H., 2004, A&A, **416**, 213

Terlevich, E., 1987, MNRAS, **224**, 193

Testi, L., Bacciotti, F., Sargent, A. I., Ray, T. P., & Eislöffel, J., 2002, A&A, **394**, 31

Uchida, Y., & Shibata, K., 1985, PASJ, **37**, 515

Vishniac, E. T., 1994, ApJ, **428**, 186

Vlahakis, N., Tsinganos, K., Sauty, C. & Trussoni, E., 2000, MNRAS, **318**, 417

Ward-Thompson, D., Motte, F., & Andre, P., 1999, MNRAS, **305**, 143

Wardle, M., & Königl, A., 1993, ApJ, **410**, 218

Weber, E. L., & Davis, L., 1967, ApJ, **148**, 217

Whelan, E. T., Ray, T. P., & Davis, C. J., 2004, A&A, **417**, 247

White, R. J., & Ghez, A. M., 2001, ApJ, **556**, 265 (WG01)

Wilson, T. L., & Walmsley, C. M., 1989, A&ARv, **1**, 141

Woitas, J., Bacciotti, F., Ray, T. P., Marconi, A., Coffey, D., & Eislöffel, J., 2005, A&A, **432**, 149

Woitas, J., Köhler, R., & Leinert, C., 2001, AAp, **369**, 249

Woitas, J., Leinert, Ch., & Köhler, R., 2001, A&A, **376**, 982

Woitas, J., Ray, T. P., Bacciotti, F., Davis, C. J., & Eislöffel, J., 2002, ApJ, **580**, 336